Computational insights into the strain aging phenomenon in bcc iron at the atomic scale

Roberto Gomes De Aguiar Veiga

Thèse

Computational insights into the strain aging phenomenon in bcc iron at the atomic scale

présentée devant

L'Institut National des Sciences Appliquées de Lyon
pour obtenir
le grade de docteur

Ecole doctorale : Matériaux de Lyon
Spécialité: Matériaux

par
Roberto GOMES DE AGUIAR VEIGA

Soutenue le 16 septembre 2011 devant la Commission d'examen

Jury

Professeur David BACON	University of Liverpool
Professeur Chad SINCLAIR	University of British Columbia
Professeur Philippe MAUGIS	Université Paul Cézanne Marseille-Aix III
Professeur Michel PEREZ	Institut National des Sciences Apliquées de Lyon
Professeur Charlotte BECQUART	Ecole Nationale Supérieure de Chimie de Lille
Docteur Ghiath MONNET	EDF R&D

To Dani, Edu, and Maria da Penha.

Contents

List of Tables

List of Figures

List of Algorithms

List of Abbreviations

3DAP	Three-dimensional atom probe tomography
AKMC	Atomistic kinetic Monte Carlo
ART	Activation-relaxation technique
CI-NEB	Climbing image nudge elastic band
BCC	Body centered cubic
CG	Conjugate gradient
DSA	Dynamic strain aging
EAM	Embedded atom method
ECOPoSAP	Energy-compensated optical position sensitive atom probe
FIM	Field ion microscopy
KMC	Kinetic Monte Carlo
LAMMPS	Large-scale Atomic/Molecular Massively Parallel Simulator
MC	Monte Carlo
MD	Molecular dynamics
NEB	Nudged elastic band
PAD	Periodic array of dislocations
PLC	Portevin-LeChatelier
SSA	Static straing aging
TaR	Translation-and-relaxation
TEM	Transmission electron microscopy
TEP	Thermo-electric power
ULC	Ultra low carbon

Acknowledgements

Many people helped me along this journey.

First, I would like to thank my supervisors, Profs. Michel Perez (Institut National des Sciences Apliquées de Lyon, INSA-Lyon) and Charlotte Becquart (École Nationale Supérieure de Chimie de Lille, ENSCL) for their support and guidance.

I extend the same words to Drs. Christophe Domain and Ghiath Monnet (EDF R&D), Dr. Nicolas Castin (Belgian Nuclear Research Centre, SCK-CEN), and Prof. Chad Sinclair (University of British Columbia, UBC) for useful discussions about metallurgy and simulations.

Additionally, I would also to acknowldege my colleagues – professors, students, and administrative staff – at the laboratories MATEIS (INSA-Lyon) and UMET (Université des Sciences et Technologies de Lille).

During this time in France, I made many good friends, from all over the world. Whether good or bad times, it is always much better when we are not alone. To all my friends I have to say: thank you very much, we had a great time together!

It is worth mentioning that this PhD project had as industrial partner EDF, which provided funding through a contract with the Institut National des Sciences Apliquées de Lyon. This financial suport is gratefully acknowledged.

Last but not least (in Portuguese): Aproveito também para agradecer minha família no Brasil pela paciência e por suportar da melhor maneira possível a distância. Espero que todas as lágrimas que derramamos ao longo desses anos por causa da saudade não tenham sido em vão.

General introduction

The static strain aging (SSA) concept refers to the hardening of a material that has undergone plastic deformation and then is aged for a certain period of time. As represented in Fig. 1, the most evident manifestation of SSA is the increase in the yield stress. In the late 1940s, Cottrell and Bilby proposed a theory to explain SSA in ferritic steels [Cottrell 1949]. In a few words, this theory states that, during the rest time, the dislocations introduced by plastic deformation interact with the interstitial carbon atoms in solid solution in the iron matrix through their respective stress fields; carbon segregation to dislocations is the consequence of this interaction. As more carbon atoms segregate, an "atmosphere" grows around the dislocations. This carbon Cottrell atmosphere hinders the dislocation motion upon reloading, such that a higher stress is required in order to make the dislocation tear away from the solutes. It is commonly accepted that the Cottrell atmosphere formation is the first stage of static strain aging. The second stage is the precipitation of carbides in the dislocation vicinity. However, if carbon concentration is low, only the first stage is expected to occur.

Apart from the increase in the yield stress after straining and other mechanical properties related to the dislocation anchoring (e.g., the fatigue strength, the ductile-to-brittle transition, the ultimate tensile strength, and so forth), other aging effects also arise from the removal of solutes from the iron matrix. For example, the thermoelectric power (TEP) measurement is known to be very sensitive to the specimen microstructure in general and the carbon content in solution in particular. As such, it provides a convenient way of quantifying the amount of carbon content still in solution after a prescribed aging time. Fig. 2 presents the TEP variation of a ULC steel at different aging times and temperatures [Lavaire 2001].

Recent advances in the experimental techniques, particularly the field ion microscopy and the atom probe tomography [Kelly 2007], made possible to image Cottrell atmospheres, which are no longer mere conjectures. L. Chang,

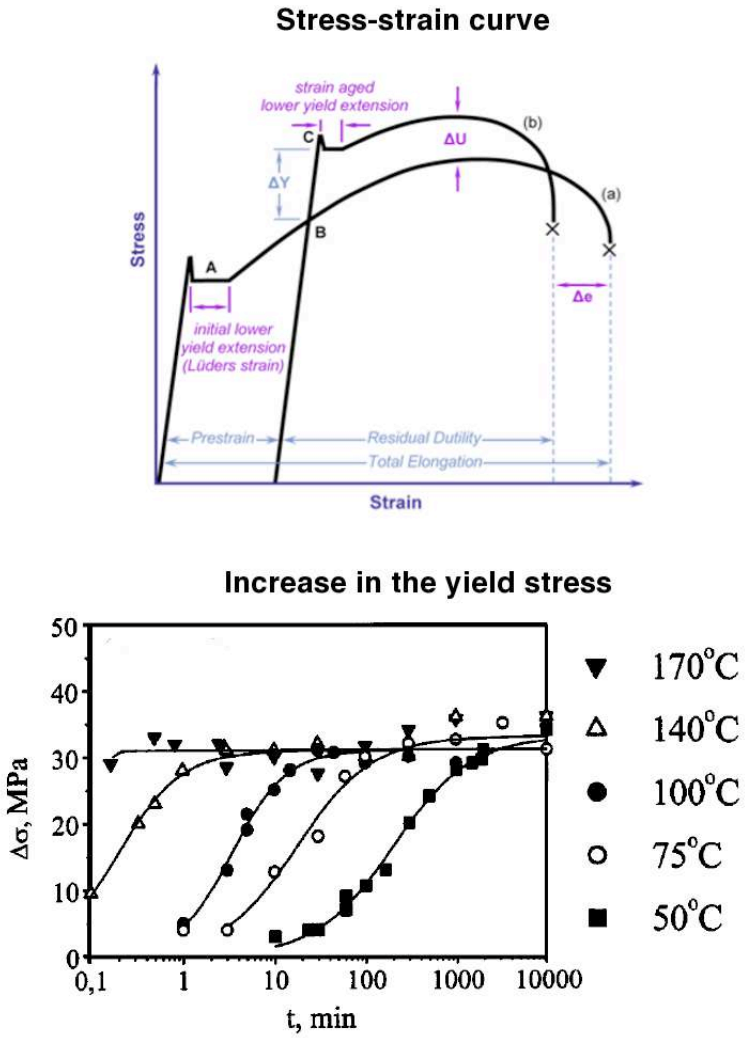

Figure 1: Typical stress-strain curve for Fe-C systems and the variation in the yield stress at different temperatures (figure adapted from Ref. [De 2000]).

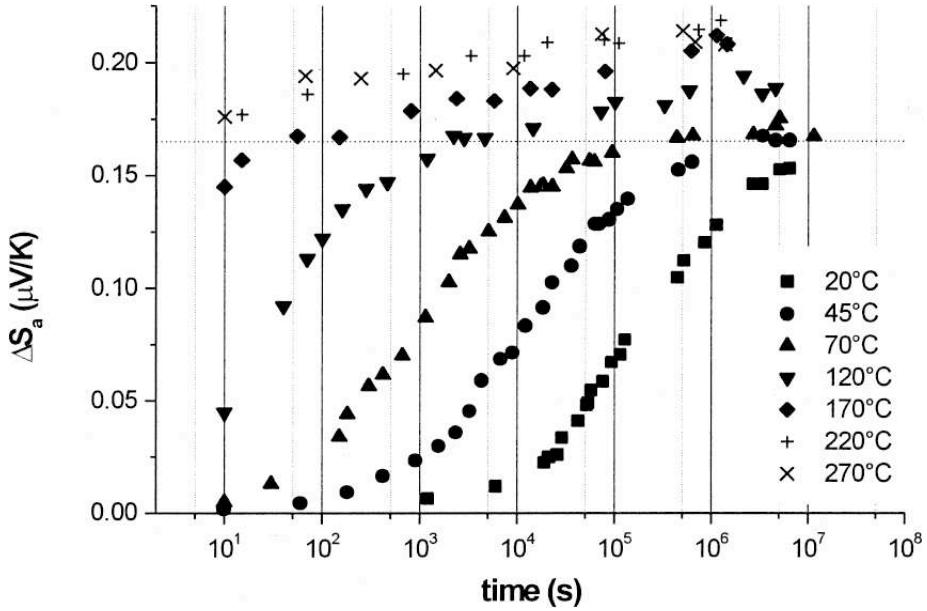

Figure 2: TEP variation of a cold worked ULC steel (50% of reduction) aged at different temperatures. Figure taken from Ref. [Lavaire 2001].

in his doctoral thesis [Chang 1985], provided the first experimental evidence of carbon Cottrell atmospheres in low carbon lath martensites by superimposing field ion micrographs and gated carbon images taken in the imaging atom probe. Many other experimental works have been published since then where atom probe techniques were used to visualize impurity segregation at line defects [Wilde 2000, Miller 2003, Sherman 2007]. For the sake of example, Fig. 3 shows a 3D carbon atom map in a martensite specimen. The morphology and the concentration profile of the interconnected carbon-enriched regions indicate that the carbon atoms are trapped in Cottrell atmospheres in dislocation tangles in the martensite matrix [Sherman 2007].

From a technological point of view, the dislocation pinning by solutes results in deleterious plastic instabilities that can represent a serious hindrance to the steel-based manufacture and applications. The two types of instabilities associated with strain aging are the Lüders bands (non-uniform yielding) and the Portevin-LeChatelier (PLC) effect [Graff 2004]. The Lüders bands are localized bands of plastic deformation that propagate in the material as a consequence of SSA. As it can be clearly discerned in Fig. 4, the Lüders bands delineate plastically deformed and undeformed zones in the analyzed specimen upon the application of tensile stress. The PLC effect, in turn, is characterized by a serrated stress-strain curve due to the pinning/unpinning of dislocations and is related to another strain aging phenomenon, called dynamic strain aging (DSA). In contrast with SSA, which

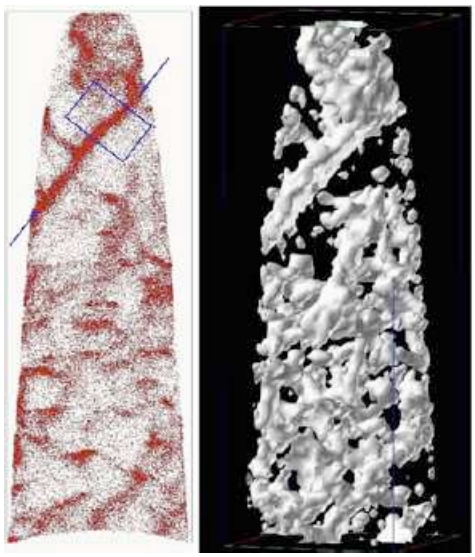

Figure 3: 3D carbon atom map (left) and the corresponding 1.3 at%C isoconcentration surfaces (right) in a martensite specimen obtained from atom probe tomography data. The morphology and the concentration profile of the interconnected carbon-enriched regions indicate that the carbon atoms are trapped in Cottrell atmospheres in dislocation tangles in the martensite matrix. Figure adapted from Ref. [Sherman 2007].

takes place during the specimen rest time, DSA manifests during the specimen deformation. It is currently associated with the diffusion of impurities to a mobile dislocation temporarily arrested at obstacles such as a dislocation forest. Strain localization related to the PLC effect is usually seen as a sequence of shear bands, as one can see in Fig. 5.

Given its technological importance, it is natural that strain aging has been attracting so much attention for decades. From a theoretical point of view, some simple analytical models, based mostly on classical elasticity theory, were proposed and helped to explain many aspects of strain aging, despite the limitations inherent to continuum approaches applied to an atomistic problem. In recent years, owing to the fact that computer power enormously increased, computer simulations with methods that fully take into account the atomistic details (e.g., molecular dynamics) became possible.

The work presented in this thesis can be seen as part of a larger effort to apply atomistic simulations to the investigation of the properties of Fe-C systems under stress conditions. The milestones of this long term project are outlined in the following:

1) development of interatomic potentials to be used with atomistic simulations (e.g., the Fe-C interatomic potential presented in Ref. [Becquart 2007]);

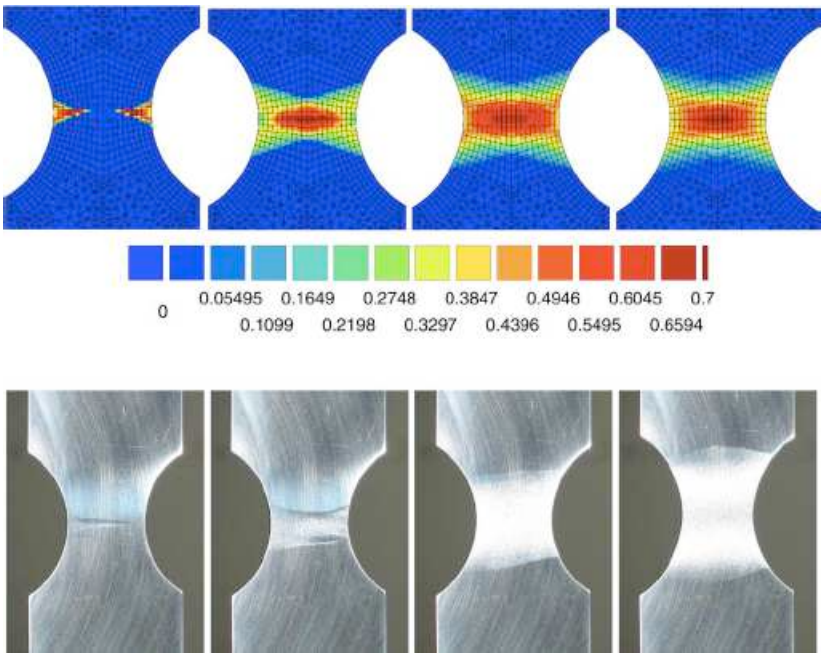

Figure 4: The Lüders behavior in a simulated (finite elements) and an experimental smooth U-notched specimen. The plastic strain maps are shown at different overall displacement levels (0.2, 0.5, 1.2, 1.8 mm). Figure taken from Ref. [Graff 2004].

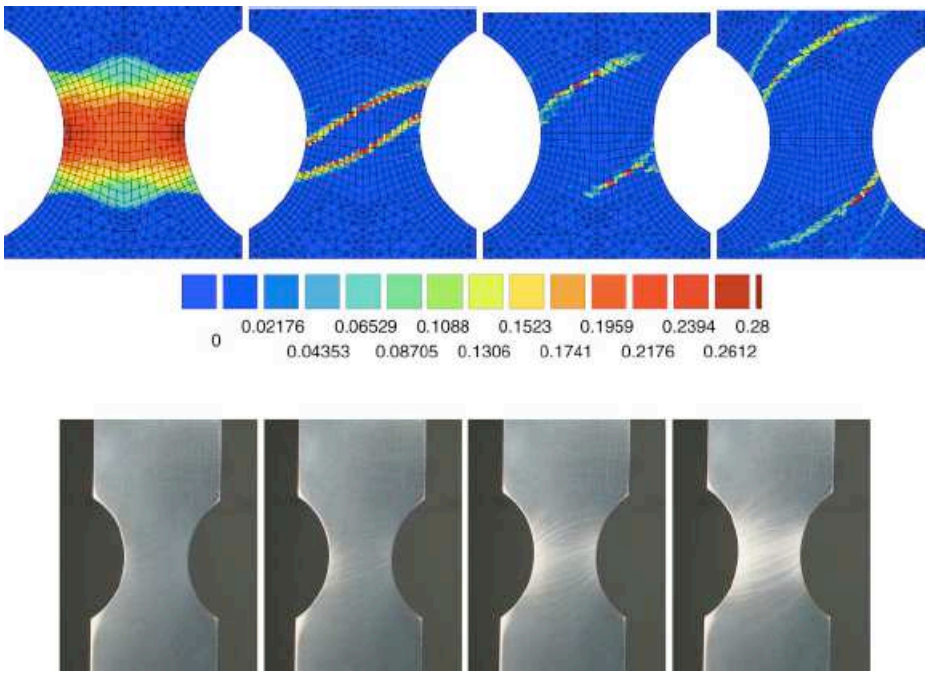

Figure 5: The PLC effect in a simulated (finite elements) and an experimental smooth U-notched specimen. The plastic strain rate maps are shown at different overall displacement levels (0.3, 0.5, 0.7, 1 mm). Figure taken from Ref. [Graff 2004].

2) carbon diffusion in bcc iron under the application of homogeneous stress (e.g., modeling the carbon Snoek peak [Garruchet 2008]);

3) carbon diffusion in the non-homogeneous stress field created by dislocations, leading to the Cottrell atmosphere formation (first stage of static strain aging);

4) further stages of static strain aging, when carbide precipitation takes place in the dislocation vicinity;

5) dislocation unpinning and glide under the application of an external stress.

This thesis partially addressed point 3 above. It should be mentioned that, such as many problems in materials science, modeling SSA is inherently a multiscale problem (see Fig. 6). This kind of problem, which spans multiple spatial and temporal scales, is very challenging, both theoretically and experimentally. On one hand, it is out of reach to treat all involved scales in the framework of a single physical model. On the other hand, even if it is possible and necessary, it is not trivial to link the results and conclusions of experiments or models obtained at different scales. For the time being, the scope of the present project is restricted to the atomic (nanometer) scale, where the behavior of individual atoms are explicitly taken into account.

Although the underlying (atomic scale) mechanism of SSA is well-established in general terms (i.e., carbon and other impurities migrate and pin dislocations), many aspects of this important phenomenon still have to be tackled. For example, in the theoretical corner, there are very few studies that actually model the effect of the dislocation stress field on carbon diffusion at the atomic scale. Indeed, most of the works on the subject refer to the application of simple kinetic models or, at the best, extract their conclusions from static calculations of carbon-dislocation binding energies. A key point in the multiscale materials modeling is the choice of the simulation tool which is the most appropriate for the task to be accomplished. Because diffusion in the solid state is a thermal-activated phenomenon that proceeds slowly (minutes or even hours) compared to the typical time scale (a few nanoseconds) that can be achieved by molecular dynamics, which is the standard method for computer simulations at the atomic scale, alternatives have to be considered. One of the most promising is kinetic Monte Carlo. With kinetic Monte Carlo, computer simulations can overcome the nanosecond barrier and even achieve the experimental time scale (see Fig 6), while describing accurately the diffusional processes. As such, it has been the preferential method used throughout this PhD work.

The manuscript is organized as follows:

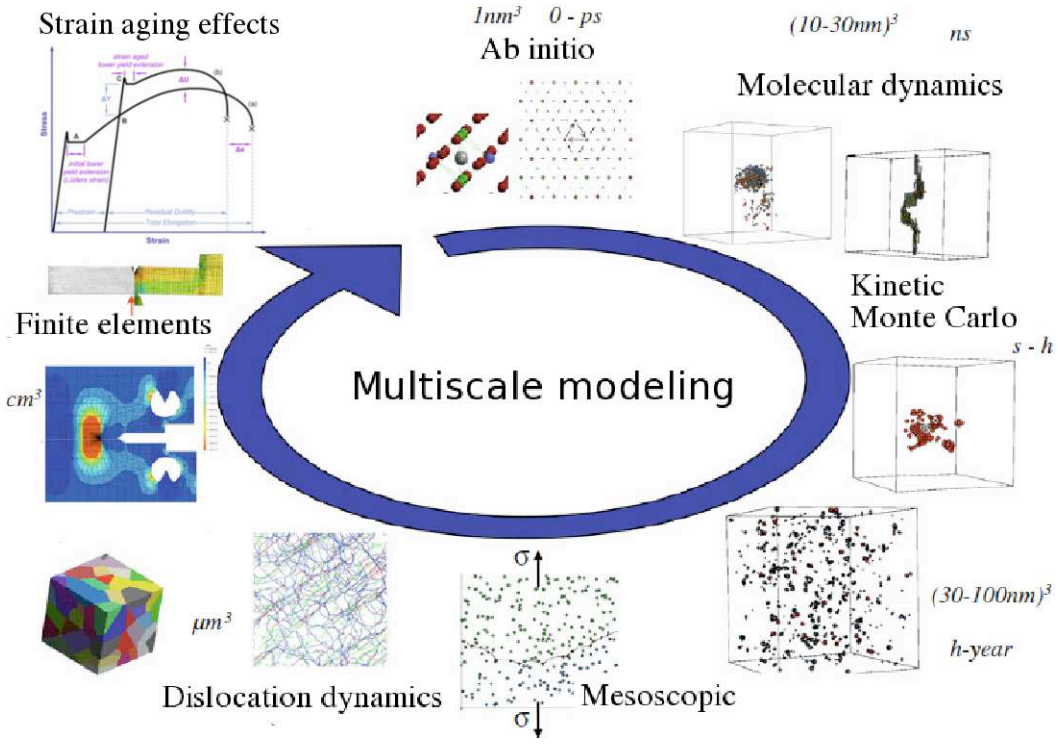

Figure 6: Representation of multiscale materials modeling according to the different scales involved. Figure adapted from Ref. [Becquart 2010].

- Chapter 1 shortly introduces the computational methods that have been used in this work, emphasizing atomistic kinetic Monte Carlo;
- Chapter 2 focuses on the effect of the long range stress field created by an edge and a screw dislocation on carbon diffusion, using molecular statics to obtain carbon-dislocation binding energies and energy barriers for carbon migration, as well as atomistic kinetic Monte Carlo to simulate a carbon atom diffusing in the neighborhood of the line defect;
- Chapter 3 presents the comparison of carbon-dislocation binding energies and energy barriers for carbon migration obtained by molecular statics in Chapter 2 with results of anisotropic elasticity theory applied to the interaction between the point and the line defect;
- Chapter 4 consists of a still preliminary investigation of carbon behavior in the core of an edge or a screw dislocation (i.e., pipe diffusion);
- Chapter 5 reports the results of a statistical physics model that employs the carbon-dislocation binding energies presented in Chapter 2 to predict carbon distribution in the stress field of dislocations;

- Appendix A briefly describes the interatomic potential used in the atomistic simulations, including a modification done in the Fe-C pairwise function in the course of this PhD work.

Chapter 1

Methods

Abstract

Here we present an overview of the computational methods employed in the investigations reported in the subsequent chapters. Molecular statics provides the total potential energy of an atomistic system in the vicinity of a local energy minimum (i.e., a system configuration at $T = 0$ K). The temporal evolution of an atomistic system at $T > 0$ K, in turn, can be simulated by molecular dynamics or atomistic kinetic Monte Carlo, either method presenting specific strengths and weaknesses. Atomistic kinetic Monte Carlo requires that the energy barriers for the transitions that the system can undergo are known, thus some methods used to find saddle points are briefly introduced.

1.1 Molecular statics

Molecular statics comprises a wide family of algorithms that, applied to atomistic systems, allows to optimize the structure of a collection of atoms in order to reach a local energy minimum in the potential energy surface. In other words, it refers to the specific problem of finding out a final configuration with coordinates $\{\vec{r}_f^N\}$ for which the total interatomic force $|\vec{F}^N| = |\sum_{i=1}^{N} \vec{F}_i| \rightarrow 0$, where N is the number of atoms, starting from a configuration with coordinates $\{\vec{r}_s^N\}$. In practical terms, $\{\vec{r}_f^N\}$ will be the first atomic configuration close to $\{\vec{r}_s^N\}$ for which $|\vec{F}^N| \leq \epsilon$, where ϵ is an arbitrarily small force tolerance (typical values ranging from 10^{-2} to 10^{-4} eV/nm).

Although damped molecular dynamics algorithms are frequently used to optimize atomic structures, molecular statics is inherently different from molecular dynamics because the former method does not produce physically meaningful atomic trajectories. In fact, only the final configuration has a physical meaning, namely, the ground state of the considered system (i.e., a system state at $T = 0$ K). Since temperature is not taken into account in molecular statics simulations, the particle momenta $\{\vec{p}^N\} = 0$.

In our work, we preferentially used the conjugate gradient (CG) algorithm to perform geometry optimization. This is by far the most widely used algorithm for this purpose. The method is shortly described in the following. CG is implemented as a sort of iterative method for the solution of systems of linear equations in the form $\mathbf{Ax} = \mathbf{b}$, where $\mathbf{A}$ is a square positive-definite matrix, $\mathbf{b}$ is a known vector, and $\mathbf{x}$ is the vector to be determined. Concerning the problem of minimizing the energy of a collection of atoms, it means that, at each CG iteration, for every atom in the system, the force $\vec{F}_i$ acting on the i-th atom located at $\vec{r}_i$ is calculated from the gradient of the system potential energy $\vec{\nabla}_i E$, and then this atom is displaced in the direction of energy decrease as well as in the direction perpendicular to its previous displacement. CG normally allows to reach a relaxed configuration (i.e., a local energy minimum in the potential energy surface) within a certain tolerance ϵ in a relatively small number of iterations (compared to the system size) by monotonically improving approximations to the exact solution. To a comprehensive description of the conjugate gradient method, the interested reader is referred to Ref. [Shewchuk 1994], which is properly entitled "An Introduction to the Conjugate Gradient Method Without the Agonizing Pain", or to Ref. [Saad 2003].

Throughout this work, we used the Large-scale Atomic/Molecular Massively Parallel Simulator (LAMMPS) code [Plimpton 1995] to perform molecular statics

(and also molecular dynamics) simulations. To date, LAMMPS is one of the most efficient codes available for this purpose. It is fully parallelized, which makes it a good choice for the simulation of moderate-to-large atomistic systems on multiple processors.

1.2 Molecular dynamics

In computer simulations, molecular dynamics (MD) is the standard method used to numerically simulate the evolution in time of an atomistic system by integrating Newton's equations of motion for all its particles. Time in MD simulations is discretized and the time step Δt is normally chosen so as to be as small as the fastest atomic vibrations ($\approx 10^{-15}$ s). In this short time interval, the forces acting on the particles are assumed to be constant. Numerical integration is carried out by using finite difference methods. Some efficient numerical integrators are available; in this work, we used the Velocity Verlet algorithm [Swope 1982], based on the original algorithm proposed by L. Verlet [Verlet 1967]. The position $\vec{r}_i$ and the velocity $\vec{v}_i$ of the i-th particle at $t + \Delta t$ according to the Velocity Verlet algorithm is given by the following equations:

$$\begin{cases} \vec{r}_i(t+\Delta t) = \vec{r}_i(t) + \vec{v}_i(t)\Delta t + \dfrac{\vec{F}_i(t)}{2m_i}\Delta t^2 \\ \vec{v}_i(t+\Delta t) = \vec{v}_i(t) + \dfrac{1}{2m_i}\left[\vec{F}_i(t) + \vec{F}_i(t+\Delta t)\right]\Delta t \end{cases} \tag{1.1}$$

where m_i is the particle mass and the force $\vec{F}_i$ acting on the particle at any instant t is calculated as follows:

$$\vec{F}_i(t) = -\vec{\nabla}_i E = -\left(\frac{\partial E}{\partial x_i}\hat{i} + \frac{\partial E}{\partial y_i}\hat{j} + \frac{\partial E}{\partial z_i}\hat{k}\right) \tag{1.2}$$

The total potential energy E of the system at any instant of time is determined from the relative positions of the particles, which interact with each other through an interatomic potential, and is evaluated at each MD step. Solving Eq. (1.2) for every particle in the system is the most computationally expensive task to be carried out by the MD algorithm.

Most of the molecular dynamics codes available to the community of computational materials scientists are complex software packages (e.g., LAMMPS, NAMD, Amber, Gromacs). In spite of it, all MD programs share the same basic logic. A minimalist outline of a typical MD program is presented in the following:

- A simulation protocol defines the general conditions under which the system

will be simulated: initial temperature, initial pressure, target temperature, target pressure, boundary conditions, number of MD steps, time step (Δt), etc.

- System initialization: initial positions and velocities are assigned to the particles, and all necessary information about the system, such as the interatomic potential, is provided.

- The simulation itself is launched. MD is an iterative method, where each iteration corresponds to a time step Δt. At each iteration:

  1) The total potential energy of the system as a function of particle positions is calculated.

  2) The forces acting on all particles are computed (Eq. (1.2)).

  3) The new positions and velocities of the particles are computed by integrating the equations of motion with a suitable algorithm, such as the aforementioned Velocity Verlet algorithm (Eq. (1.1)).

  4) The total simulated time is incremented by Δt.

  5) Optionally, the quantities of interest (e.g., the positions and velocities of the particles) are stored into appropriate data files for post-processing.

  6) If the total number of MD steps is reached, the simulation stops; otherwise, the next iteration starts.

The trajectories simulated by MD should be long enough to provide representative samples of the system configurations. The number of MD steps required to perform meaningful statistical analysis depends on the simulated temperature and also on the characteristics of the system under study. As a general rule, molecular dynamics simulations of liquids and soft matter can be shorter and performed at lower temperatures than simulations of solids, owing to the higher mobility of the atoms in the former case.

Molecular dynamics, for the reasons explained in the next section, was not the principal simulation method that we have employed so far. On the other hand, in the sequence of this work, it is the natural choice for a number of perspective simulations (e.g., unpinning of a dislocation arrested by a Cottrell atmosphere). A detailed discussion on molecular dynamics can be found in Ref. [Frenkel 2002].

1.3 Atomistic kinetic Monte Carlo

1.3.1 Motivation of the algorithm

The erratic walk of a carbon atom in a bcc iron matrix is an example of diffusion in the solid state. This is one out of many important physical phenomena that are ruled by rare events (i.e., discrete transitions that usually take a long time to occur compared to the atomic vibrations). Transition state theory states that most of the time the system will be found in the vicinity of a stable state, which is a configuration that corresponds to a local energy minimum in the potential energy surface [Marcelin 1915, Wigner 1932, Eyring 1935]. A transition occurs when the system performs a jump to another stable state, adjacent to the current one, surpassing the energy barrier that separates the two states in a sudden move. As such, the long time evolution of this system can be described in terms of a chain of discrete transitions.

In principle, MD simulations can be used to simulate this kind of system, too. In fact, there is no technical issue that prevents this. However, in practice, a well-known drawback of molecular dynamics is that the time step Δt in Eq. (1.1) has to be very small (in the order of 10^{-15} s). As a consequence, in MD simulations, much of the computational effort is done to simulate the atoms vibrating around their equilibrium positions and such vibrations give no contribution to particle diffusion. Furthermore, the small Δt imposes a drastic limit on the time scale that can be achieved by MD simulations (typically, a few nanoseconds) in a reasonable CPU time, even in large parallel machines, while a transition, depending on the simulated temperature, may take a long time to occur.

On the other hand, kinetic Monte Carlo (KMC) [Voter 2002, Fichthorn 1991] is specially suitable to study this kind of state-to-state dynamics. It belongs to the Monte Carlo family of algorithms that use random numbers to solve a broad range of numerical problems. Since KMC makes the system evolve dynamically, it is in sharp contrast with other Monte Carlo algorithms, like Metropolis [Metropolis 1953, Frenkel 2002], which are time-independent and are used to find configurational free energy minima only. In contrast with MD, the time step in KMC is not fixed but stochastically determined at each iteration. Moreover, every KMC iteration is associated with a system transition; the atomic vibrations around an energy minimum between two transitions are neglected. The KMC approach allows to reach typical experimental time scales (hours, days, in some cases, even years, depending on the system under study).

1.3.2 The AKMC algorithm

Among the available KMC algorithms, atomistic kinetic Monte Carlo (AKMC) is one of the simplest [Becquart 2009]. In typical AKMC, the geometry of a rigid lattice is derived from the actual geometry of the atomistic system to be studied. This is to say that, bearing in mind the problem of an interstitial atom (carbon) diffusing in a crystal (bcc iron), every point on the AKMC lattice corresponds to a site in the crystal that is available to be occupied by the interstitial atom. Furthermore, all possible transitions that this kind of system can undergo, as well as their corresponding probabilities, can be obtained just once and then tabulated into a reusable event catalog, which enormously speeds up AKMC simulations. Concerning the present model, we have implemented an AKMC code based on the residence time algorithm derived by Young and Elcock for the study of vacancy migration in ordered alloys [Young 1966].

A brief description of the AKMC algorithm used in this work (Algorithm 1.1) is given next. The central quantity in AKMC, calculated at each iteration, is the residence time τ, which determines how long the system remains in a given state before jumping to one of the adjacent states. In order to calculate it, all transition rates to escape such a state must be known. The transition rate $R_{i\to j}$, where i is the current state and j is one of the adjacent states, is obtained by:

$$R_{i\to j} = w_0 \exp\left(\frac{-E^m_{i\to j}}{kT}\right) \tag{1.3}$$

where w_0 is the attempt frequency (usually in the order of 10^{13} Hz), k is the Boltzmann constant, T is the simulated temperature, and $E^m_{i\to j}$ is the energy barrier (at $T = 0$ K) to be surpassed in order to the system escapes the current state i to the adjacent state j (see Fig. 1.1). According to harmonic transition state theory [Vineyard 1957], the energy barrier for the transition $i \to j$ is given by the following simple equation:

$$E^m_{i\to j} = E^{sp} - E^{min}_i \tag{1.4}$$

where E^{sp} is the total energy of the system at the saddle point (i.e., the transition state) and E^{min}_i is the total energy of the system at the state i. Hence, the residence time τ is computed as:

$$\tau = -\frac{\ln r_1}{\Omega_i} \tag{1.5}$$

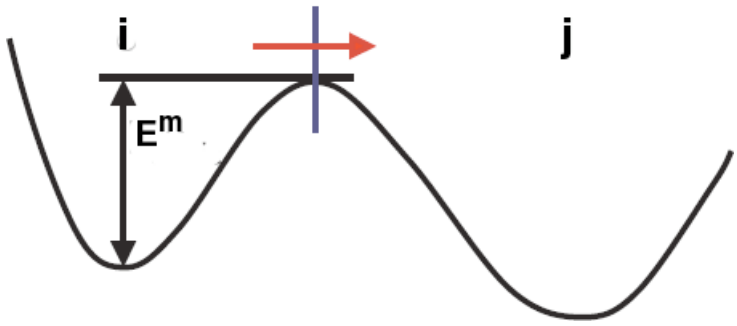

Figure 1.1: Illustration of a transition taking the system from state i to j (direction of the red arrow) by overcoming the energy barrier E^m.

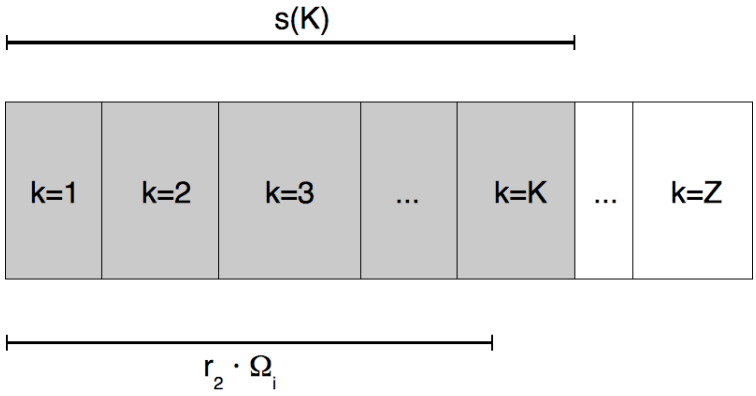

Figure 1.2: The K-th transition is chosen because its assigned value of $s(k)$ intercepts $r_2 \cdot \Omega_i$.

Note that τ, in Eq. (1.5), depends on all transition rates, not only on the rate to escape to state j: $\Omega_i = \sum_{k=1}^{Z} R_{i\to k}$ is the sum of the rates of all possible Z transitions that the system can undergo from the current state i; r_1 is a random number in the range of $(0, 1]$.

As soon as τ has been calculated, it is added to the total time elapsed until then, and a transition is selected to make the system advance to the next state. This is done by applying the method introduced by Bortz, Kalos, and Lebowitz in Ref. [Bortz 1975]. A quantity $s(k) = \sum_{k=1}^{K} R_{i\to k}$ is defined and its value is assigned to the K-th transition, with $K \leq Z$ (Z is the total number of transitions that are allowed from the current state i). Then, a random number r_2 in the range of $[0, 1]$ is generated and the transition corresponding to the smallest $s(k)$ that is greater than $r_2 \cdot \Omega_i$ will be chosen (see Fig. 1.2). At this point, a single AKMC iteration is finished. The program will proceed until the maximum number of AKMC steps (or any other stopping condition) is reached.

In order to provide an estimate of the efficiency of Algorithm 1.1, the simulation of a trajectory consisting of 1,000 steps lasts less than one second running

on a single processor (Intel Core 2 Duo, 2.4 GHz).

Algorithm 1.1 The AKMC algorithm used in this work.

```
Load the catalog containing the allowed transitions and the corresponding rates;
Parameter: maximum number of trajectories N_traj to be generated;
Parameter: maximum number of steps (iterations) per trajectory N_steps;
a = 1;
while a ≤ N_traj do
    t = 0;
    Select an initial state;
    b = 1;
    while b ≤ N_steps do
        if Stopping condition is not achieved then
            Compute Ω_i;
            Generate a random number r_1;
            Compute τ;
            t = t + τ;
            Generate a random number r_2;
            s(:) = 0;
            for all States k adjacent to the current state i do
                Compute s(k);
                if s(k) ≥ r_2 · Ω_i then
                    Pick the K-th state as the new current state;
                    Exit the loop;
                end if
            end for
            b = b + 1;
        end if
    end while
    a = a + 1;
end while
```

1.4 Saddle point finding methods

1.4.1 The saddle point problem

The energy barriers calculated by Eq. (1.4) are entry parameters of the AKMC code, thus they have to be obtained by other means. It is straightforward to obtain the total energy of local energy minima with molecular statics simulations. On the other hand, even if saddle points also are critical points, they are neither minima nor maxima in the potential energy surface. A saddle point corresponds to a point for which the Hessian matrix (the second derivative of the potential

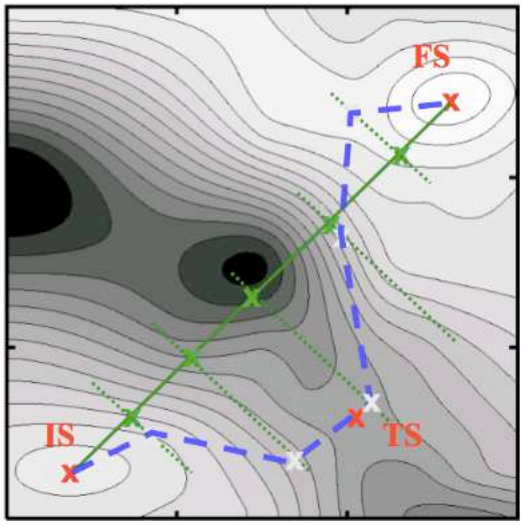

Figure 1.3: The drag method: the system is moved from the initial state (IS) to the final state (FS) by small steps and relaxed in the (hyper)plane perpendicular to the IS-FS direction. The transition state (TS) is taken as the point with the highest energy along the minimum energy path. Figure taken from http://www.fhi-berlin.mpg.de.

energy E with respect to the positions of the particles) is indefinite. In principle, it means that saddle points could be calculated from the Hessian matrix. In practice, this is computationally too expensive to be accomplished, then approximative methods have been proposed. An authoritative review by Henkelman and co-workers on some of the main methods currently used to find saddle points can be found in Ref [Henkelman 2000a]. A brief description of the methods employed in this work follows.

1.4.2 The drag method

It is the simplest method to search for saddle points. The drag method requires the knowledge of two states that are energy minima of the system in the potential energy surface. Starting from the initial state, small fixed length displacements (steps) are applied to the system towards the final state (see Fig. 1.3). At each step, the system is allowed to relax only in the hyperplane perpendicular to the drag line (i.e., the line connecting the initial and the final state). The direction followed by the system stepwise is often called the reaction coordinate. As soon as the minimum energy path between the two energy minima is revealed, the position with the highest energy along this path will be taken as the best estimate for the saddle point.

The accuracy of the drag method is inversely proportional to the step length.

If the step length is too large, the saddle point is likely to be missed by far. At the beginning of our work, a modification of the drag method was implemented where the step size was no longer fixed. The first step that makes the system leave an energy minimum can be very large (1/3 of the minimum-to-minimum distance, for instance), and the subsequent ones should be smaller (we used 1/10 of that distance as a first guess). At each step, $\vec{F} \cdot \hat{R}$ is calculated, where $\vec{F}$ is the force vector and $\hat{R}$ is the unit vector that points from the starting energy minimum to the destination one (i.e., it defines the reaction coordinate). If the scalar product is less than zero, the force is trying to bring the system back to the initial energy minimum and then it has to be dragged in the direction of $\hat{R}$ in order to climb up the potential energy surface. On the contrary, if the the scalar product is greater than zero, then the system surpassed the saddle point and is trying to reach the other energy minimum. Then the system is brought back to the previous step, a new step size is defined as half the current one, and the system is moved again towards the second energy minimum. This procedure is iteratively applied until the step size is within an arbitrarily small tolerance or, much less likely, the scalar product $\vec{F} \cdot \hat{R}$ becomes zero (that is, the system is exactly at the saddle point). It is not possible to draw a minimum energy path with this method but, on the other hand, this modification is more efficient and accurate to find a saddle point than the original drag method implementation.

In spite of its easy implementation, it should be pointed out that the drag method is not reliable in all situations and, in fact, it completely fails in many. Since a more sophisticated and reliable method (the nudged elastic band method, see below) became available in LAMMPS, the drag method will be no longer used in the context of the current project.

1.4.3 The nudged elastic band method

The nudged elastic band (NEB) method became, in recent years, the state-of-the-art method to draw a minimum energy path between two known energy minima and estimate the saddle point [Henkelman 2000a]. In the NEB method, a set of replicas ("images") of the system is created along the path connecting the two energy minima (see Fig. 1.4). Those replicas form a chain where consecutive replicas are connected by fictitious springs (i.e., the elastic band), which prevent that the chain collapses on the energy minima. The actual minimum energy path is revealed when the total energy of the string of replicas is minimized by a suitable algorithm.

A modified version of the NEB method is the Climbing Image Nudged Elastic

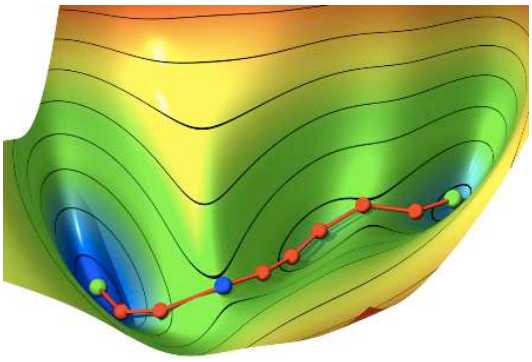

Figure 1.4: The NEB method: representation of a chain of images in the potential energy surface. Each image is a snapshot of the system at that position along the minimum energy path that connects two energy minima (green spheres). The blue sphere is the image with the highest energy and therefore it is supposed to be the image that is closest to the saddle point.

Band (CI-NEB) method. After minimizing the energy of all images taken together, the highest energy image is disconnected from its neighbors and is driven up to the saddle point by maximizing its energy along the direction defined by the band. CI-NEB has the obvious advantage that it provides not only the saddle point, but also a global view of the minimum energy path between two energy minima. It allows to identify, for instance, whether more than one saddle point is found along the minimum energy path.

1.4.4 The activation-relaxation technique

In contrast with "chain-of-states" methods (like drag and NEB), the activation-relaxation technique (ART) [Barkema 1996] is an example of method to search for saddle points when only one energy minimum is known. The method can be split into two steps:

1) **Activation**: one of the atoms of the system is slightly displaced in order to create a non-zero force in the system. Then the whole system is enforced to go up hill in the potential energy surface up to arrive to a saddle point;

2) **Relaxation**: once at the saddle point, the system is relaxed towards a new energy minimum in the potential energy surface, thus completing a transition (event).

While the relaxation step can be achieved by any of the well known methods for minimizing the energy of a system, the activation step is more challenging to be implemented. ART, in the original formulation by Barkema and Mousseau,

accomplishes it by introducing a modified force, defined as follows:

$$\vec{G} = \vec{F} - (1 + \alpha)(\vec{F} \cdot \hat{R})\hat{R} \tag{1.6}$$

where $\vec{F}$ is the force derived from the interatomic potential energy, $\hat{R}$ is the unit vector pointing from the energy minimum to the current position, and α is a positive number. Thus the new force $\vec{G}$ is opposite to $\vec{F}$ in the direction parallel to $\hat{R}$ and equal to $\vec{F}$ in all other directions. At the saddle point, $|\vec{G}| = |\vec{F}| = 0$ and the activation step stops. Some improvements have been introduced by other authors in the ART method, as one can see, for instance, in the work by Cancés *et al* [Cancès 2009].

In the context of this PhD work, we have implemented a simplified version of the ART method, namely, the translation-and-relaxation (TaR) method. It starts by randomly displacing a single atom (in our case, the carbon atom) from the position that corresponds to the energy minimum. Then constrained molecular statics is carried out where the carbon atom is allowed to relax only on the plane perpendicular to $\hat{R}_C$, which is the unit vector pointing to the current carbon position from its initial position. After geometry optimization, $\hat{R}_C$ is updated with the new carbon position and a small displacement of the carbon atom is performed in the direction pointed out by $\hat{R}_C$. Constrained molecular statics is performed again. This process, which clearly corresponds to the activation step in the original ART method, will be repeated while the scalar product $\vec{F}_C \cdot \hat{R}_C < 0$, where $\vec{F}_C$ is the force acting on the carbon atom evaluated before each translation. When $\vec{F}_C \cdot \hat{R}_C > 0$, the carbon atom crossed the position corresponding to the saddle point and the geometry of the system is fully relaxed so as to allow the carbon atom moves towards an adjacent energy minimum. This can be seen as the relaxation step in the original ART method.

Although the TaR method could be used to provide an estimate of the saddle point, it has been used in this work to find the unknown energy minima positions around an initial energy minimum (i.e., it has been used to build a network of energy minima as seen in Fig. 1.5), while the saddle points have been obtained with CI-NEB.

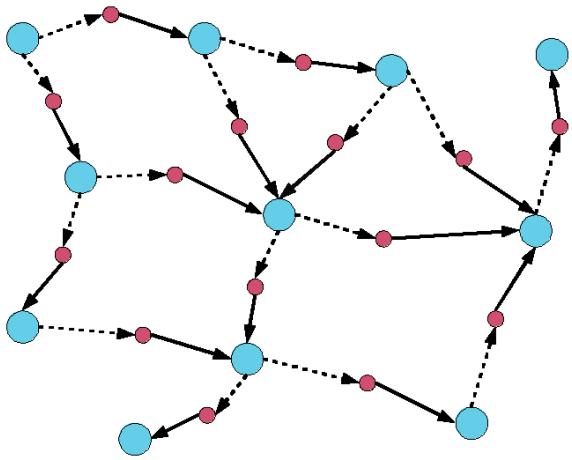

Figure 1.5: The TaR method: a network of local energy minima (big blue circles) connected by saddle points (small red circles) can be built starting from only one energy minimum by performing many activation (dashed arrows) and subsequent relaxation (solid lines) steps.

Chapter 2

Effect of the stress field of dislocations on carbon diffusion

Abstract

Carbon diffusion near the core of an edge and a screw dislocation in α-iron has been investigated by means of an atomistic model that brings together molecular statics and atomistic kinetic Monte Carlo. Molecular statics simulations with a recently developed EAM potential have been carried out in order to obtain atomic configurations, carbon-dislocation binding energies, and the activation energies required for carbon hops in the neighborhood of the line defect. Using information gathered from molecular statics, on-lattice AKMC simulations have been performed for temperatures ranging from 300 K to 600 K, so as to study the behavior of a carbon atom as it interacts with the dislocation stress field before being trapped by the line defect.

2.1 Introduction

Much effort has been done to model the strain aging behavior of steels and other metallic alloys since Cottrell and Bilby proposed a first kinetic model to describe the initial stage of SSA [Cottrell 1949], which is the Cottrell atmosphere formation. In their model, the total number N_s of segregated carbon atoms per unit length of dislocation in time t is given by:

$$N_s = N_0 3 \left(\frac{\pi}{2}\right)^{\frac{1}{3}} \left(\frac{ADt}{kT}\right)^{\frac{2}{3}} \tag{2.1}$$

where N_0 is the number of atoms in solid solution per unit of volume, D is the diffusion coefficient of the segregating atom, A is a parameter that determines the intensity of carbon-dislocation interaction[1], k is the Boltzmann constant and T is temperature. It should be pointed out that Cottrell and Bilby's model does not take into consideration carbon depletion in the matrix, thus it fails to describe the kinetics as aging proceeds. Harper later modified the model in order to consider the lowering of carbon concentration in the dislocation surroundings [Harper 1951]:

$$\frac{N_s}{N_0} = 1 - \exp\left[-3L \left(\frac{\pi}{2}\right)^{\frac{1}{3}} \left(\frac{ADt}{kT}\right)^{\frac{2}{3}}\right] \tag{2.2}$$

In Eq. (2.2), the rate of carbon atoms already segregated to dislocations increases as carbon concentration in solid solution exponentially decays. As Harper's model neglects back diffusion to the matrix, it is expected to work only for low atmosphere densities. A "generalized" form of Harper's equation that has been preferred in recent studies is the JohnsonMehl-Avrami equation, which can be written as:

$$\frac{N_s}{N_0} = 1 - \exp\left[-(Kt)^n\right] \tag{2.3}$$

where the parameter $K = K_0 \exp\left(-E^m/kT\right)$ allows to obtain the apparent activation energy of the aging process and n can assume values different from 2/3. Indeed, deviations from 2/3 in the value of n are associated with a change in the impurity diffusion mechanism [Leslie 1961, Bullough 1959, Buono 1998]. For instance, if diffusion is restricted to the core of a dislocation (pipe diffusion), $n \to 1/3$, and if the absorbing particle is a precipitate (e.g., a growing cementite particle), $n \to 1/2$.

[1] In original Cottrell and Bilby's formulation, the interaction energy of a carbon atom at a location (r, θ), in polar coordinates, with respect to an edge dislocation is given by $E^{inter} = A \sin\theta / r$.

In a further development from Harper's and other's works [Ham 1959, Bullough 1959, Muba 1962], Hartley derived a model where the increase in yield stress during aging is assumed to be due only to the reduction of mobile dislocation length, which is in turn supposed to be proportional to the linear concentration of solute atoms on the dislocations [Hartley 1966]. Hartley successfully applied his model to the investigation of the effect of oxygen segregation to dislocations in the aging of unalloyed tantalum. The kinetics of strain aging from the measurement of changes in yield stress according to Hartley's model is given by the following equation:

$$\begin{aligned} \frac{\Delta\sigma}{\Delta\sigma_{max}} &= K_1 + K_2(at)^n \\ &= K_1 + K_2\left(\frac{Dt}{T}\right)^n \end{aligned} \tag{2.4}$$

where $\Delta\sigma/\Delta\sigma_{max}$ is the fractional increase in the yield stress during aging, t is the aging time, K_1 and K_2 are constants that depend on the test conditions (the meaning of which is not very clear in Hartley's derivation), D is the diffusion coefficient of the segregating atom, T is temperature, and $n = 2/3$ (in his original work).

Despite the fact that Cottrell atmospheres remained a conjecture for decades, the simple analytical models introduced above have been widely used in the interpretation of aging experiments and proved to be consistent with the observed kinetics, at least for small t. In recent years, three-dimensional atom probe techniques allowed to go further and image interstitial impurities distributed around dislocations in metallic alloys [Chang 1985, Blavette 1999, Cadel 1999, Wilde 2000, Thompson 2007, Miller 2006], providing the missing direct experimental evidence of Cottrell atmospheres. However, in spite of representing a substantial advance in the experimental side, these techniques provide only a static picture of the atmosphere. In other words, the impurity diffusion to dislocations and the subsequent Cottrell atmosphere formation remains a challenge for these techniques. In this context, numerical simulations, which strongly benefited from the recent increase in computing power, may come and fill the gap between microscopic and macroscopic experiments and models by offering an atomistic view of impurity diffusion near and to dislocations [Ramasubramaniam 2008, Hin 2008, Veiga 2010].

This chapter presents computer simulations of carbon diffusion in the moderately strained surroundings of an edge and a screw dislocation (the dislocation core itself has not been considered except as a trap for carbon). Our model

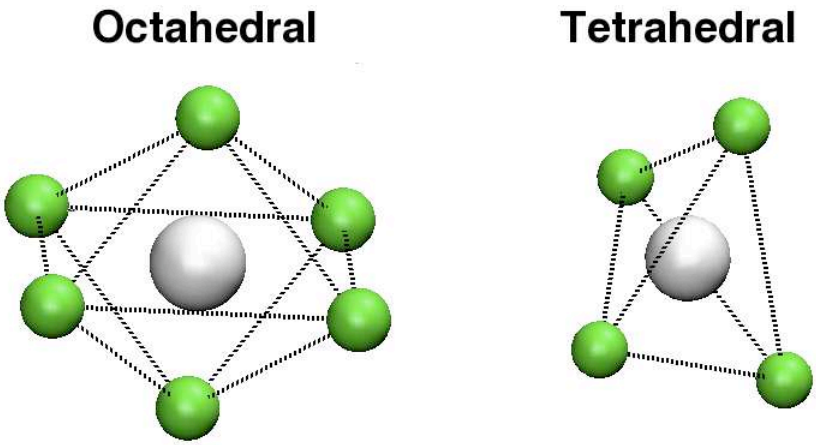

Figure 2.1: A carbon atom (big white ball) in an octahedral or a tetrahedral site, surrounded by iron atoms (small green balls).

consisted of coupling molecular statics and atomistic kinetic Monte Carlo simulations, which allows to simulate thousands of trajectories with duration of up to a few hours at temperatures close to the room temperature. The model and its results are described in the next pages.

2.2 A note on the diffusion mechanism of carbon in bcc iron

Carbon is much lighter than iron and thus a carbon atom in solution in the iron matrix will be generally found in interstitial positions. There are two in the α-Fe lattice, which are depicted in Fig. 2.1. In the octahedral (O) site, a carbon atom is in the center of the octahedron formed by six iron atoms that occupy the vertices. The first nearest neighbors (two atoms) and the second nearest neighbors (four atoms) are situated at a distance of 0.179 nm and 0.198 nm, respectively, from the carbon atom[2]. In the tetrahedral (T) site, a carbon atom is surrounded by four iron atoms at a distance of 0.179 nm.

The interpretation of experimental results [Porter 1981], later supported by *ab initio* calculations [Jiang 2003, Domain 2004], states that the diffusion mechanism of interstitial carbon in bcc iron consists of hops from/to octahedral sites passing through tetrahedral sites. When sitting on an octahedral site, a carbon atom is in the center of one of the faces of a bcc cubic cell. It can jump to one out of four coplanar neighboring octahedral sites located in the edges of the cube.

[2]According to the interatomic potential presented in Ref. [Becquart 2007], after energy minimization.

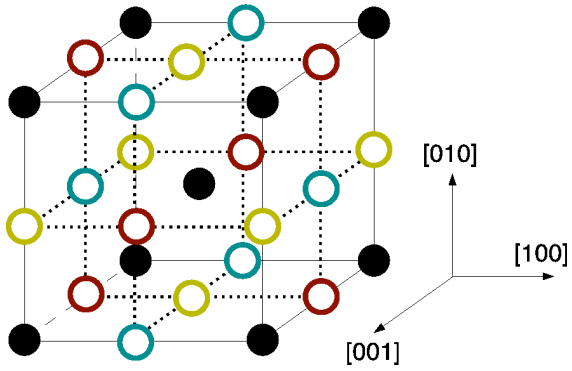

Figure 2.2: A schematic illustration of the positions of the three different octahedral sites (variants) in the bcc unit cell (large open circles). The iron atoms are represented by filled black circles. The dotted lines indicate the minimum energy path for carbon migration.

These sites also correspond to the center of one of the faces of other cubic cells. The basic assumption of the work reported in this chapter and also in Chapter 3 is that this simple diffusion mechanism still holds wherever the iron matrix is moderately strained by the presence of a dislocation. Therefore, the first task before performing simulations was to map all O- and T-sites around a dislocation. For this purpose, we implemented a very simple algorithm taking into account that far enough from the dislocation line, the lattice distortion is small and the bcc symmetry is maintained, so that an octahedral position can be found in the midpoint of every pair of neighboring iron atoms oriented along one of the tetragonal distortion axes ([100], [010], or [001]). As it can be seen in Fig. 2.2, the different orientations of those axes allow us to distinguish three octahedral variants. A tetrahedral position, in turn, is always found in the midpoint of two adjacent octahedral sites. For instance, a carbon atom occupying an [100] O-site can jump either to a [010] or to a [001] O-site (there are two of each). In the first case, the initial and the final O-sites are aligned in the [001] direction, therefore the T-site between them is labeled a [001] T-variant. The same reasoning has been applied to find [100] and [010] tetrahedral variants. Fig. 2.3 shows the T-sites in the bcc unit cell.

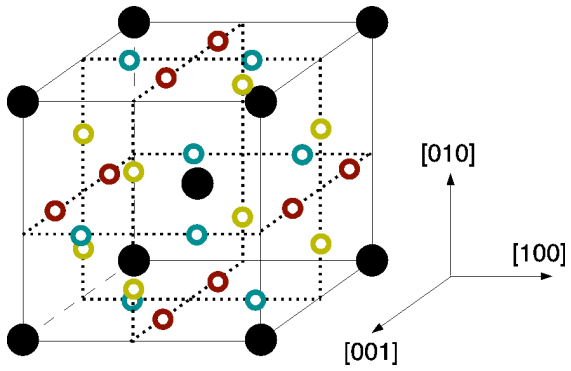

Figure 2.3: A schematic illustration of the positions of the three different tetrahedral sites (variants) in the bcc unit cell (small open circles). The iron atoms are represented by filled black circles. The dotted lines indicate the minimum energy path for carbon migration.

2.3 Energy calculations: molecular statics simulations

2.3.1 Setting up molecular statics simulations

Molecular statics simulations were performed by LAMMPS with a recently developed Fe-C potential [Becquart 2007] built according to the embedded atom method (EAM), taking into account the modifications described in Appendix A. The simulation boxes employed in this study are represented in Fig. 2.4 (top view). They consisted of cylinders of radius 15 nm and height equal to approximately 4 nm with an edge or a screw dislocation in the center. The iron atoms (about 200,000) have been arranged on a bcc lattice with $a_0 = 0.286$ nm, where a_0 is the equilibrium lattice parameter and its value is given by the EAM potential. The dislocations have been introduced in the simulation boxes by displacing the iron atoms according to the anisotropic elasticity theory of straight line defects [Eshelby 1953, Stroh 1962, Stroh 1958]. Such a displacement corresponds to the Volterra elastic field created by the dislocation. In both cases, the Burgers vector is $\vec{b} = a_0/2[111]$ and the glide plane is a $\{\overline{1}01\}$ plane that divides the simulation boxes into two halves. These dislocations are the most commonly observed in α-iron. For the edge dislocation, the dislocation line is oriented along the $[1\overline{2}1]$ direction, whereas the dislocation line for the screw dislocation is oriented along the [111] direction.

This choice of simulation box geometry is not usual in computer simulations, but a dislocation is known to destroy the periodicity of the lattice in directions perpendicular to its line. Consequently, periodic boundary conditions have not

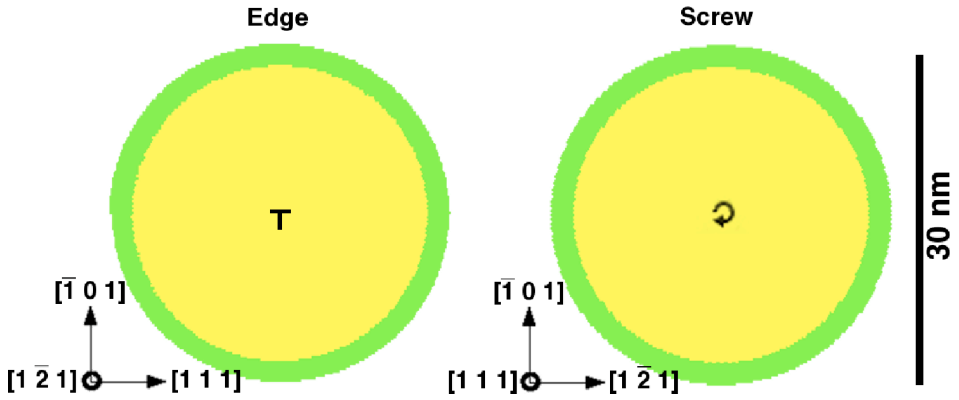

Figure 2.4: Top view of the cylindrical simulation boxes containing an edge and a screw dislocation (in the center). Iron atoms in the outer green rings (2 nm thick) are kept fixed in order to permanently represent the correct displacement field created by the dislocations.

been applied in any direction except along the dislocation line, which corresponds to the cylinder axis. A 2 nm thick (about four times the potential cutoff) outer shell of iron atoms (represented by the green rings in Fig 2.4) was kept fixed in the simulations. The aim of this rigid boundary condition was to avoid spurious relaxation that might come from free surface effects, so that the true dislocation strain fields were permanently reproduced in the far-field. An alternative approach that ensures full periodic boundary conditions introduces a second dislocation, with an opposite Burgers vector, in the simulation box, such that the resulting Burgers vector is zero. This dislocation dipole arrangement has been used, for instance, to compute the core energies and properties of a screw dislocation in α-iron with *ab initio* calculations [Clouet 2009]. However, regarding our work, it would require a much larger simulation box in order to minimize the interaction between the two dislocations and between the second dislocation and the interstitial atom. Osetsky and Bacon, in turn, have proposed the periodic array of dislocations (PAD) method to enforce periodic boundary conditions in the glide direction [Osetsky 2003], which makes it possible to investigate dislocation gliding under the application of shear stress with molecular dynamics or molecular statics. This can be modeled, for instance, by displacing atoms in the free surfaces at the top and at the bottom of the simulation box in opposite directions. In order to implement the PAD method, the simulation box is slightly deformed in order to acquire a rectangular shape (see Fig. 2.5). If the simulation box is large enough, such an unbending procedure has no noticeable effect on the geometry of the dislocation core. The PAD method may be used in a subsequent stage of the current work, when we will investigate the effect of Cottrell clouds

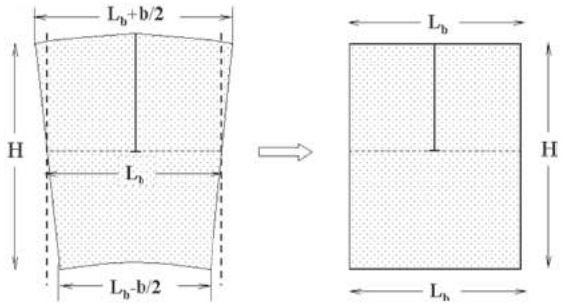

Figure 2.5: A simulation box containing an edge dislocation before and after unbending the crystal in order to enforce periodic boundary conditions along the glide direction (adapted from Fig. 2 in Ref. [Osetsky 2003]).

on dislocation glide. For the moment, the cylindrical approach that we have adopted, despite its lack of boundary conditions in two dimensions, is much easier to implement and provides an accurate description of the interaction between the point defect and the sink in the center, provided that the point defect is far from the rigid outer boundary.

In the simulation boxes defined above, all O- and T-sites within a cylindrical volume of radius 6 nm around the dislocation line, excluded the core region, have been mapped. Therefore, there was at least a distance of 7 nm separating the interstitial positions at the largest distance from the central sink and the rigid layer represented in Fig. 2.4. A parenthesis is necessary here: in this chapter and also in Chapter 3, the region corresponding to the dislocation core has been defined *ad hoc* for both dislocation types as a cylinder of radius $4b \approx 1$ nm that surrounds the dislocation line. This inner cylinder is just wide enough to encompass the very distorted zone in the vicinity of the dislocations. Carbon behavior inside this core region is the subject of Chapter 4.

Before introducing an interstitial carbon atom, the simulation box was relaxed by molecular statics. The dislocation core remained straight for both dislocation types (that is, it did not exhibit any kink), staying in the center of the simulation box. After relaxation, except in the vicinity of the dislocation core, the atomic coordinates did not differ more than a few thousandths of nanometer from the initial coordinates provided by anisotropic elasticity theory, confirming again the ability of this theory to predict atomic positions wherever lattice strain is moderate. Then, for every mapped interstitial position, a molecular statics simulation was launched with a single carbon atom at that position (see Fig. 2.6). For the octahedral sites, full energy minimization was carried out. For the tetrahedral sites, the carbon atom was constrained to relax only on the plane perpendicular

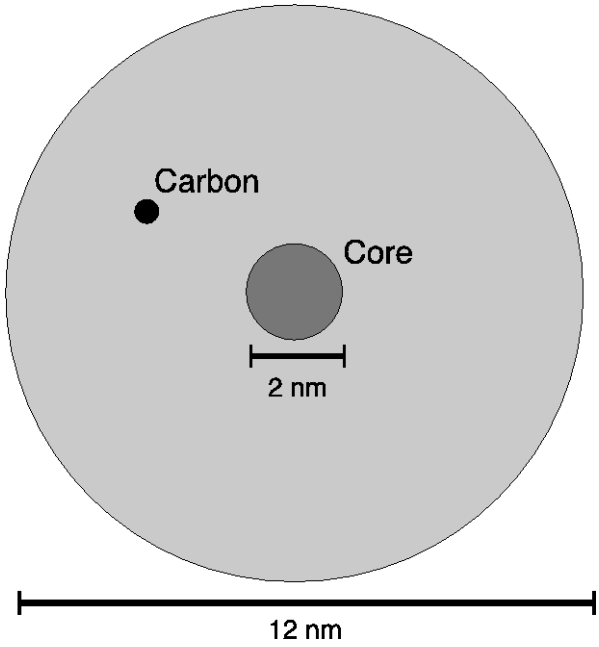

Figure 2.6: Representation of a simulation box containing a carbon atom (small black disk) occupying an interstitial position in the volume of interest, represented by the light gray disk. Interstitial positions in the region defined as the dislocation core, represented by the dark gray disk (diameter equal to $8b \approx 2$ nm), were not included in the mapping of interstitial sites and thus they were not considered in the molecular statics simulations presented in this chapter.

to the vector connecting the two neighboring octahedral sites. About 100,000 carbon-dislocation configurations were relaxed by the conjugate gradient algorithm up to the interatomic forces were less than 10^{-2} eV/nm, which yields a convergence in the total energies between 1–2 meV. A convergence in the order of 0.1 meV (about one order of magnitude smaller) increases the CPU time by a factor of two or even more. Given the large amount of configurations, a compromise between the accuracy and the CPU time was necessary.

2.3.2 Validation of the diffusion mechanism in the presence of dislocations

In order to gain some confidence on the validity of the simple carbon diffusion mechanism described previously in a context where the carbon atom interacts with a dislocation, some minimum energy path calculations with the CI-NEB method [Henkelman 2000b, Henkelman 2000a], as implemented in LAMMPS, have been performed for transitions in the vicinity of either an edge or a screw dislocation. In every CI-NEB simulation, nine images were used. Adjacent images were connected by a spring with a spring constant k of 10 eV/nm. The total

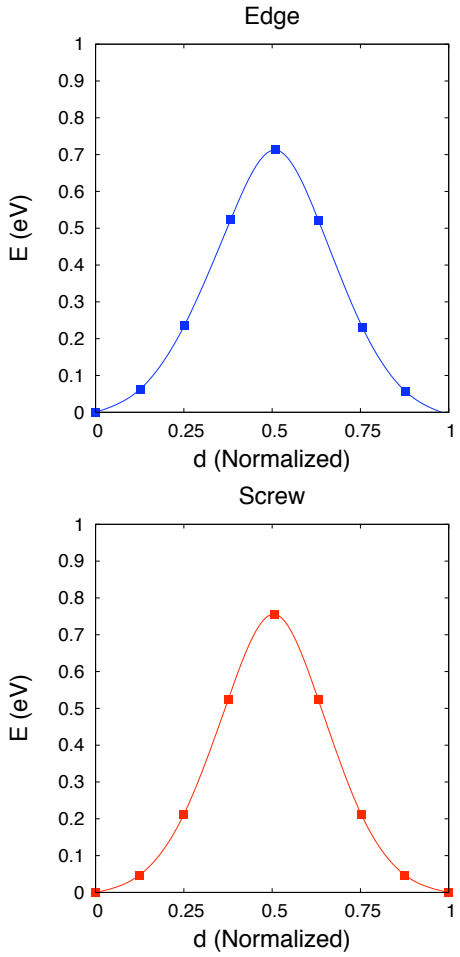

Figure 2.7: NEB-calculated minimum energy paths for a carbon atom migrating between interstitial sites in the vicinity of an edge or a screw dislocation. They refer to transitions between local energy minima found just above the dislocation cores ($x \approx 0$, $y \approx 0.6 - 0.7$ nm, with respect to the dislocation lines). In this plot, d is the normalized distance between the two extremities of each path. The saddle points are found in the middle of the path.

energy of each image was minimized by damped dynamics up to the internal and also the inter-image forces, taken together, were less than 10^{-2} eV/nm. These simulations have shown that taking the octahedral sites as the energy minima and the tetrahedral site as the saddle points for carbon migration seems to be a good approximation even relatively near the dislocation lines (see Fig. 2.7).

2.3.3 Carbon-dislocation binding energies

The strength and the type of interaction (attractive or repulsive) between a carbon atom and a dislocation as a function of the relative positions of the defects

is given by the corresponding binding energy, defined as follows:

$$E^b_{[O|T]} = E_{[O|T],carbon} + E_{dislo} - E_{[O|T],carbon+dislo} \tag{2.5}$$

In Eq. (2.5), $E_{O,carbon} = -10.059$ eV and $E_{T,carbon} = -9.243$ eV are the energies added by an isolated carbon atom occupying either an O- or a T-site in α-iron after relaxation, according to the Fe-C potential. They can be easily obtained by taking the difference between the total potential energies of a large simulation box with a carbon atom occupying either an O- or T-site and the same simulation box with no carbon. E_{dislo}, in turn, is the total potential energy of one of the simulation boxes depicted in Fig. 2.4. $E_{[O|T]carbon+dislo}$ refers to the total potential energy of the same simulation box with a single carbon atom in an O- or a T-site. $E^b_{[O|T]} > 0$ reveals an attractive interaction between the point and the line defects, whereas $E^b_{[O|T]} < 0$ means that the dislocation repels the carbon atom. The mapping of carbon-dislocation binding energies for a carbon atom occupying O- and T-sites near an edge and a screw dislocation is shown in Figs. 2.8 and 2.9, respectively. In a non-strained iron crystal, all O-sites are energetically equivalent (as well as the T-sites), but this equivalence is lost even at low strain level, as reported by Garruchet and Perez for uniaxial strain [Garruchet 2008]. This is underscored in the neighborhood of a dislocation. The (absolute) binding energies $|E^b_{[O|T]}|$ decrease proportionally to $1/R$, where R is the separation between the defects. One can also see that there is an important angular dependence on the values of $E^b_{[O|T]}$, reflecting the non-homogeneity of the dislocation stress field and confirming what pioneering models predicted a long time ago [Cottrell 1949, Cochardt 1955]. Out of the region defined as the dislocation core, the maximum $|E^b_{[O|T]}|$ is smaller than 200 meV for both dislocation types and, for $R > 5$ nm, $|E^b_{[O|T]}|$ falls below 50 meV.

Around an edge dislocation, both E^b_O and E^b_T are affected by the normal stresses σ_{xx} and σ_{yy} created by the line defect, since it is related to the volume of the locus occupied by the carbon atom in the iron lattice. In the zone under tension (above the glide plane), the volume of the interstitial site is larger than in the zone under compression (below the glide plane), which implies that the lattice relaxes less in the first case in order to accommodate a carbon atom. Owing to the misfit of the planes just above and below the glide plane, the edge dislocation is also seen to create a shear stress σ_{xy}. Lattice relaxation due to the carbon atom leads to local tetragonal distortion, and it is much more important when a carbon atom sits on an octahedral site than in a tetrahedral one, according to the current EAM potential.Therefore, the shear stress of the edge dislocation has

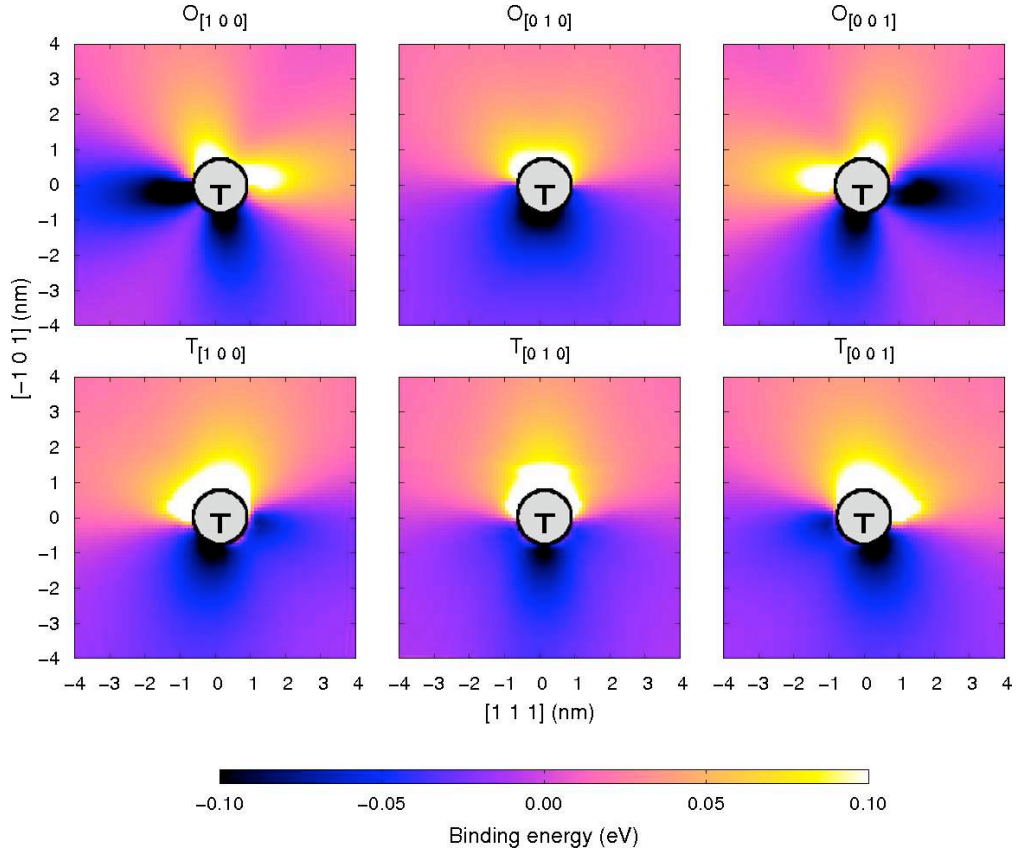

Figure 2.8: Mapping of carbon-dislocation binding energies obtained by atomistic simulations for carbon positions around a straight edge dislocation (in the center) which is aligned parallel to the $[1\bar{2}1]$ direction (perpendicular to the page). The gray circle in the center (diameter equals to $8b$) refers to the region defined as the dislocation core.

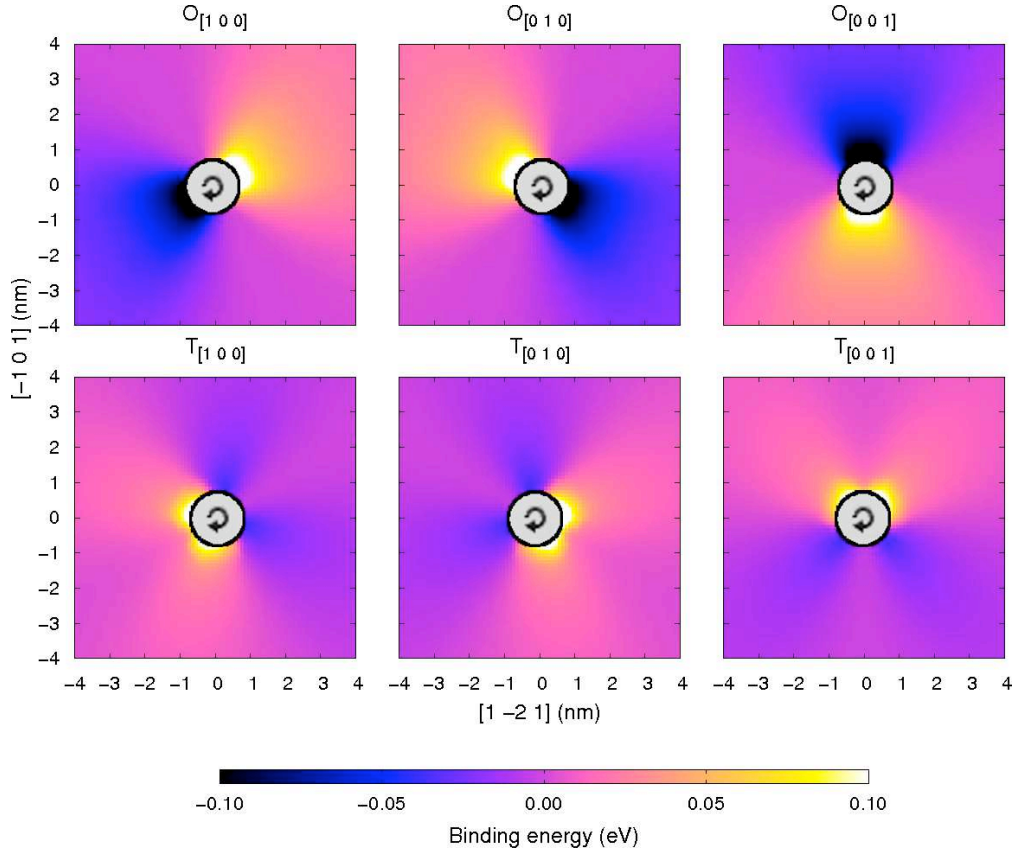

Figure 2.9: Mapping of carbon-dislocation binding energies obtained by atomistic simulations for carbon positions around a straight screw dislocation (in the center) which is aligned parallel to the [111] direction (perpendicular to the page). The gray circle in the center (diameter equals to $8b$) refers to the region defined as the dislocation core.

a minor influence on a carbon atom occupying a T-site near the glide plane, thus in this case E_T^b is not as significant as E_O^b. For the [100] and [001] O-site variants, in the simulation box orientation that we have adopted, the carbon atom induces a local shear of the two adjacent $(\overline{1}01)$ planes, i.e., we have a local $\sigma_{xy} \neq 0$ which interacts with the long range σ_{xy} created by the edge dislocation. A carbon atom in a [010] O-site in turn induces a local σ_{xz} shear. Since outside the core the σ_{xz} component of the stress tensor of the edge dislocation vanishes, there is little interaction between both defects when a carbon atom lies on a [010] O-site near the glide plane and $E_O^b \to 0$.

As it has been observed in Ref. [Clouet 2008], when the carbon atom approaches an edge dislocation along its glide plane, the interaction between the point and the line defect becomes so strong that the dislocation line leaves its initial position towards the carbon atom. Fig. 2.10 shows the position of the dislocation line as a carbon atom approaches the line defect coming from $-\infty$. Every position occupied by the carbon atom corresponds to an [001] O-variant. We have seen in Fig. 2.8 that when it is found occupying interstitial sites of this variant near the glide plane and the carbon position $X_C < 0$, the carbon atom is attracted by the dislocation. At a separation distance of approximately $3.5b$, the edge dislocation is displaced along its glide plane by about 0.6 nm. Such a displacement is clearly associated with a discontinuity in the carbon-dislocation binding energy. This abrupt jump in E^b has been already reported in Ref. [Hanlumyuang 2010], although the reason has not been explained by the authors.

In contrast with the edge dislocation, the stress field of a screw dislocation is predominantly shear (σ_{xz} and σ_{yz}) with small normal contribution restricted to the close vicinity of the core. Considering that the interaction of a carbon atom with a dislocation through their respective shear stress is much stronger when a carbon atom lies in an O-site than in a T-site, as already stated above, E_O^b is usually much more important than E_T^b in the vicinity of a screw dislocation. Moreover, due to its high Peierls stress, the screw dislocation does not leave its initial position as a carbon atom approaches the line defect.

2.3.4 Energy barriers for carbon diffusion

After obtaining the total energies of all carbon-dislocation configurations inside the volume of interest with molecular statics, it was straightforward to calculate the energy barriers for all transitions with Eq. (1.4).

Fig. 2.11 depicts a mapping of the energy barriers in the neighborhood of an edge dislocation, for the six types of transitions that a carbon atom can undergo.

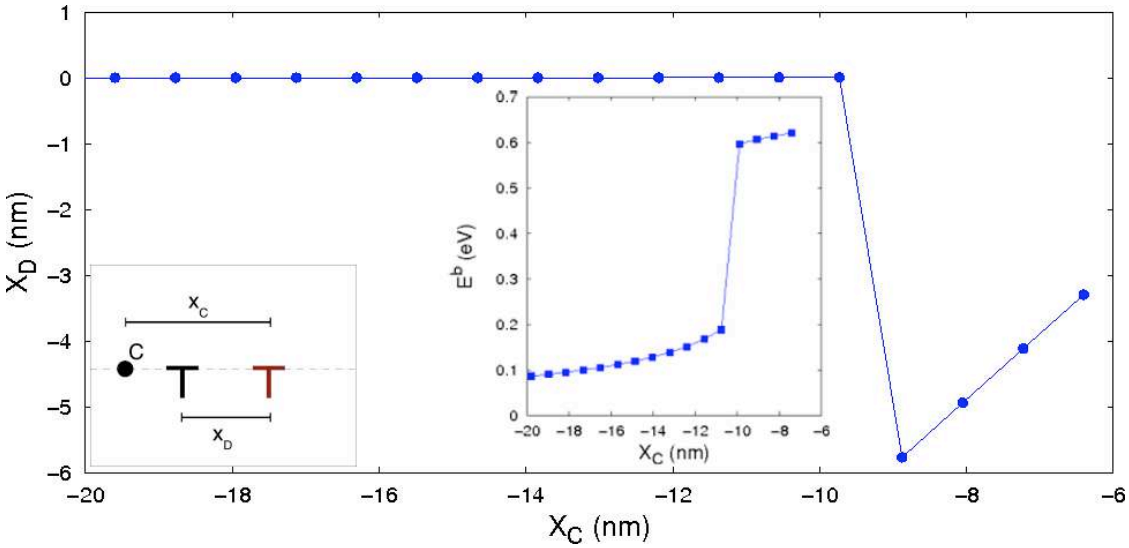

Figure 2.10: Dislocation line position (X_D) as a function of carbon position (X_C) for a carbon atom occupying interstitial sites corresponding to the [001] O-variant along the glide plane of an edge dislocation. The reference is the initial position of the dislocation line (in red in the left inset). The carbon-dislocation binding energy E^b as a function of carbon position is shown in the inset in the middle.

The first thing to be noticed is that the effect of the edge dislocation on the energy barriers is more pronounced running parallel to the glide plane. Indeed, the largest variations in the migration energies (ranging from 0.66 eV up to 0.98 eV) occur when a carbon atom jumps between [100] and [001] O-sites near the glide plane. A carbon atom undergoing such transitions move on the $(\bar{1}01)$ plane passing through a [010] T-site. The carbon atom sitting on one of these variants has been seen in Fig. 2.8 to strongly interact with the σ_{xy} component of the dislocation stress tensor that predominates thereby. On the other hand, the little interaction with the dislocation explains the fact that energy barriers for transitions starting from a [010] O-site in the vicinity of the glide plane differ less from the bulk value (0.816 eV) than their counterparts. Although less pronounced, there also are important variations in the migration energies just above and below the dislocation core, where the point and the line defects interact more due to their corresponding normal stresses.

For the screw dislocation, one can see in Fig. 2.12 that the variation of the energy barriers for a given transition is mirrored by the variation of the energy barriers of the inverse transition. This draws an overall picture of the energy barriers for carbon migration around a screw dislocation that is much simpler than what is seen for an edge dislocation. Outside the core of the screw dislocation, the lowest energy barrier is 0.65 eV and the highest one is 0.89 eV.

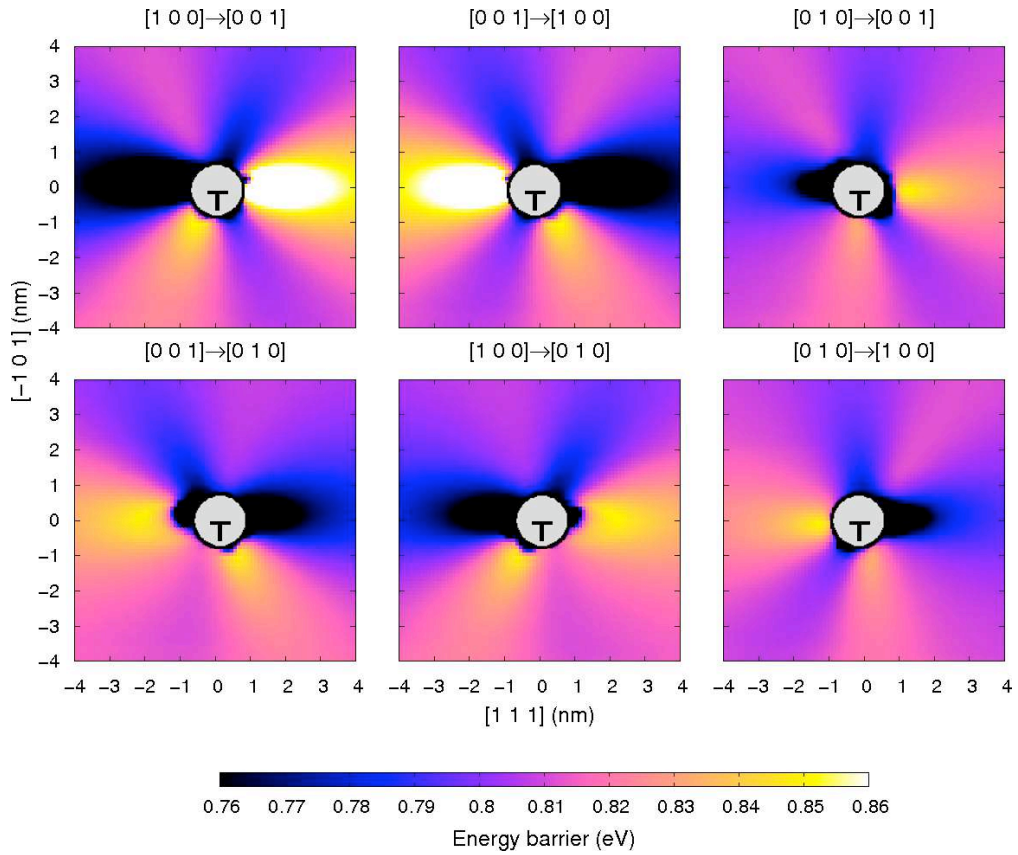

Figure 2.11: Mapping of energy barriers obtained by atomistic simulations for carbon migration in the vicinity of a straight edge dislocation (in the center) which is aligned parallel to the $[1\bar{2}1]$ direction (perpendicular to the page). The gray circle in the center (diameter equals to $8b$) refers to the region defined as the dislocation core.

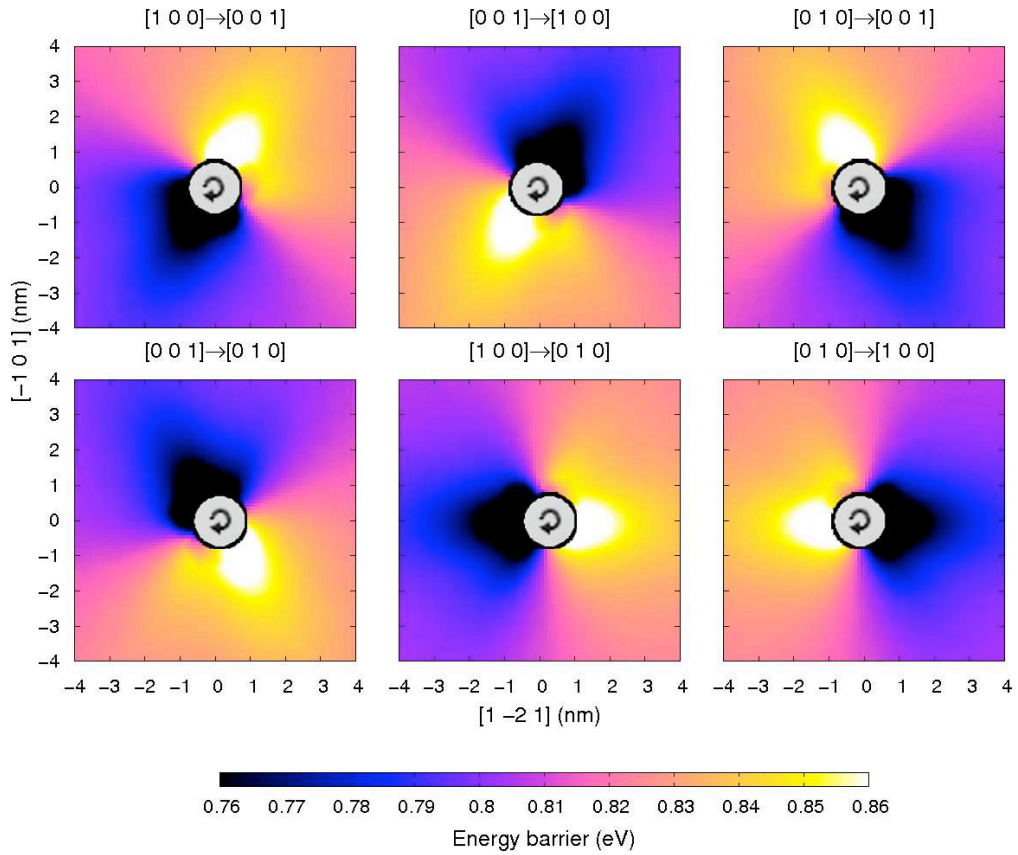

Figure 2.12: Mapping of energy barriers obtained by atomistic simulations for carbon migration in the vicinity of a straight screw dislocation (in the center) which is aligned parallel to the [111] direction (perpendicular to the page). The gray circle in the center (diameter equals to $8b$) refers to the region defined as the dislocation core.

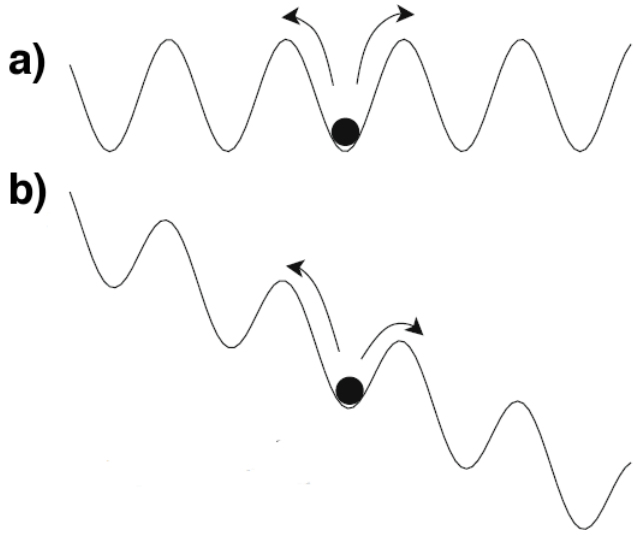

Figure 2.13: A random walker sitting in a local minimum (adapted from Fig. 1 in Ref. [Barlett 2009]). In this 1D random walk, the random walker can perform one of two jumps at a time, either to the left or to the right: in a simple random walk (a), energy barriers are the same and the probability is of 50% per jump; in a biased random walk (b), the random walker is likely to jump to the right, because the energy barriers are lower in this direction.

2.4 Dislocation-induced bias on carbon diffusion

In a simple on-lattice random walk, at every lattice site, the random walker can take one of the N allowed steps with a probability of $1/N$. The random walker trajectory spreads isotropically and, after a large number of steps, the volume visited by the random walker will assume an almost spherical shape. A different situation appears if one step has a lower barrier compared to the other ones. Since a lower energy barrier increases the probability to take that step, now the random walker prefers to take it rather than others. Such a random walker performs, in this case, a biased random walk [Rudnick 2004, Barlett 2009, Codling 2008], which has as a net effect a drift in the trajectory. In Fig. 2.13, the sketch of a 1D random walk is depicted to clarify the concept. In this figure, a random walker is found sitting in a local energy minimum and can take a fixed length step either to the left or to the right in order to fall into one of the two adjacent potential wells. When performing a simple random walk (Fig. 2.13 (a)), the random walker will choose between the adjacent steps with a probability of 50% per step. On the other hand, if the random walk is biased somehow (Fig. 2.13 (b)), the random walker now will take steps preferentially to the right.

Biased random walks are widely used, for instance, in computational biol-

ogy to model organism motility [Codling 2008]. In a phenomenon known as chemotaxis, a bacterium propels itself with the aid of its flagella following what resembles a random walk. However, the changes in the direction of a bacterium are dictated by the chemical environment: the organism tends to move towards directions with increasing food supply gradients and also to avoid directions with increasing toxin gradients [Macnab 1972]. These different gradients are said to add a bias to the bacterium motion. Concerning materials science, solid state diffusion is usually biased owing to the interaction of the diffusing particle with some applied field (e.g., an external electric field adds a bias to the diffusion of a charged particle).

A carbon atom jumping from/to octahedral sites in a non-strained bcc iron lattice is an example of a simple random walker. In this case, the probability that a carbon atom will perform a jump to a specific octahedral site is 25% and the step length also is the same for all possible jumps ($\delta = a_0/2$). On the other hand, if the lattice is non-homogeneously strained, as is the case when a dislocation is present, the energy of the different O- and T-sites change and, as a consequence, the relative heights of the energy barriers (and thus, the transition probabilities) change as well, as one can readily deduce from Figs. 2.11 and 2.12. The biasing field is the long-range stress field of the dislocation and the diffusion of a carbon atom immersed in it should be therefore better described as a biased random walk.

The strength and the orientation of the bias added to a random walk are quantified by the mean displacement vector $\langle\vec{d}\rangle$, defined as follows:

$$\langle\vec{d}\rangle = \sum_{j=1}^{N} P_{i\to j}\vec{\delta}_{i\to j} \tag{2.6}$$

where $P_{i\to j}$ is the normalized temperature-dependent probability of the transition $i \to j$, $\vec{\delta}_{i\to j}$ is the vector that connects the site i to the site j, and N is the number of first nearest neighbors of site i (since a carbon atom occupying an octahedral site in α-Fe can jump to four other neighboring octahedral sites, $N = 4$). If there is no bias, $\langle\vec{d}\rangle = \vec{0}$ everywhere (and we have a simple random walk). On the other hand, if the bias is too strong, the walk cannot be said to be random anymore because the walker deterministically follows one direction.

Figs. 2.14 and 2.15 show the projection of the vectors $\langle\vec{d}\rangle$, for $T = 300$ K and $T = 600$ K, on the planes perpendicular to the dislocation lines for the edge and screw dislocations, respectively. In these figures, each arrow corresponds in fact to the resulting mean displacement vector in an area of 0.4×0.4 nm^2.

Only vectors with lengths greater than 10^{-3} nm are plotted. The first thing to be noticed is that the bias on carbon diffusion is much more important around an edge dislocation than around a screw dislocation. This is to say that, at the same temperature, an edge dislocation influences a diffusing carbon atom at a larger distance. Moreover, as expected, such a bias is drastically reduced as the temperature increases. In the high temperature limit, the dislocation stress field should have a slight effect on carbon diffusion, if any, and the carbon atom would behave almost as a simple random walker.

More interestingly, the dislocation-induced bias does not differ from one dislocation type to the other only in its extent: one can see that both its strength and its orientation are location dependent. This is obviously a consequence of the fact that the dislocation stress field varies spatially, establishing a clear contrast with the bias induced by an uniform external field, as the one reproduced in Fig. 2.13. Regarding the bias strength, it increases as the carbon atom approaches the dislocation core, as one should expect. In Fig. 2.14, it is straightforward to see that the bias on carbon diffusion is not the same above and below the glide plane of an edge dislocation. When diffusing in the tensile region, a carbon atom is pulled towards the dislocation core. A quite different picture is shown in the compressive region: a carbon atom thereby is clearly discouraged to reach the dislocation core from below, it rather prefers to diffuse towards the glide plane. As one can see in Fig. 2.15, the bias induced by a screw dislocation, in turn, also exhibits the well-known three-fold symmetry of its stress field: attractive and repulsive regions around the dislocation line are separated by 120°.

The bias on carbon diffusion due to the dislocation stress fields should play the major role in driving the nucleation of a Cottrell atmosphere in the initial stage of static strain aging, when carbon concentration is low and carbon-carbon interactions are negligible.

2.5 Carbon diffusion to dislocations: AKMC simulations

2.5.1 Setting up AKMC simulations

The AKMC simulation box consisted of a rigid lattice where every site corresponded to an O-site in the simulation box employed in molecular statics simulations, thus it was also a cylinder of radius 6 nm. Two absorbing barriers (i.e., end points for the AKMC simulations) were present: the so-called core region

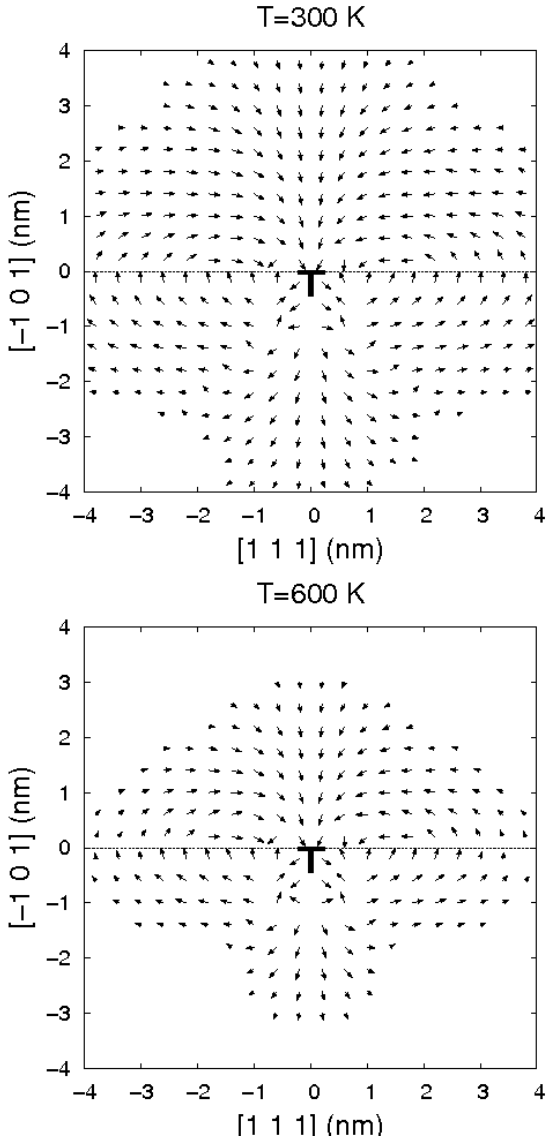

Figure 2.14: Mean displacement vectors $\langle \vec{d} \rangle$ in the vicinity of an edge dislocation at $T = 300$ and $T = 600$ K. Only vectors with lengths greater than 10^{-3} nm are plotted. For the sake of readability the vectors were multiplied by 100. The z component (parallel to the dislocation line) is not shown. Each arrow corresponds to a vector which is in fact the resulting vector in an area of 0.4×0.4 nm^2. The dotted line represents the glide plane.

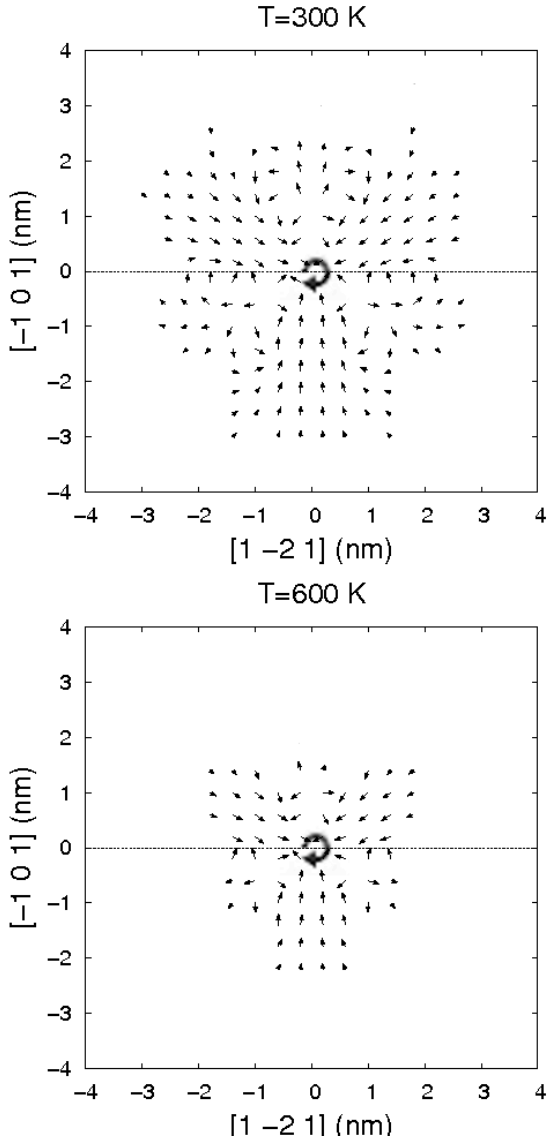

Figure 2.15: Mean displacement vectors $\langle \vec{d} \rangle$ in the vicinity of a screw dislocation at $T = 300$ and $T = 600$ K. Only vectors with lengths greater than 10^{-3} nm are plotted. For the sake of readability the vectors were multiplied by 100. The z component (parallel to the dislocation line) is not shown. Each arrow corresponds to a vector which is in fact the resulting vector in an area of 0.4×0.4 nm^2. The dotted line represents the glide plane.

($R < 4b \approx 1$ nm) and the outer boundary ($R > 6$ nm). In the first case, a carbon atom is considered trapped by the dislocation; in the other case, the carbon trajectory simply is not followed anymore. Each set of AKMC simulations generated 100,000 carbon trajectories with a minimum of 100 and a maximum of 100,000 jumps at temperatures ranging from $T = 300$ K to $T = 600$ K. This minimum number of jumps was chosen in order to prevent including in the statistics trajectories that either fall into the dislocation core or leave the simulation box through the outer boundary too quickly. Starting points have been chosen at random and thus equally distributed inside the simulation box, so that the resulting trajectories have covered its whole volume and explored as many pathways as possible. Additionally, AKMC simulations were also performed where the energy barriers were considered as 0.816 eV (i.e., the energy barrier for carbon diffusion in non-strained bulk α-iron) everywhere. Comparison with the results of these simple (isotropic) random walks allows to check the effect of the dislocation stress fields on carbon diffusion.

2.5.2 Analysis of carbon trajectories

Because of the the boundary conditions, the kinetics given by the AKMC simulations is in fact a competition between the two absorbing barriers. Therefore, it is worth considering in separate trajectories that left the simulation box and trajectories that terminated in the dislocation cores (which are the ones that we are more interested in). Indeed, the unphysical sink at $R > 6$ nm does not have any active influence on carbon trajectories: since it does not create any stress in the lattice, a carbon atom does not "see" the outer boundary at any moment except just before reaching it, if it does. On the other hand, it becomes more likely that a carbon trajectory will leave the simulation box rather than being trapped by the dislocation as the trajectories start farther from the dislocation line. Care should be taken because this changes the rate of depletion of carbon atoms in solid solution due to dislocation trapping in the latest stages of the simulated kinetics, inducing a pseudo-saturation not related at all to the physical saturation of dislocations observed in experiments.

Figs. 2.16 and 2.17 show the evolution of the fraction of carbon atoms trapped by either an edge or screw dislocation, respectively, in the course of AKMC simulations. Regarding the edge dislocation, a first noticeable effect is that the kinetics is accelerated with respect to the simple random walk case. Such an effect is obviously temperature-dependent, but it still is present at the highest temperature (600 K) considered in this study. It is also consistent with the

carbon atom diffusing most of the time (about 80% of the total number of jumps, at $T = 300$ K) above the glide plane, where the normal tensile stress due to the edge dislocation lowers the activation energies with respect to the non-strained bulk value, as can be seen in Fig. 2.11, which speeds up diffusion. For the screw dislocation, the effect is the opposite: there is a delay in the beginning of the stress-assisted kinetics with respect to the simple random walk one, clearly observed at $T = 300$ K. Such a delay almost disappears at $T = 600$ K. Therefore, diffusion of a carbon atom in the vicinity of a screw dislocation, at least at low temperatures, is slowed down owing to the interaction of the impurity with the dislocation stress field.

Compared to the simple random walk simulations, in which 27% of the carbon trajectories fall into the central trap purely by chance, the fraction of carbon trajectories ending either in the edge or in the screw dislocation core rather than leaving the simulation box ranges between 32–34% and between 30–32%, respectively. In other words, both the edge and the screw dislocations have the ability to drag solute carbon atoms found diffusing nearby, although such a net attractive character, for both dislocation types, seems to be too slight at a first sight. This is somewhat true for the screw dislocation, but it does not apply at all to the edge dislocation. As illustrated in Fig. 2.14, the carbon atom feels differently the influence of an edge dislocation above and below the glide plane, even relatively far from the dislocation line. Consequently, as one can see in Fig. 2.18, the probability that a simulated carbon trajectory will end in the core region of an edge dislocation strongly depends on where it starts. Between 40% and 50% of the trajectories starting in the zone under tension have been trapped by the edge dislocation. On the other hand, the trapping probability drops below 20% for trajectories starting in the zone under compression. Concerning the trajectory end point, irrespective of temperature, between 77–85% of the carbon trajectories have reached the dislocation core from the tensile half of the simulation box (above the glide plane), which implies that most of the trajectories starting in the compressive half and terminating in the core have crossed first the glide plane.

2.5.3 Application of an analytical kinetic model to simulation results

Direct comparison of the kinetics simulated by AKMC with aging experiments is challenging. Ideally, one should be able to reproduce the evolution of the properties of a realistic system in simulations. However, in practice, the actual microstructure of most of the materials comprises multiple defects (e.g., vacancies,

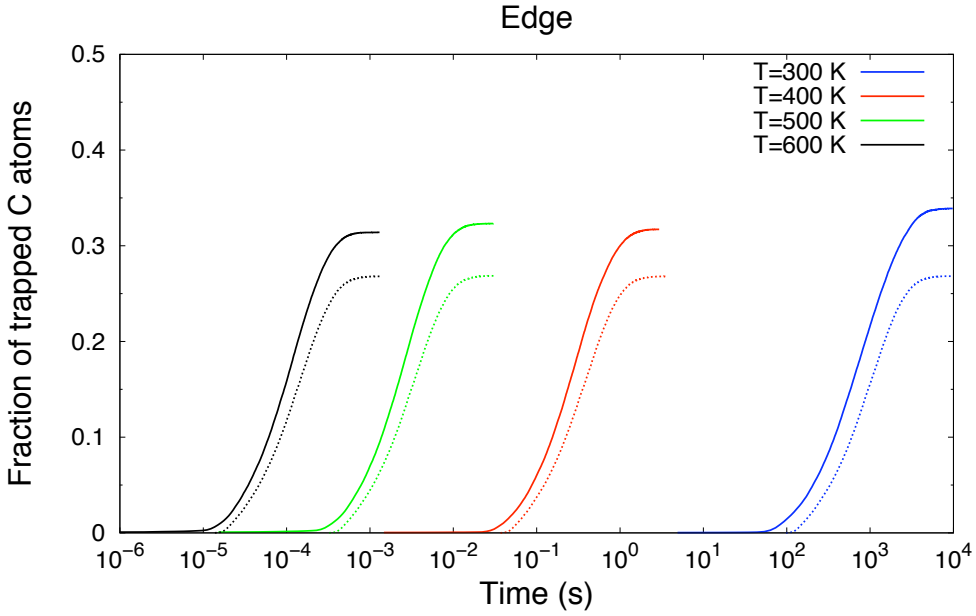

Figure 2.16: Solid lines represent the fraction of carbon trajectories that terminated in the region defined as the core of an edge dislocation ($R < 4b \approx 1$ nm) during AKMC simulations as a function of time for temperatures ranging from 300 K to 600 K. Dotted lines, in turn, represent the results of simple random walks ($\Delta E^m = 0.816$ eV).

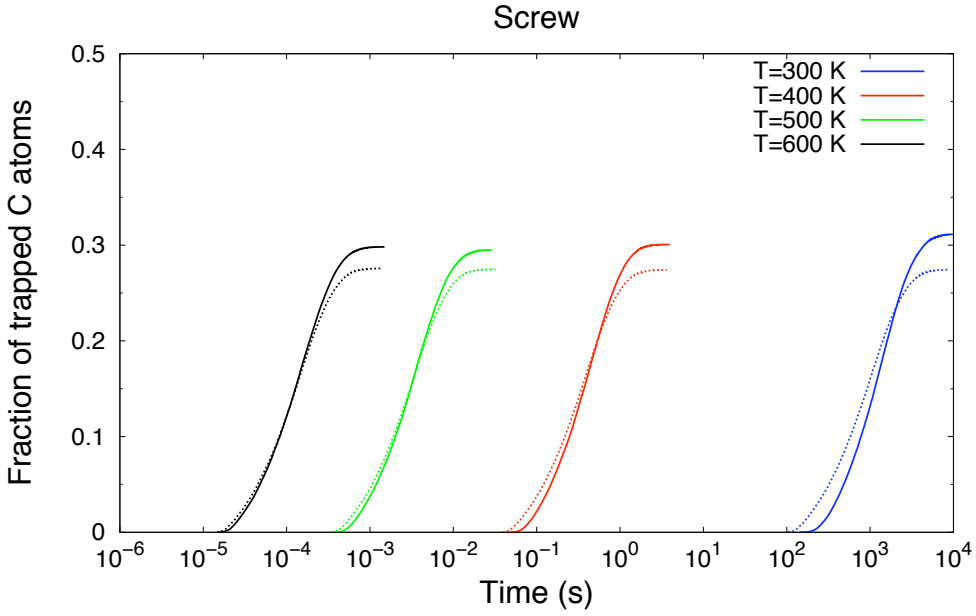

Figure 2.17: Solid lines represent the fraction of carbon trajectories that terminated in the region defined as the core of a screw dislocation ($R < 4b \approx 1$ nm) during AKMC simulations as a function of time for temperatures ranging from 300 K to 600 K. Dotted lines, in turn, represent the results of simple random walks ($\Delta E^m = 0.816$ eV).

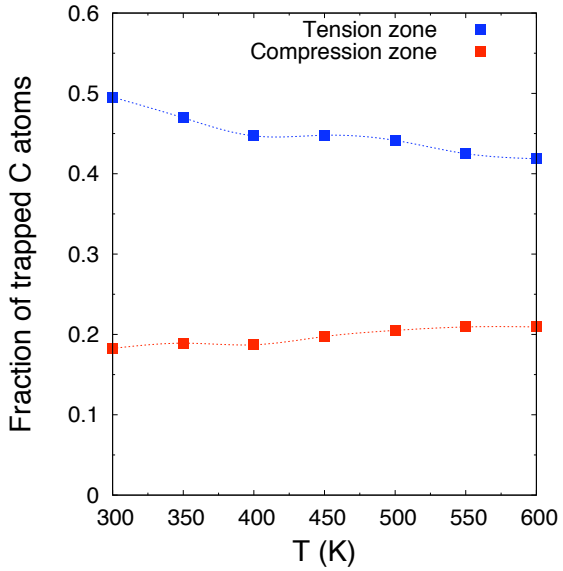

Figure 2.18: Fraction of carbon trajectories, starting either in the zone under tension or in the zone under compression near an edge dislocation, that terminated in the dislocation core in AKMC simulations.

voids, dislocations, precipitates, grain boundaries) that affect in different manners the aging process. This implies a level of complexity that puts realistic systems most of times out of reach of atomistic simulations. Moreover, the scales involved in aging experiments and simulations are not the same.

Despite the difficulties outlined above, a bridge between aging experiments and atomic scale simulations may be established through simple analytical kinetic models commonly used to interpret experimental results, such as aforementioned Hartley's model. For instance, results reported by A. K. De and co-workers fitted to Eq. (2.4) show that the kinetics of strain aging in prestrained ULC bake hardening steels apparently, at small t, obey the so-called $t^{\frac{2}{3}}$ kinetic law [De 2001, De 2000]. The effective activation energies for carbon segregation in the studied specimens lie between 0.82–0.85 eV. According to their interpretation of the application of Hartley's model to the experimental data, dislocation densities up to a level of 10% prestrain have no important effect on the kinetics of strain aging at low temperatures (320–410 K).

In the following analysis, we assumed that each dislocation-trapped trajectory refers to the diffusion of a single carbon atom to a dislocation and that the ensemble of many simulations provides a picture of carbon segregation to the line defects. This implies a low carbon concentration, so that every carbon trajectory is independent from the others and every arriving carbon locks a different segment of an infinitely long dislocation line. Given the relatively small

volume of the simulation box, the carbon atom interacts with the central sink during most of the simulated time. Simulation results shown in Figs. 2.16 and 2.17 were fitted at the best (asymptotic standand error below 1%) by the nonlinear least-squares Marquardt-Levenberg algorithm [Press 2007], as implemented in Gnuplot, to Eq. (2.4), with the fraction of carbon atoms trapped by the dislocation replacing $\Delta\sigma/\Delta\sigma_{max}$. As in the experimental work, only the initial part of the curves fits to Hartley's model.

The kinetic parameters obtained from the simulated data can be seen in Table 2.1. Values of n for both dislocation types are within the experimental range (0.59–0.80) reported in Ref. [De 2001]). Near an edge dislocation, in the "biased walks" (i.e., the AKMC simulations where the effects of the dislocation stress field on the energy barriers are taken into account), n varies very little, remaining close to 0.66 ($\approx 2/3$). A different picture is seen for carbon diffusion to a screw dislocation: n varies from 0.66 ($T = 600$ K) to 0.75 ($T = 300$ K). Knowing that $D = D_0 \exp(-E^m_{eff}/kT)$, where k is the Boltzmann constant and T is temperature, the effective activation energy E^m_{eff} has been obtained from the slope of $\ln(D)$ as a function of $1/T$. Not surprisingly, $E^m_{eff} = 0.817$ eV for the "unbiased walks", a difference of only 1 meV with respect to the energy barrier used for all transitions in these walks. Regarding the stress-assisted walks, the effective activation energy in the paths followed by the carbon atom is slightly lowered in the vicinity of the edge dislocation (0.809 eV) and augmented in the vicinity of a screw one (0.825 eV). In any case, E^m_{eff} falls within the wide range (0.77–0.95 eV) of apparent activation energies obtained in strain aging experiments found in the literature [Elsen 1993, De 2001, De 2000]. Overall, these results indicate that, although some effects of the dislocations on the kinetic parameters are actually observed in AKMC simulations, they seem to be below what can be detected by aging experiments, the results of which present large variations for all kinetic parameters. In addition, it should be pointed out that the AKMC simulations also show that trapping of carbon atoms by the dislocation proceeds according to the same kinetic law as $\Delta\sigma/\Delta\sigma_{max}$ at small t. This underlines the fundamental link between the microscopic phenomenon assessed by the AKMC simulations and the change in mechanical properties observed in the macroscopic experiments.

2.6 Overview

Molecular statics has been employed to obtain the total energies for a carbon atom occupying octahedral and tetrahedral positions within a radius of 6 nm around an

Dislocation	Simulation type	T (K)	n	D (m^2/s)	D_0 (m^2/s)	E^m_{eff}
Edge	Biased walk	300	0.62	4.2×10^{-21}		
		400	0.65	1.0×10^{-17}		
		500	0.66	1.2×10^{-15}		
		600	0.65	2.6×10^{-14}	1.7×10^{-7}	0.809
	Unbiased walk	300	0.65	2.6×10^{-21}		
		400	0.65	7.0×10^{-18}		
		500	0.66	8.1×10^{-16}		
		600	0.66	1.9×10^{-14}	1.4×10^{-7}	0.817
Screw	Biased walk	300	0.75	2.3×10^{-21}		
		400	0.71	7.0×10^{-18}		
		500	0.69	8.6×10^{-16}		
		600	0.66	2.0×10^{-14}	1.7×10^{-7}	0.825
	Unbiased walk	300	0.64	2.6×10^{-21}		
		400	0.65	7.0×10^{-18}		
		500	0.66	8.0×10^{-16}		
		600	0.66	1.9×10^{-14}	1.4×10^{-7}	0.817

Table 2.1: Kinetic parameters obtained from AKMC simulations after fitting to Eq. (2.4). "Biased walk" refers to the AKMC simulations with energy barriers calculated by molecular statics and "Unbiased walk" refers to simple random walks with the same energy barrier (0.816 eV) for all transitions.

edge or a screw dislocation, excluded a cylindrical region of radius $4b$ surrounding the dislocation line, taken as the dislocation core. The energy barriers calculated from molecular statics results have been used to build a static catalog for an AKMC code. AKMC simulations have generated a number of independent carbon trajectories for temperatures in the 300–600 K range. Carbon diffusion is seen to be biased by the stress field of dislocations, with location dependent transition probabilities. Such a bias, as expected, decreases with temperature, and it is stronger when the carbon atom approaches an edge dislocation than a screw dislocation. In the compressive half of an edge dislocation, the carbon atom is repelled by the dislocation core and either it moves in oblique trajectories towards the glide plane or escapes the influence of the edge dislocation, moving away from the sink. In the tensile half, the carbon atom is more likely to diffuse directly towards the dislocation core. The bias on carbon diffusion around a screw dislocation, in turn, reproduces the three-fold symmetry of its stress field, with attractive zones alternating repulsive ones. Both dislocations have been seen to present a net attractive character, dragging a carbon atom diffusing nearby.

2.7 Ongoing work

In order to model the actual kinetics of carbon diffusion to dislocations, the AKMC simulations presented in this chapter have to be improved. The unphysical absorbing barrier at a relatively short distance from the dislocation is certainly undesirable because it has been seen to affect the simulated kinetics. For the time being, there is no straightforward way to solve this problem, but some attempts are under consideration.

A first possibility is to treat the outer boundary as a reflecting barrier, that is, when the carbon atom reaches it, it is sent back to the simulation box instead of being lost. However, although this artifact should not have a great influence on the simulated kinetics in a much larger simulation box, since a carbon atom diffusing near the outer boundary would behave as a simple random walker, it is not sure this would be the case in a simulation box as small as the one that we have employed, where the carbon atom interacts with the dislocation most of the time.

A second and more promising solution is to enforce full periodic boundary conditions by remapping, by the criterion of proximity, the sites in the cylindrical simulation box into a non-strained rectangular one, assigning the carbon migration energy in non-strained bcc iron (0.816 eV) to the remaining sites in

the latter. This implies, particularly in the case of an edge dislocation, an abrupt interacting-to-noninteracting change regarding the point and the line defects, which may also affect the simulated kinetics. A possible way to improve this approach is to employ fast elasticity calculations to obtain energy barriers for carbon diffusion in the far-field. The applicability of elasticity calculations for this purpose is discussed in Chapter 3.

Chapter 3

Comparison of atomistic and elasticity approaches for carbon diffusion near line defects

Abstract

Energy barriers for carbon migration in the neighborhood of line defects in bcc iron obtained by atomistic (molecular statics) simulations are compared to the predictions of anisotropic elasticity theory. The agreement is better for the octahedral sites (energy minima) than for the tetrahedral sites (saddle points). Absolute differences in the energy barriers obtained by the two methods are usually below 5 meV at distances larger than 1.5 nm from the screw dislocation and 2 nm (up to 4 nm in the glide plane) from the edge dislocation. AKMC simulations performed at $T = 300$ K and additional analysis based on the activation energies show that the methods are in good qualitative agreement, despite some important quantitative discrepancies due to the largest absolute errors found near the dislocation cores.

3.1 Introduction

Elasticity theory has been long used to estimate the binding energy of dislocations with other lattice defects (e.g., interstitial and substitutional atoms, vacancies, other dislocations). In their pioneering work, Cottrell and Bilby estimated the binding energy between an edge dislocation and a carbon atom in solid solution in α-iron by considering only the size interaction between the defects [Cottrell 1949]:

$$E^b = -P\Delta V = \frac{1}{3}\mathrm{Tr}\left(\sigma^d_{ii}\right)\Delta V \tag{3.1}$$

where P, which is proportional to the trace of the dislocation stress tensor σ^d, corresponds to the pressure created by the dislocation at the position of the point defect and ΔV is the relaxation volume of the interstitial atom. Despite its simplicity, this approximation holds to a large extent for vacancies and substitutional atoms, known to act as dilatation centers, but it is not appropriate for an interstitial carbon atom that also induces tetragonal distortion in the iron matrix. Cochardt and co-workers improved this calculation by including also the local shear strain created by the interstitial atom (i.e., the shape interaction) [Cochardt 1955]. In both calculations, the dislocation stress field was obtained according to isotropic elasticity. However, owing to its cubic symmetry, bcc iron is anisotropic. This later motivated Douthwaite and Evans to introduce anisotropic elasticity within Cochardt's calculations [Douthwaite 1973].

It has been recently shown that results of elasticity calculations compare well to atomistic simulations on the interaction of vacancies with an edge dislocation in face centered cubic metals (Al, Au, Cu, Ni) [Clouet 2006]. Clouet and co-workers have also reported a good quantitative agreement between the carbon-dislocation binding energies obtained by atomistic simulations and anisotropic elasticity theory [Clouet 2008], provided that carbon-dislocation separation is larger than 2 nm (edge) and 0.2 nm (screw). It should be pointed out that isotropic elasticity predictions, in this case, provide only a qualitative accord with atomistic simulations. More recently, Hanlumyuang and others modeled carbon distribution and concentration around dislocations in bcc iron at $T = 300$ K and $T = 400$ K with a combination of DFT and anisotropic elasticity calculations, concluding that effects of chemistry and magnetism beyond those already reflected in the elastic constants can be safely neglected [Hanlumyuang 2010]. Taken together, those works provide evidence that a continuum approach based on anisotropic elasticity theory can accurately describe the interaction of a point and a line defect provided that they are separated by a minimum distance to be determined

on a case-by-case basis.

Energy barriers for transitions at the atomic scale are usually obtained by atomistic simulations, as reported in Chapter 2. These simulations provide an approximate description of the true chemical environment by employing some simplified description of the atomic interactions involved. On one hand, it is true that this approach represents an extraordinary gain in computational time compared to state-of-the-art DFT calculations, which explicitly take into account the electronic structure contribution. On the other hand, depending on the system size and number of simulations, computational time remains an important issue. The next step is therefore to check whether elasticity calculations are also accurate when applied to the study of diffusion of an impurity that interacts with a dislocation. Indeed, in a recent work, Chen and co-workers employed elasticity to obtain energy barriers to feed a KMC simulation performed to investigate the role of solute segregation on the strength and the evolution behavior of dislocation junctions [Chen 2008]. However, in their model, the saddle point energies have been assumed to be constant.

In this chapter, the carbon-dislocation binding energies and the energy barriers for carbon migration in the neighborhood of an edge and a screw dislocation have been calculated by anisotropic elasticity theory and compared to the results of the molecular statics simulations presented in Chapter 2. The aim is to assess the extent to which carbon diffusion in a bcc Fe lattice strained by the presence of dislocations can be described purely by the elastic interactions between the point and the line defect.

3.2 Elasticity approach for the interaction between point and line defects

In contrast with atomistic simulations, elasticity theory assumes a continuum description of a material. The underlying chemistry or other atomic properties of the host crystal not reflected in the elastic constants are not considered. The elastic constants of the bcc iron matrix corresponding to the Fe-Fe potential are $C_{11} = 243$, $C_{12} = 145$ and $C_{44} = 116$ GPa. Within elasticity theory, a point defect, such as carbon, is seen as a singular source of stress and modeled by its force moment tensor, also called the "elastic dipole", P_{ij} [Bacon 1980].

The elastic dipole P_{ij} can be readily deduced from atomistic simulations by introducing the point defect in a simulation box of fixed volume V with periodic boundary conditions in all directions, and then performing full coordinate opti-

mization with a molecular statics algorithm (e.g., conjugate gradient). Elasticity theory then predicts that the homogeneous stress which develops in the simulation box varies linearly with the inverse of the volume according to the following equation:

$$\sigma_{ij} = -\frac{1}{V} P_{ij} \tag{3.2}$$

Both the O- and T- interstitial sites have a tetragonal symmetry with the tetragonal axis defined by the variant type. In the orientation given by $\vec{u}_x = (1,0,0)$, $\vec{u}_y = (0,1,0)$ and $\vec{u}_z = (0,0,1)$, the elastic dipole tensor P_{ij} should therefore take the following form:

$$(P_{ij}) = \begin{pmatrix} P_{xx} & 0 & 0 \\ 0 & P_{yy} & 0 \\ 0 & 0 & P_{zz} \end{pmatrix} \tag{3.3}$$

with only two different diagonal terms ($P_{yy} = P_{zz}$ for instance for the [100] variant). As a consequence of Eq. (3.2), shear components of the stress tensor vanishes and the off-diagonal terms obey the same symmetry.

Fig. 3.1 presents $\sigma_{ij}(1/V)$ for a carbon atom in a [100] octahedral variant. The corresponding values of the non-zero components of the P_{ij} tensor are $P_{xx} = 8.03$ eV and $P_{yy} = P_{zz} = 3.40$ eV. For the other two O-variants, the values of P_{ii} are obtained by performing the appropriate permutations. In the same figure we can see also $\sigma_{ii}(1/V)$ for the [010] T-variant. In this case we have $P_{xx} = P_{zz} = 6.66$ eV and $P_{yy} = 4.87$ eV. Similar to the O-variants, the diagonal components of the P_{ij} tensor must be permuted to find the ones corresponding to the other two T-variants.

From the P_{ij} tensor associated with one of the interstitial sites, the corresponding relaxation volume ΔV of carbon in bcc iron within the elastic model is easily obtained by the following equation:

$$\Delta V_{[O|T]} = \frac{\mathrm{Tr}(P_{ij})}{C_{11} + 2C_{12}} \tag{3.4}$$

which results in $\Delta V_O = 0.0045$ nm^3 and $\Delta V_T = 0.0055$ nm^3. The migration volume $\Delta V_m = \Delta V_T - \Delta V_O = 0.001$ nm^3 compares well to experimental results [Wuttig 1971, Bosman 1960, Bass 1962].

Anisotropic elasticity theory [Eshelby 1955, Douthwaite 1973] with the formulation of the elastic dipole by Bacon and co-authors [Bacon 1980] establishes that the binding energy between a point defect and a dislocation is obtained by the following equation:

$$E^b = P_{ij} \epsilon^d_{ij} \tag{3.5}$$

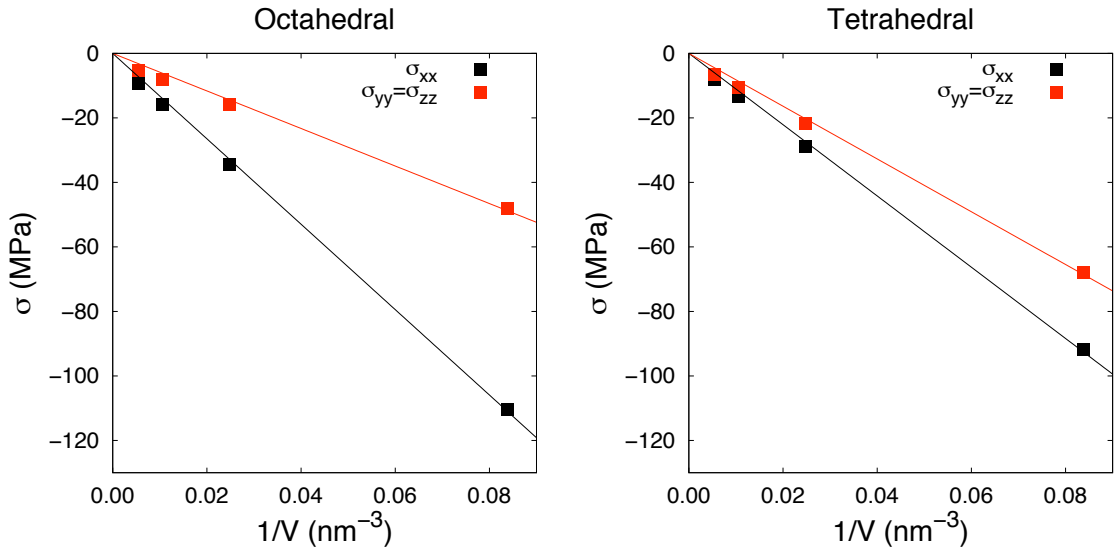

Figure 3.1: Stress as a function of the inverse of the simulation box volume for a simulation box with a carbon atom sitting in either a [100] O-variant or [010] T-variant. Symbols refer to atomistic simulations results and lines represent their linear regression.

where ϵ^d_{ij} is the strain field of the dislocation at the location of the point defect [Stroh 1962, Stroh 1958]. After obtaining the binding energies for a carbon atom occupying an O- or T-site, the corresponding energy barrier can be obtained by rearranging Eq. (2.5):

$$E_{[O|T],carbon+dislo} = E_{[O|T],carbon} + E_{dislo} - E^b_{[O|T],elast} \tag{3.6}$$

and then taking the difference in Eq. (1.4):

$$\begin{aligned} E^m_{elast} &= E_{T,carbon+dislo} - E_{O,carbon+dislo} \\ &= E_{T,carbon} + E_{dislo} - E^b_{T,elast} - \left(E_{O,carbon} + E_{dislo} - E^b_{O,elast}\right) \\ &= E^m_{bulk} - E^b_{T,elast} + E^b_{O,elast} \end{aligned} \tag{3.7}$$

where $E^m_{bulk} = E_{T,carbon} - E_{O,carbon} = 0.816$ eV is the energy barrier for carbon migration in a non-strained iron matrix.

3.3 Comparison of elasticity calculations to atomistic simulations

3.3.1 Differences in the migration energies

Anisotropic elasticity calculations have been carried out with the Babel code, developed by E. Clouet at CEA-Saclay. To obtain the binding energies $E^b_{O,elast}$ and $E^b_{T,elast}$ with Eq. (3.5), first the P_{ij} tensors associated with the O- and T-sites were rotated according to the orientation of the simulation boxes used in atomistic simulations (see Fig. 2.4) in order to describe the local stress field of the carbon atom with respect to the dislocation line. Then the Volterra displacement field of the edge or the screw dislocation was applied to the positions of the interstitial sites found in a non-strained bcc iron lattice.

A mapping of the absolute differences between the binding energies obtained by atomistic simulations and elasticity calculations (i.e., $|\Delta E^b_{[O|T]}| = |E^b_{[O|T],atom} - E^b_{[O|T],elast}|$) can be seen in Figs. 3.2 and 3.3 for carbon positions around an edge and a screw dislocation. Such differences represent the absolute errors that one should expect by replacing molecular statics by anisotropic elasticity theory. Not surprisingly, the agreement is much better when the carbon atom is closer to the screw than to the edge dislocation. A point raised by Ref. [Clouet 2008] helps to explain this discrepancy. In the elasticity calculations, only the Volterra displacement field of the dislocations has been taken into account. Nonetheless, the relaxation of the dislocation core and its surroundings with the current EAM potential yields an additional, shorter in range, displacement field. Considering that such a relaxation is larger for the edge dislocation than for the screw dislocation, the resulting change of the dislocation stress field also is larger. For the T-sites, one can see that near the dislocation line the agreement is not as good as for the O-sites. We found a particularly noticeable discrepancy for the [010] T-variant in the vicinity of the edge dislocation glide plane, for which elasticity theory predicts almost no interaction between the defects ($E^b_{T,elast} < 10^{-7}$ eV), in great contrast with atomistic simulations ($E^b_{T,atom}$ is in the order of 10^{-3} eV), so that we have $|\Delta E^b_T| \approx |E^b_{T,atom}|$. Consequently, the relative error in this case is enormous. The absolute error, in turn, is small simply because $|E^b_{T,atom}|$ is small. As we have seen in Chapter 2, when a carbon approaches an edge dislocation along its glide plane and reaches a distance of approximately $3.5b$ from the dislocation line, the edge dislocation leaves its initial position and moves towards the interstitial atom. Since the carbon-dislocation

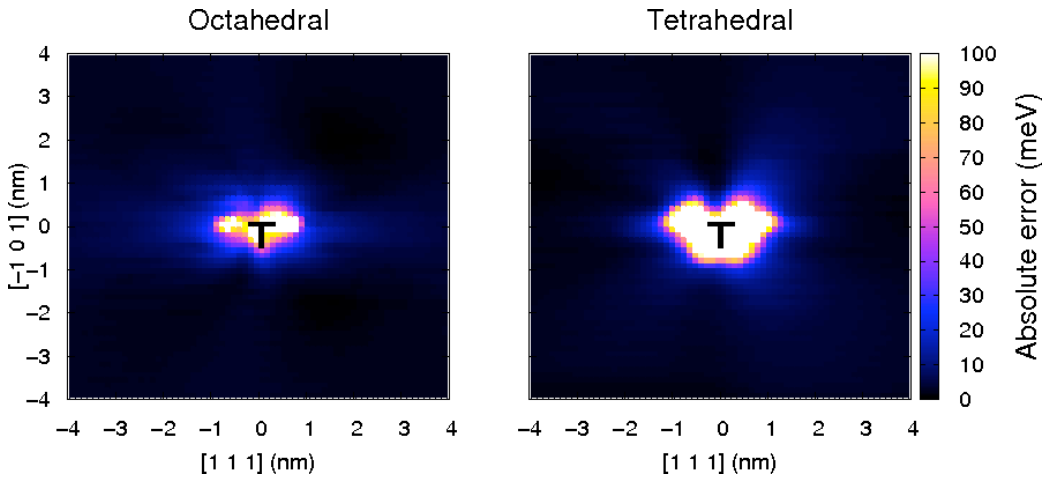

Figure 3.2: Mapping of absolute differences (errors) $|\Delta E^b|$ between the binding energies obtained by atomistic simulations and anisotropic elasticity calculations as a function of carbon position around an edge dislocation.

separation is no longer the same as in elasticity calculations, it is worthless to compare the methods in this situation.

The energy barrier E^m_{elast} was obtained according to Eq. (3.7). The mapping of the absolute errors $|\Delta E^m|$ between energy barriers obtained by each method is shown in Fig. 3.4. Despite the fact that errors in binding energies may be cumulative in Eq. (3.7), from a qualitative point of view, the energy barriers calculated by both methods present the same trend. The relative errors in the energy barriers are usually very low (less than 5%). One can see that $|\Delta E^m|$ is larger around an edge dislocation (ranging from 4 to 6 meV on average) than around the screw dislocation (generally below 3 meV). Moreover, $|\Delta E^m|$ is within the same order of magnitude of energy convergence in atomistic simulations (between 1–2 meV), except very close to the dislocation core. Although $|\Delta E^m|$ is small in absolute terms, it is worthwhile to point out that, in statistical mechanics, quantities that depend on migration energies (e.g., the probability of a carbon jump in bcc iron) are proportional to the Boltzmann factor $\exp(-E^m/kT)$, where k is the Boltzmann constant and T is temperature. Consequently, owing to the exponential dependence, even small errors in the activation energies may yield large differences in the final results. For instance, if a threshold of about 20% is tolerated for the relative error in quantities determined by the Boltzmann factor, at room temperature ($T = 300$ K) it means a maximum absolute error of only 5 meV in the activation energies. This implies a minimum carbon-dislocation separation of about 1.5 nm for the screw dislocation and of about 2 nm for the edge dislocation (up to 4 nm in its glide plane).

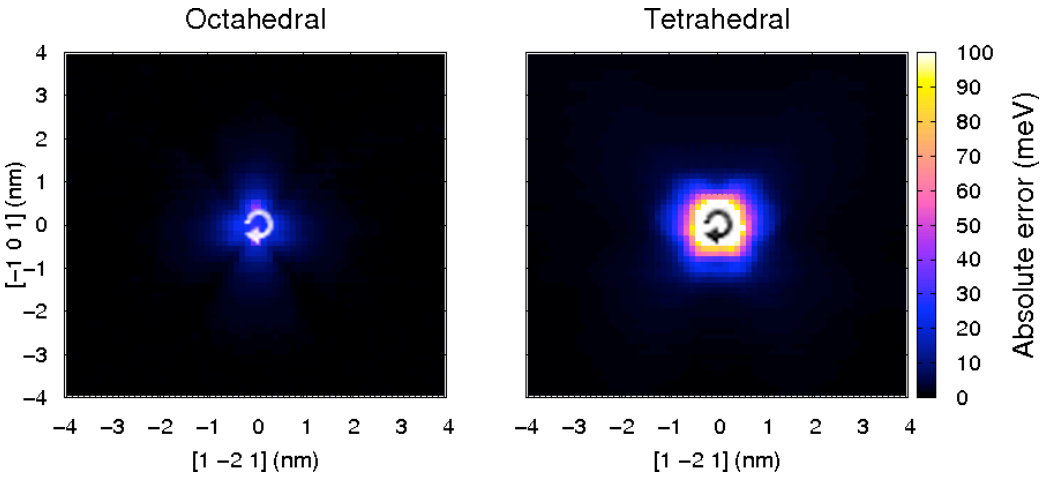

Figure 3.3: Mapping of absolute differences (errors) $|\Delta E^b|$ between the binding energies obtained by atomistic simulations and anisotropic elasticity calculations as a function of carbon position around a screw dislocation.

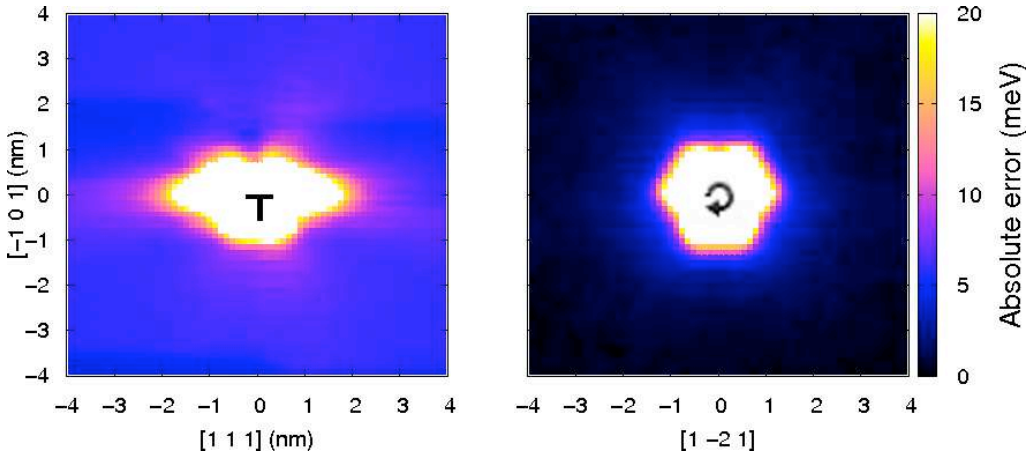

Figure 3.4: Mapping of absolute differences (errors) $|\Delta E^m|$ between the energy barriers obtained by atomistic simulations and anisotropic elasticity calculations as a function of carbon position around an edge (left) or a screw (right) dislocation.

3.3.2 Dislocation-induced bias on carbon diffusion

In Chapter 2, it has been shown that a dislocation induces a location-dependent bias on the random walk performed by a carbon atom as it interacts with the stress field of the line defect. Figs. 3.5 and 3.6 allow to compare the mean displacement vectors $\langle\vec{d}\rangle_{atom}$ and $\langle\vec{d}\rangle_{elast}$ around an edge and a screw dislocations, respectively, for $T = 300$ K (only vectors with a magnitude greater than 10^{-3} nm are shown). For the edge dislocation, both methods predict that a carbon atom above the glide plane tends to go to the dislocation core. On the other hand, below the glide plane (region under compression), the carbon atom tends to move obliquely with respect to the dislocation core towards the glide plane. For the screw dislocation, one can see that the bias is much less pronounced than in the edge case. Both methods reflect in a similar way the effect of the three-fold symmetry of the screw dislocation stress field on carbon diffusion: attractive (repulsive) zones are separated by 120°.

3.3.3 Carbon diffusion to dislocations

In order to evaluate how the differences in the activation energies affect the simulated kinetics of carbon diffusion near a dislocation, we also performed AKMC simulations with transition rates obtained by elasticity calculations at $T = 300$ K and compared to the simulations presented in Chapter 2 at the same temperature. The simulation box in this case also consisted of a cylinder of radius 6 nm with two absorbing barriers in the directions perpendicular to the dislocation line: the dislocation core (an inner cylinder of radius $4b$) and the open outer boundary. Periodic boundary conditions were only used in the z direction, parallel to the dislocation line.

Starting by the edge dislocation, atomistic simulations and elasticity calculations are in agreement when predicting the amount of trajectories that ended in the dislocation core (about 34%; 27% in simple random walks). Thus the probability that a carbon atom will be trapped by the edge dislocation instead of leaving the simulation box is the same for both methods. As previously said, a feature of the edge dislocation is to split the simulation box into two different regions, one under tension and the other under compression (above and below the glide plane, respectively). We have seen that, irrespective of the method employed to obtain the migration energies, about 3/4 of the stress-assisted carbon trajectories that ended in the core of the edge dislocation started in the tension half. Moreover, considering only the carbon atoms trapped by the core whose

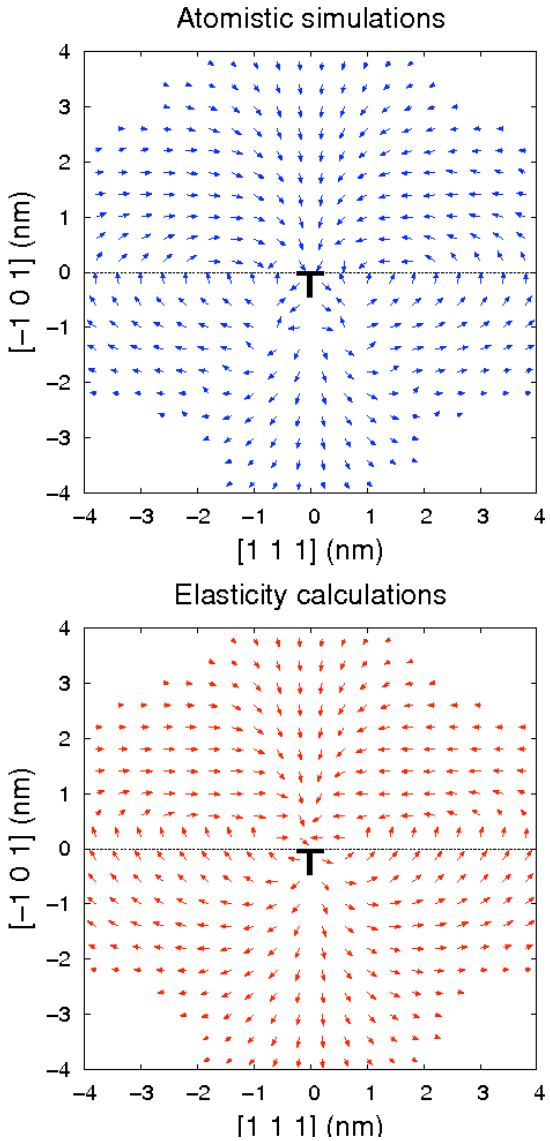

Figure 3.5: Mean displacement vectors $\langle\vec{d}\rangle_{atom}$ and $\langle\vec{d}\rangle_{elast}$ in the vicinity of an edge dislocation at $T = 300$ K. Only vectors with lengths greater than 10^{-3} nm are plotted. For the sake of readability the vectors were multiplied by 100. The z component (parallel to the dislocation line) is not shown. Each arrow corresponds to a vector which is in fact the resulting vector in an area of 0.4×0.4 nm^2.

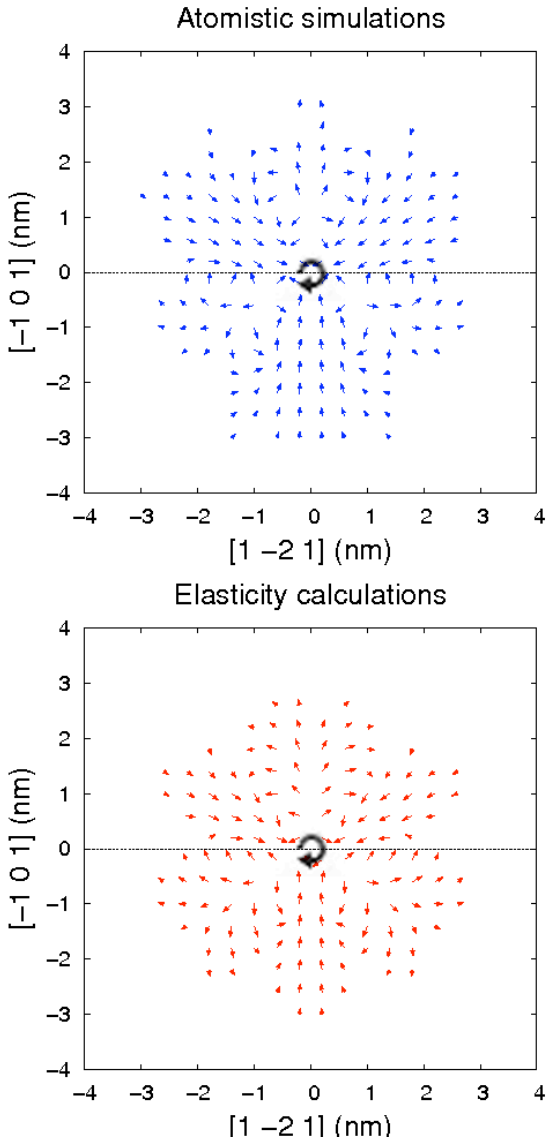

Figure 3.6: Mean displacement vectors $\langle \vec{d} \rangle_{atom}$ and $\langle \vec{d} \rangle_{elast}$ in the vicinity of screw dislocation at $T = 300$ K. Only vectors with lengths greater than 10^{-3} nm are plotted. For the sake of readability the vectors were multiplied by 100. The z component (parallel to the dislocation line) is not shown. Each arrow corresponds to a vector which is in fact the resulting vector in an area of 0.4×0.4 nm^2.

Dislocation	Method	n	D (m^2/s)
Edge	Molecular statics	0.62	4.2×10^{-21}
	Elasticity calculations	0.66	2.5×10^{-21}
	Simple random walk	0.65	2.6×10^{-21}
Screw	Molecular statics	0.75	2.3×10^{-21}
	Elasticity calculations	0.70	1.7×10^{-21}
	Simple random walk	0.64	2.6×10^{-21}

Table 3.1: Kinetic parameters obtained from AKMC simulations after fitting to Eq. (2.4).

trajectories started in the half under compression, more than 80% diffused first towards the glide plane before being led to the dislocation core. Therefore, it is very unlikely according to both methods that a carbon atom arrives to the core of an edge dislocation coming directly from the compression region. Regarding the screw dislocation, in contrast with edge, the probability that carbon trajectories generated from the atomistic-calculated migration energies terminates in the screw dislocation core (32%) is slightly higher than for elasticity results (29%).

We have also checked whether atomistic simulations and elasticity calculations yield similar kinetics of carbon diffusion to dislocations. The evolution of the fraction of carbon atoms trapped by the edge or the screw dislocation is depicted in Fig. 3.7. The curves show the well-known sigmoidal shape usually reported in aging experiments [Lavaire 2001, Lavaire 2004, De 2001]. There is also a delay in elasticity-informed AKMC simulations with respect to atomistic-informed ones that starts since the first carbon atoms are trapped by the dislocation. Those are generally the ones closest to the dislocation core, thus suggesting this is a cumulative effect of the increasing absolute errors as the carbon atom approaches the sink. Simulation results were also fitted to Eq. (2.4) in the same way as in Chapter 2; the corresponding kinetic parameters n and D are shown in Table 3.1 for comparison. The $t^{\frac{2}{3}}$ kinetic law, again with small deviations, also holds for the trajectories generated from elasticity-calculated transition rates. One can see that the effective diffusion coefficients obtained from elasticity-informed AKMC simulations are smaller than the ones from atomistic-informed simulations, but within the same order of magnitude.

3.3.4 The mean residence time

The speed of a diffusional process in the solid state is related to the mean elapsed time $\langle\tau\rangle$ that the system spends at every accessible state. The mean elapsed time

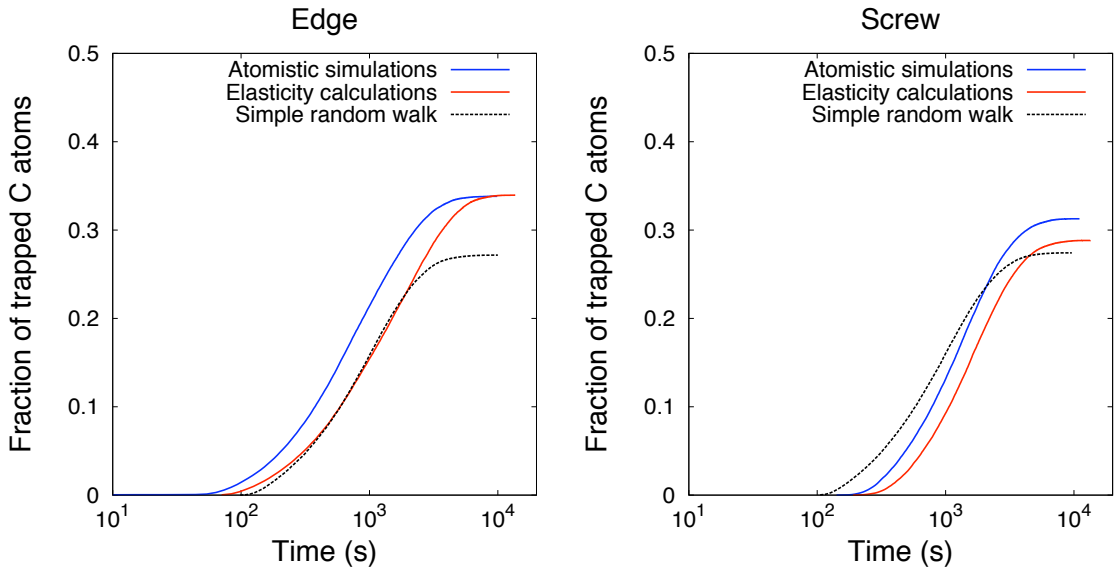

Figure 3.7: Fraction of carbon trajectories that terminated in the region defined as the core ($R < 4b \approx 1$ nm) of either an edge or a screw dislocation during AKMC simulations as a function of time at $T = 300$ K.

in a specific location i can be calculated by [Voter 2002]:

$$\langle \tau \rangle = \frac{1}{\Omega_i} = \left[\nu_0 \sum_{j=1}^{N} \exp\left(\frac{-E^m_{i \to j}}{kT} \right) \right]^{-1} \tag{3.8}$$

In this equation, Ω_i is the sum of the transition rates that the system can undergo starting from state i and ν_0 is the attempt frequency, in the order of 10^{13} Hz. In Figs. 3.8 and 3.9, a mapping of $\langle \tau \rangle$ as a function of carbon position with respect to the dislocation line at $T = 300$ K obtained by atomistic simulations and elasticity calculations is shown. For comparison, $\langle \tau \rangle \approx 1.25$ s for $E^m = 0.816$ eV (simple random walk) and the same ν_0. One can see that, around an edge dislocation, $\langle \tau \rangle_{atom}$ and $\langle \tau \rangle_{elast}$ exhibits the same trend: the carbon atom diffuses faster as it approaches the dislocation in the region under tension and slower as it does the same coming from the region under compression or in the vicinity of the glide plane. On the other hand, the cumulative effect of the differences in the migration energies calculated by each method is also evident. The mean relative errors as a function of distance to the edge dislocation line between $\langle \tau \rangle_{atom}$ and $\langle \tau \rangle_{elast}$ reveal that elasticity calculations leads to an overestimation of the mean elapsed time (and, consequently, underestimation of the diffusivity) with respect to atomistic simulations of at least 20% (reaching 50% near the core) within the maximum radius of 6 nm considered in this work. Disagreement between $\langle \tau \rangle_{atom}$ and $\langle \tau \rangle_{elast}$, in turn, becomes noticeable only when the carbon atom is about 2

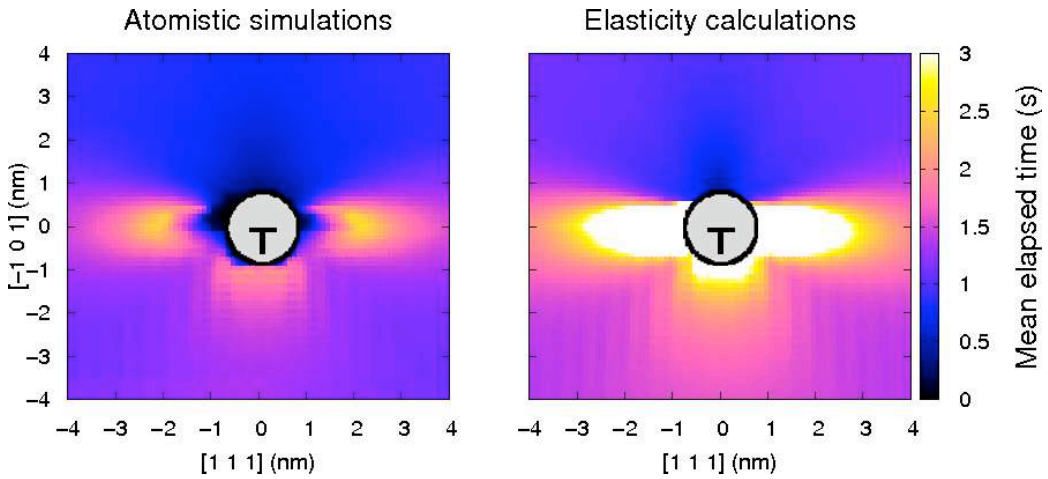

Figure 3.8: Mapping of mean elapsed times $\langle\tau\rangle_{atom}$ and $\langle\tau\rangle_{elast}$ at $T = 300$ K as a function of carbon position with respect to the edge dislocation line. The gray circle in the center (diameter equals to $8b$) refers to the region defined as the dislocation core.

nm away from the screw dislocation line. An interesting point is that the EAM potential (and also elasticity) predicts that the carbon atom diffuses slower as it approaches the core of a screw dislocation, thus explaining the delay of stress-assisted trajectories with respect to simple random walks in Figs. 3.7 and 2.17. It is also the same picture found in the vicinity of the glide plane of an edge dislocation, where σ_{xy} is the predominant component of the stress tensor. This suggests that shear stress slows down carbon diffusion.

3.4 Overview

The results of two different methods that can be applied to obtain carbon migration energies near dislocations in α-iron have been presented in this chapter. Atomistic simulations describe the Fe-C system as an ensemble of particles that interact with each other according to an interatomic potential, in this work, an EAM potential fitted to *ab initio* calculations. Anisotropic elasticity theory, in turn, considers a continuum medium distorted by the strain fields of the line and the point defect. Despite such an important difference, the methods agree reasonably (absolute errors of less than 5 meV on average) if the carbon atom is far enough from the dislocation lines. However, it should be pointed out that even small absolute errors in the migration energies may lead to significative temperature-dependent errors in quantities that depend on the Boltzmann factor. Indeed, some important discrepancies have been found in AKMC simulations performed at $T = 300$ K, thus indicating that the atomistic treatment still is nec-

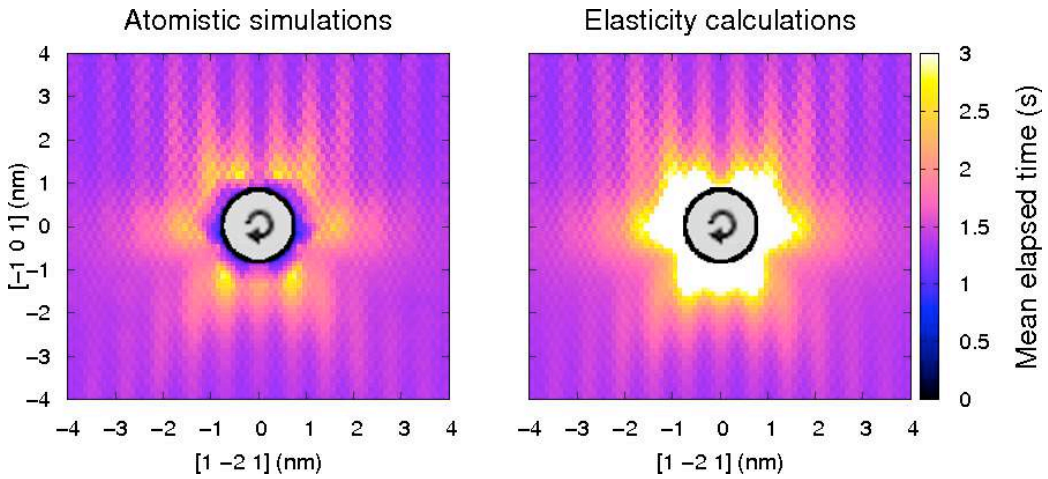

Figure 3.9: Mapping of mean elapsed times $\langle\tau\rangle_{atom}$ and $\langle\tau\rangle_{elast}$ at $T = 300$ K as a function of carbon position with respect to the screw dislocation line. The gray circle in the center (diameter equals to $8b$) refers to the region defined as the dislocation core.

essary when examining carbon behavior in the vicinity of the dislocation core, where errors due to the elasticity approximation are the largest. In future work, atomistic simulations and anisotropic elasticity calculations may be incorporated into a single model using AKMC simulations to investigate the dynamics of Cottrell atmosphere formation in α-iron.

3.5 Ongoing work

Mesoscopic models based on an elastic description of the interaction between point defects and dislocations were already used to simulate Cottrell atmosphere formation in α-iron. For instance, Krempaszky *et al* performed finite element calculations to model carbon segregation to dislocations in bcc iron [Krempaszky 2006], obtaining good agreement with aging experiments. However, such models do not draw a fine picture of the segregation process. In other words, the actual carbon trajectories are not simulated at all. Since the segregation process spans long time scales (from a few hours up to some days), far beyond what can be achieved by molecular dynamics, it remains a seemingly insurmountable challenge to atomistic approaches based on time discretization.

The results presented in this chapter, in turn, allow us to envisage a protocol to employ AKMC to perform realistic atomic scale simulations of carbon segregation to dislocations and the consequent formation of Cottrell clouds while keeping computational time reasonable. This can be achieved by partitioning the process of obtaining the energy barriers for AKMC simulations as follows (Fig. 3.10):

1. In order to speed up AKMC simulations, a static catalog should be employed in situations where the transitions that the system can undergo are predictable:

   (a) **Region 1**: Migration energies of a single point defect in the far-field (the predominant situation in the beginning of the dynamics) should be obtained from elasticity calculations. Those calculations are very fast: running on a single CPU, about one million carbon-dislocation binding energies, subsequently used in Eq. (3.7) to calculate the energy barriers, can be obtained in less than one minute.

   (b) **Region 2**: At a given carbon-dislocation separation (according to a user-defined threshold), atomistic simulations should be employed rather than elasticity for the sake of accuracy. Atomistic simulations of a few thousands sites will usually last one or two months running on a medium-sized cluster built with today's technology CPUs.

2. **Region 3**: Additionally, an on-the-fly approach to obtain saddle point energies as the AKMC simulation runs has to be employed in the dislocation core, where lattice is too distorted. Moreover, in this region, two or more carbon atoms are expected to interact with each other as carbon concentration increases. A method such as ART [Barkema 1996, Cancès 2009] or its simplification presented in Chapter 1 (TaR) can be used to build the connectivity between neighboring states and then a method such as NEB (or, even better, CI-NEB) can be used to obtain saddle point energies. An example of on-the-fly AKMC simulations (vacancy diffusion in silicon) is presented by F. El-Mellouhi and co-workers in Ref. [El-Mellouhi 2008].

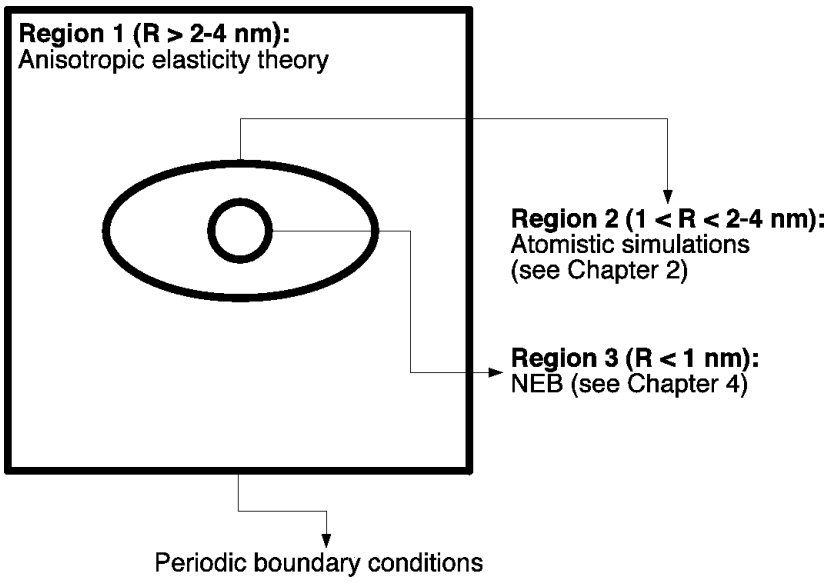

Figure 3.10: The AKMC simulation box is divided into three different regions. In the far-field, the energy barriers are calculated by anisotropic elasticity theory. At some carbon-dislocation separation, where anisotropic elasticity theory does not give accurate results, atomistic simulations have to be employed for this purpose. In the dislocation core, where the crystal is too distorted and the carbon atoms are expected to strongly interact with each other as carbon concentration increases, a method such as NEB is more appropriate. Periodic boundary conditions can be enforced in the far-field, where carbon-dislocation interaction is negligible.

Chapter 4

Pipe diffusion

Abstract

The behavior of a single carbon atom in the tight channel surrounding an edge or a screw dislocation in α-iron has been simulated by atomistic kinetic Monte Carlo. In these simulations, pipe diffusion has been observed in the core of an edge dislocation at $T \geq 400$ K and in the core of a screw dislocation at $T \geq 750$ K. Below these temperatures, instead of diffusing freely in the dislocation channel, the carbon atom has been seen to remain performing back and forth jumps at high frequencies between a few sites separated by low energy barriers. This behavior has also been observed in molecular dynamics simulations. The effective diffusion coefficient for carbon migration in the dislocation pipe calculated from the AKMC-generated carbon trajectories is about two orders of magnitude larger than the diffusion coefficient in the bulk. The effective activation energies in the core of an edge or a screw dislocation have also been calculated: 0.670 eV and 0.738 eV, respectively.

4.1 Introduction

The disordered core region of dislocations has long been assumed to be a channel through which fast unidimensional diffusion takes place. In a classical work, Love coined the term "pipe diffusion" for it, in use since then [Love 1964]. Pipe diffusion is expected to play a role as important as bulk diffusion in the aging of materials. For instance, since the vicinity of a dislocation is an ideal environment for the nucleation of precipitates in the latest stages of the aging process, the dislocation core itself could act as a fast route through which impurities travel and end up feeding a growing precipitate particle situated at some point along the dislocation line. Pipe diffusion has been also pointed out as the dominant mechanism in the dynamic strain aging of metals [Kalk 1995, Ling 1993, Picu 2004], which results in the Portevin-LeChatelier effect [Mesarovic 1995]. According to this interpretation of DSA, impurities in the atmospheres surrounding dislocations in a forest migrate to a mobile dislocation temporarily arrested by the forest.

Despite the fact that pipe diffusion has attracted so much attention because of its scientific and technological implications, direct experimental observations at the atomic scale still are scarce. Legros and co-workers, in a recent groundbreaking experiment [Legros 2008], were able to carry out real-time observation via *in situ* transmission electron microscopy (TEM) of silicon diffusion through a single dislocation connecting two silicon precipitates of different sizes in an aluminum thin film (see Fig. 4.1) for temperatures ranging from 623 K to 723 K. In the interpretation of the experimental findings, Legros and co-workers have concluded that the dislocation pipe does act as a high-diffusivity channel, with an effective diffusion coefficient many orders of magnitude higher (and an effective activation energy 20% smaller) than in the bulk. The pipe cross section used in the calculation of diffusivity was chosen as a disk with radius equal to one Burgers vector length. This choice was based on the computational work reported by Picu and Zhang on the pipe diffusion of a manganese atom in aluminium [Picu 2004] and is not free of controversy. Thus far, the actual pipe diffusion mechanism has not been established either experimentally or theoretically.

From a theoretical/computational point of view, pipe diffusion in a variety of materials has been investigated preferentially by molecular dynamics simulations [Huang 1989, Tapasa 2007, Purja 2009, Zhang 2010a, Zhang 2010b]. These works provided important insights into this intriguing phenomenon, but none of them appear to reveal actual mass transport along the dislocation pipe, which is in contradiction with the dislocation acting as a fast diffusion channel. Tapasa and co-workers, for instance, performed MD simulations at $T = 600$, 800, and 1200 K

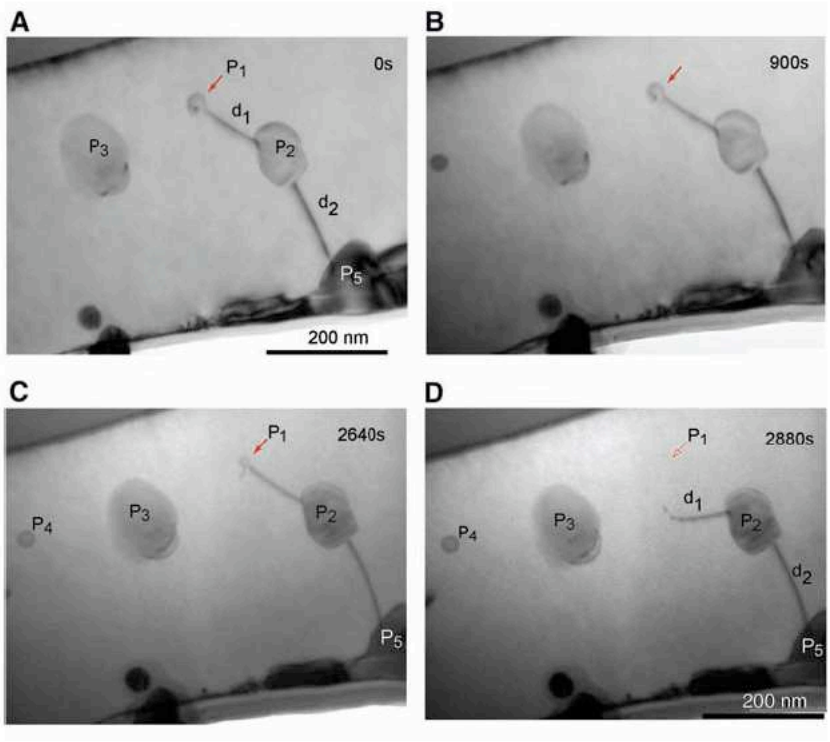

Figure 4.1: *In situ* TEM observation of precipitate dissolution through a dislocation at T=623 K. P_1 to P_5 are Si nanoprecipitates, and d_1 and d_2 are dislocation segments. Only P_1 dissolves abnormally fast, because d_1 acts as a short circuit for diffusion. Figure taken from Ref. [Legros 2008].

[Tapasa 2007]. They verified that a carbon atom trapped by an edge dislocation in bcc iron jumps back and forth in the core (i.e., no actual diffusion along the line is observed). One of the principal conclusions drawn from the results of Ref. [Tapasa 2007] is that mass transport along the line of an edge dislocation should only occur if the line itself moves. Furthermore, additional interpretation of the results indicates that pipe diffusion should be strongly dependent on the dislocation orientation. In this chapter, we report a study based on AKMC simulations, which is still underway, on the behavior of a carbon atom in the core of an edge and a screw dislocation in bcc iron.

4.2 Energy calculations

4.2.1 Energy minima

Molecular statics simulations were carried out with LAMMPS to obtain the energy minima in the volume defined *ad hoc* as the core region in Chapter 2 (i.e., a cylinder of radius $4b \approx 1$ nm around the dislocation line). The simulation boxes employed in molecular statics simulations consisted of cylinders of radius 7.5 nm (half the radius of the simulation boxes depicted in Fig. 2.4) with the dislocation line as the axis. Following the same simulation protocol reported in Chapter 2, the iron atoms in a 2 nm thick outer layer were kept fixed, so as to permanently represent the dislocation strain field in the far-field. Periodic boundary conditions were applied only along the dislocation line. The dislocations were assumed to be straight and immobile in the center of the simulation box.

Outside the core region, the bcc iron matrix is only slightly distorted by the strain field of a dislocation. Consequently, it was just necessary to implement a simple algorithm to identify the interstitial positions (octahedral sites) that corresponded to the energy minima. In the core region, particularly near the dislocation line, the lattice is too distorted and it is not trivial to guess the location of an energy minimum thereby. Our approach to handle this problem was the easiest to implement: every midpoint between two neighboring iron atoms was taken as a position that might accommodate a carbon atom. For each interstitial position candidate, a carbon atom was inserted there and geometry optimization was performed with the conjugate gradient algorithm. As one should expect, many of these initial positions revealed to be unstable after geometry optimization. In the volume of interest, we were able to identify about 800 stable interstitial positions per nanometer of dislocation for both dislocation types.

The energetically stable positions where a carbon atom can be found in the re-

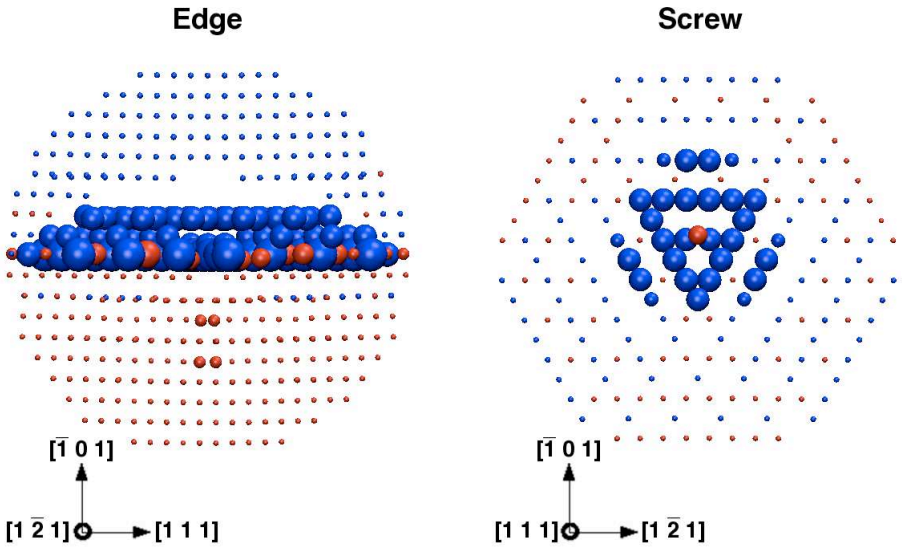

Figure 4.2: Energy minimum positions that can be occupied by a carbon atom in the region defined as the core of an edge and a screw dislocation ($R \leq 4b \approx 1$ nm). Blue (red) balls represent positive (negative) carbon-dislocation binding energies. The ball sizes are proportional to the binding energies. The dislocation lines (in the center) are perpendicular to the plane of the page.

gion defined as the dislocation core are represented in Fig. 4.2. Carbon-dislocation binding energies referring to about 34% (edge) and 52% (screw) of these positions lie in the interval $(-0.10, 0.10)$ eV. The largest carbon-dislocation binding energy was found when the carbon atom occupies some positions in the glide plane of an edge dislocation: 0.65 eV. The largest binding energy of a carbon atom to a screw dislocation (0.41 eV) was about 40% smaller than to an edge dislocation, in agreement with previous work using the same EAM potential [Clouet 2008]. Note that the maximum carbon-dislocation binding energy estimated by anelastic measurements (either Snoek or cold-work damping peak) ranges from 0.45 eV to 0.75 eV (the dislocation types are not identified in these experiments) [K. Kamber 1961, Henderson 1972]. For an edge dislocation, the positions with both the largest and the smallest (up to -0.81 eV) carbon-dislocation binding energies are distributed on the glide plane and on the planes just above and below it. For a screw dislocation, one can see that the positions with the most significant binding energies form a triangular feature around the line defect. The smallest binding energy of a carbon atom to a screw dislocation (-0.58 eV) corresponds to the position that is the closest to the dislocation line.

4.2.2 Saddle points

As it has been seen in Chapter 2 (Fig. 2.7), even if the strain due to the line defects changes the energy barrier height, the minimum energy paths for carbon migration resemble the minimum energy path in the non-strained iron matrix. Therefore, we assumed that the tetrahedral site remained the saddle point under the low-to-moderate strain condition outside the dislocation core. However, when the carbon atom falls into the dislocation core, the lattice distortion is likely to strongly affect many of the minimum energy paths that can be followed by the interstitial atom. A more sophisticated method to estimate the saddle points becomes necessary in this situation. In this work, we performed CI-NEB simulations (as implemented by the LAMMPS code) for such purpose.

Before obtaining the minimum energy paths and the corresponding saddle points with CI-NEB, a list of first nearest neighbors had to be built. A problem that we had to face was to determine whether two energy minima were first nearest neighbors or not. Initially, a criterion based on the distance between two energy minima ($\leq a_0/2+\epsilon$, where a_0 is the lattice parameter and $\epsilon = 0.01$ nm was an arbitrary tolerance) was used. After applying this criterion, we verified that there were energy minima with less than four first nearest neighbors; indeed, some had no first nearest neighbor. To search for the first nearest neighbors of these energy minima, a simplification of the ART method [Barkema 1996, Cancès 2009], namely, the TaR method described in Chapter 1, was employed. A total of 12 attempts were performed searching for a maximum of 6 nearest neighbors per energy minimum. The TaR method allowed to establish links between two known energy minima and also to find a few unknown energy minima in the dislocation vicinity. In the subsequent CI-NEB simulations, every two neighboring energy minima were connected by 7 intermediate images built by interpolation of the atomic positions. Adjacent images, in turn, were coupled to each other by a spring with a spring constant k of 10 eV/nm. This chain of replicas was relaxed by damped molecular dynamics.

Fig. 4.3 shows the distribution of NEB-calculated energy barriers in the regions that have been defined as the cores of an edge and a screw dislocation. The lowest energy barriers found in these volumes were 0.14 eV (edge) and 0.19 eV (screw), therefore much lower than the energy barrier for carbon migration in the non-strained iron matrix (0.816 eV). On the other hand, the highest energy barriers were as high as 1.55 eV (edge) and 1.14 eV (screw).

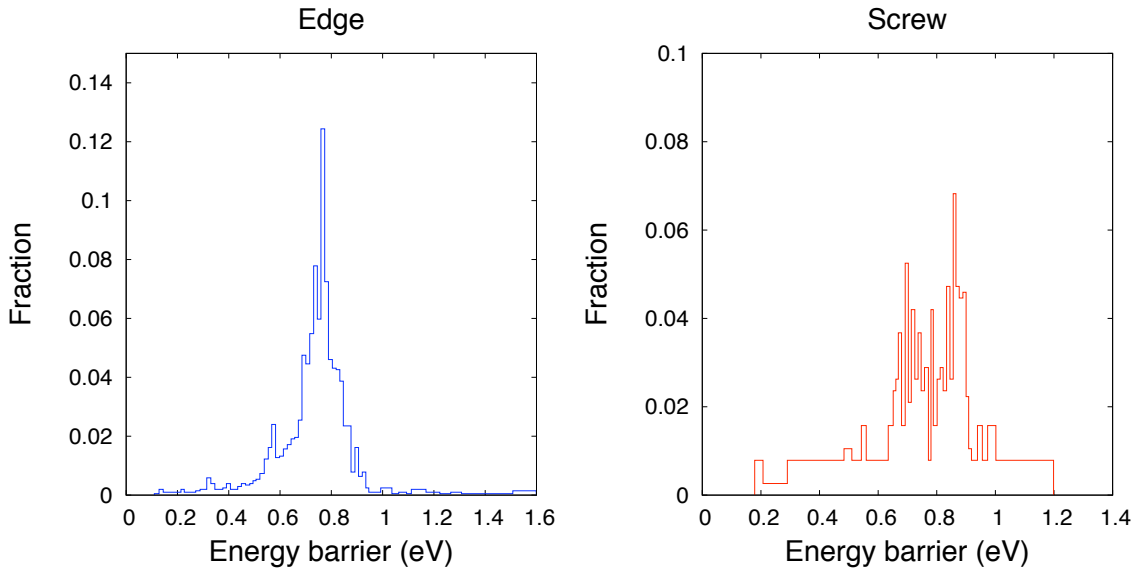

Figure 4.3: Energy barrier distribution in the regions defined as the core ($R < 4b \approx 1$ nm) of an edge and a screw dislocation.

4.3 Simulating carbon dynamics in the dislocation core

4.3.1 Atomistic kinetic Monte Carlo simulations

A first round of AKMC simulations using the NEB-calculated energy barriers and the corresponding transitions were performed where, for every simulated temperature (300–900 K), 1,000 runs were carried out. In every run, the carbon atom was placed in the first shell ($R < b$) surrounding the dislocation line and allowed to jump up to 100,000 times. Note that, for both dislocation types, the first shell contained the largest carbon-dislocation binding energies and the lowest energy barriers for carbon migration.

In these simulations, actual diffusion along the dislocation line is observed only at $T \geq 400$ K (edge) and $T \geq 750$ K (screw). By analyzing the simulated carbon trajectories, we notice that below these temperatures the carbon atom performs fast back and forth jumps within short circuits made of neighboring sites separated by low energy barriers: 0.33 eV or 0.42 eV (edge) and about 0.20 eV (screw). The sites belonging to this short circuits are enumerated and represented by spheres in Fig. 4.4. Taken together, they can be seen as a potential energy "superbasin". The energy barriers to escape the superbasins are 0.55 eV (edge) and 0.81 eV (screw).

Obviously, pipe diffusion is also expected to occur at low temperatures.

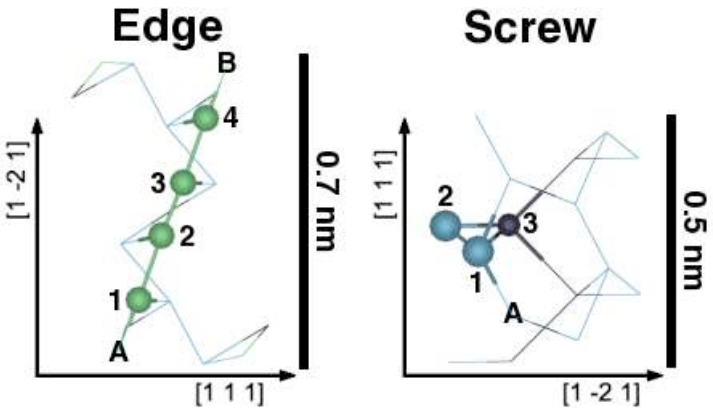

Figure 4.4: Minimum energy positions (wireframe nodes and spheres) where a carbon atom can be found in the first shell ($R \leq b$) surrounding the dislocation lines. Spheres represent sites that taken together form a superbasin where the carbon atom is trapped. Different colors account for the carbon-dislocation binding energy: 0.6–0.7 eV (green); 0.4–0.5 eV (blue); and 0.3–0.4 eV (black). Positions with negative binding energies are not shown. **A** and **B** are the sites imediately outside the superbasin. Maximum carbon-dislocation binding energy is 0.65 (edge) and 0.41 eV (screw).

Our AKMC implementation was not able to simulate pipe diffusion at low temperatures because it is affected by the low barrier problem mentioned by Ref. [Voter 2002]. It should be stressed that the existence of low barriers is not a problem in its own right. For instance, if two states i and j are such that $E^m_{i\to j} \ll E^m_{j\to i}$, once the system falls into state j coming from state i, it is very unlikely that the system will perform the inverse move. On the other hand, if $E^m_{i\to j} \approx E^m_{j\to i}$ and both energy barriers are much lower than the energy barriers to escape to other states, the system will be found performing thousands of fast transitions $i \rightleftarrows j$ in AKMC simulations, and diffusion is unlikely to be observed. The time scale that can be achieved by AKMC simulations also is strongly affected. As one can see in Fig. 4.5, the maximum simulated physical time in the core is very short compared to the maximum simulated physical time outside the core. Indeed, at room temperature, it is about ten orders of magnitude shorter. Unfortunately, for the moment, our simple AKMC implementation is not able to handle the low energy barrier problem properly.

Next we carried out much longer AKMC simulations (up to 10,000,000 steps) only for temperatures where pipe diffusion was expected to be observed with Algorithm 1.1. Examples of these long AKMC-generated trajectories can be seen in Figs. 4.6 and 4.7. It is clear from these figures that diffusion is restricted to the vicinity of the dislocation line, as one should expect if pipe diffusion is occurring. From the carbon trajectories thus simulated, we calculated the mean squared

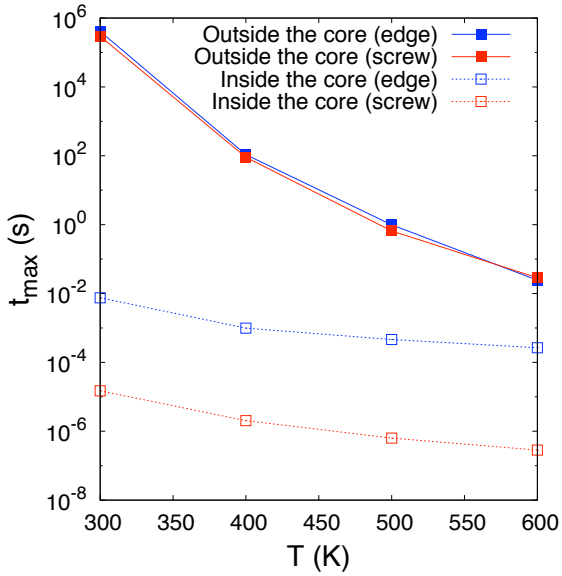

Figure 4.5: Maximum physical time achieved in individual AKMC simulations (up to 100,000 AKMC steps) as function of temperature.

displacement $\langle (z(t))^2 \rangle$ along the dislocation line. In one dimension, the Einstein formula for particle diffusion is:

$$D = \frac{\langle (z(t))^2 \rangle}{2t} \tag{4.1}$$

The effective pipe diffusion coefficient D in the core of an edge or a screw dislocation is just the slope of $\langle (z(t))^2 \rangle$, which, at large t, can be approximated to a straight line. Fig. 4.8 shows a plot of the pipe diffusion coefficients as function of the inverse of the temperature compared to the isotropic bulk diffusion coefficient (also calculated from AKMC simulations). These results are in agreement with the assumption accepted for a long time that pipe diffusion is faster than bulk diffusion (in our case, by about two orders of magnitude). From the slope of $D(1/T)$, the effective activation energy E^m_{eff} for pipe diffusion can be readily calculated. Both E^m_{eff} and the pre-exponential factor D_0 are presented in Table 4.1 and can be compared to the values for bulk diffusion. The effective activation energies E^m_{eff} for pipe diffusion are about 20% (edge) and 5% (screw) lower than the bulk value, while D_0 for both dislocation types is about two orders of magnitude larger.

As the last point of our analysis, although we have obviously focused on the component of carbon trajectories along the dislocation line, it is worthwhile to mention that in our AKMC simulations pipe diffusion was not restricted to the first shell ($R < b$) around the dislocation line: depending on the simulated

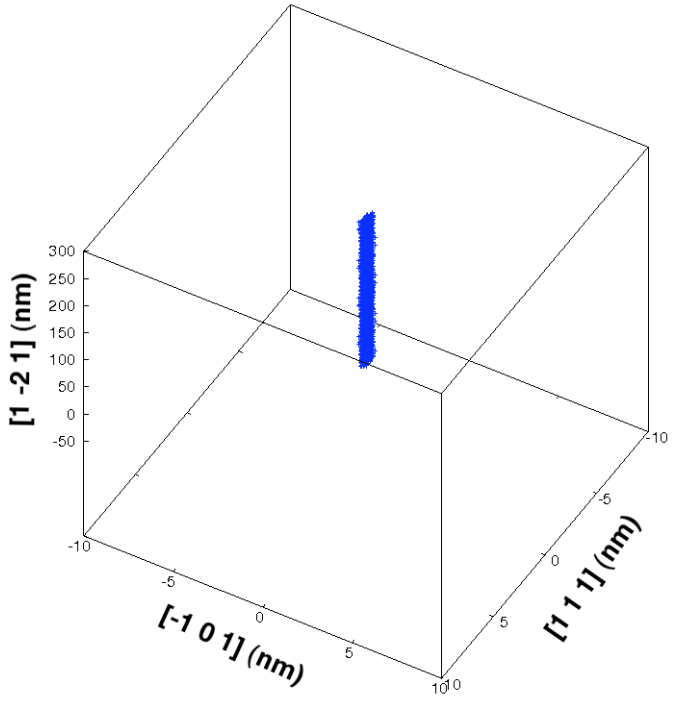

Figure 4.6: Plot of an AKMC-generated carbon trajectory (10,000,000 carbon jumps) at $T = 750$ K in the region defined as the core ($R < 4b \approx 1$ nm) of an edge dislocation. It is straightforward to see that the trajectory is quasi-unidimensional, spreading in the $[1\overline{2}1]$ direction which is parallel to the dislocation line.

	D_0 (m^2/s)	E^m_{eff} (eV)
Bulk	1.3×10^{-7}	0.816
Edge	9.9×10^{-6}	0.670
Screw	1.0×10^{-5}	0.738

Table 4.1: Pre-exponential factor D_0 and effective activation energy E^m_{eff} for carbon diffusion in the bulk and in the core ($R < 4b \approx 1$ nm) of an edge or a screw dislocation.

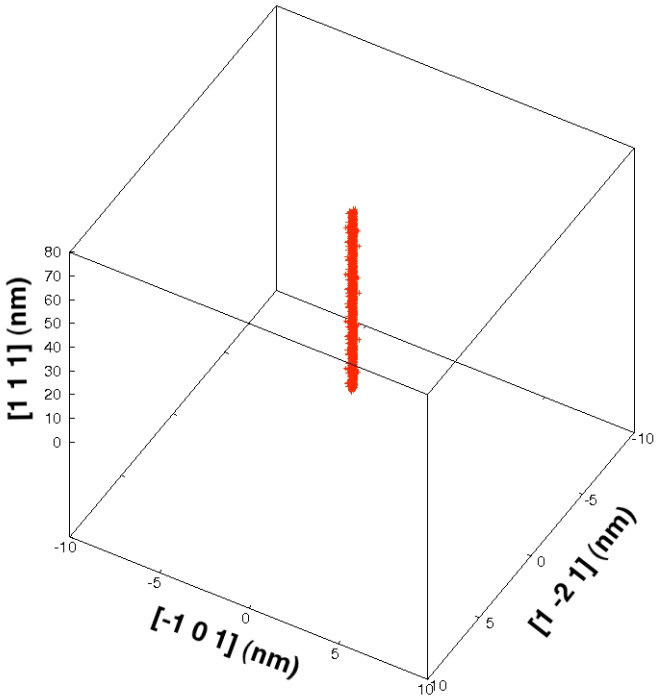

Figure 4.7: Plot of an AKMC-generated carbon trajectory (10,000,000 carbon jumps) at $T = 850$ K in the region defined as the core ($R < 4b \approx 1$ nm) of a screw dislocation. It is straightforward to see that the trajectory is quasi-unidimensional, spreading in the [111] direction which is parallel to the dislocation line.

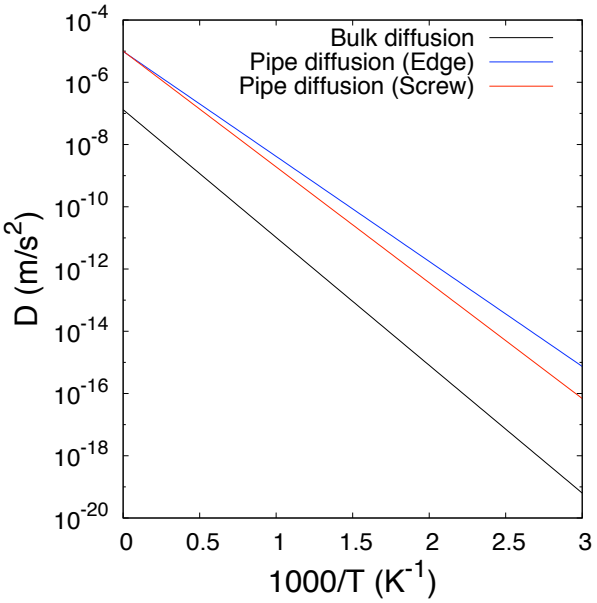

Figure 4.8: Carbon diffusion coefficient in bulk α-iron and in the core ($R < 4b \approx 1$ nm) of an edge or screw dislocation, calculated from AKMC simulations.

temperature, the carbon atom visited positions at $R > 3b$. This is not surprising at all: one should expect that the width of the dislocation pipe increases with temperature, up to the limit where the carbon atom can move away from the line defect. Despite the fact that the host material (aluminium) and the diffusing atom (silicon) in the experimental study reported by Ref. [Legros 2008] are not the same as in this work, our results suggest that the pipe radius may be larger than b, which is the value that Legros and co-workers used in the diffusivity calculation.

It should be mentioned that the analysis of pipe diffusion in the context of this work is hindered, first, by the fact that the current AKMC algorithm is not able to treat the low energy barrier problem properly at low temperatures and, second, by the fact that at high temperatures the carbon-dislocation complex easily dissociates and the carbon atom diffuses back to the bulk. Therefore, the temperature range within which the data for diffusivity presented in Fig. 4.8 was collected was somewhat limited (400–800 K for edge and 750–850 K for screw).

4.3.2 Molecular dynamics simulations

In order to perform an additional check, MD simulations of a single carbon atom in the core of an edge and a screw dislocation have been carried out with LAMMPS using the same simulation boxes as in molecular statics simulations. A time step of 10^{-15} s was used for the integration of the equations of motion. The total simulated time was 11 ns, with 1 ns of equilibration. For both dislocation types, the carbon atom was initially left in the first shell surrounding the dislocation line ($R < b$). For the time being, simulations have been performed at $T = 600$ K (edge and screw) and $T = 800$ K (edge only). In these simulations, the temperature remained constant by means of the coupling to a Nosé-Hoover thermostat [Nosé 1984, Hoover 1985].

A few snapshots of a carbon atom in the core of an edge dislocation at $T = 600$ K can be seen in Fig. 4.9. In this simulation, the carbon atom has been found performing back and forth jumps restricted most of the time to the glide plane of the edge dislocation. Only six jumps to different dislocation segments have been observed during the whole simulated time. The span of the carbon trajectory along the dislocation line (i.e., the difference between the maximum and the minimum z-coordinates of the positions visited by the carbon atom) was 1.6 nm. On the other hand, at $T = 800$ K, pipe diffusion is readily observed. Therefore, our results led to a different conclusion from Tapasa *et al*, which stated that no actual diffusion along the pipe of an edge dislocation was observed in the course

of their MD simulations [Tapasa 2007], even at temperatures as high as 1200 K. It should be mentioned that Ref. [Tapasa 2007] employed a different Fe-C interatomic potential [Johnson 1964].

In Fig. 4.10, one can see three snapshots taken at approximately 1, 4, and 9 ns for a carbon atom in the core of a screw dislocation. These snapshots show the carbon atom occupying the positions that correspond to the sites represented in Fig. 4.4. As it has been previously observed in AKMC simulations, the carbon atom also performs hops at high frequencies within what seems to be a trap. No actual diffusion is seen for the whole simulated time, which one should expect taking into account that the MD-simulated time is much shorter than the AKMC-simulated time at the same temperature. Indeed, according to the AKMC results, pipe diffusion in the core of a screw dislocation, in the typical time scale of MD simulations (ns), is unlikely to be observed at temperatures lower than 750 K.

As a preliminary conclusion, MD simulations revealed the same behavior predicted by AKMC simulations, that is, the carbon atom jumps back and forth in the dislocation core. In the core of a screw dislocation, MD simulations at higher temperatures are necessary to give the carbon atom enough energy to escape the superbasin.

4.4 Analysis of the minimum energy paths in the dislocation core

4.4.1 Carbon in the core of an edge dislocation

Figs. 4.11 to 4.15 show the plots of the minimum energy paths in the core of an edge dislocation that refer to the superbasin seen in Fig. 4.4. The geometries of both energy minima and saddle points are also represented. When the carbon atom lies in an energy minimum, it occupies nearly the center of an irregular (distorted) octahedron. The distance to the surrounding iron atoms falls within the 0.187–0.198 nm range, significantly larger than the carbon-iron distance in an octahedral site in bulk α-iron (0.179 nm). Considering that more space is available, carbon solvation is favored in the core of an edge dislocation and thus carbon-dislocation binding energies are the largest (ranging from 0.61 eV to 0.65 eV), in agreement with previous simulations carried out with our Fe-C potential [Clouet 2008]. The lowest energy barriers (0.33 eV) are observed for the transitions depicted in Figs. 4.12 and 4.14. At the saddle point, the carbon atom is found in the center of a distorted tetrahedron, that is, these transitions are sim-

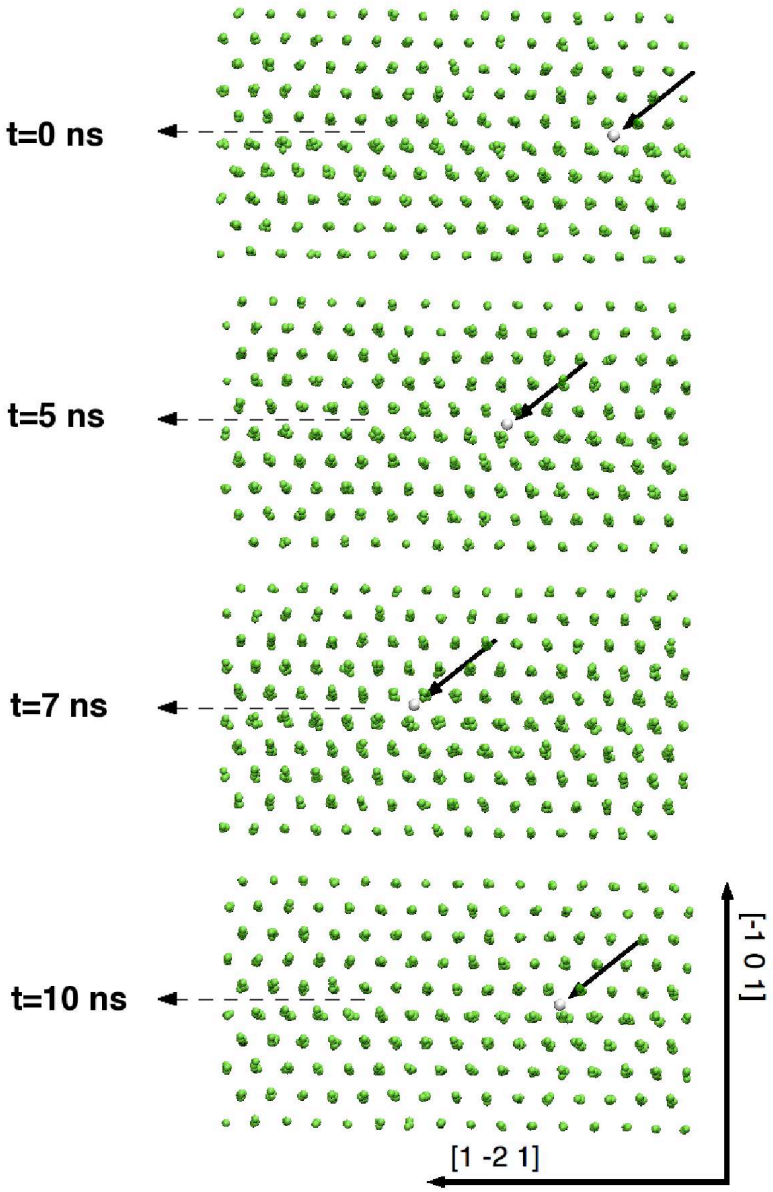

Figure 4.9: Snapshots of molecular dynamics simulations at $T = 600$ K for a carbon atom (white ball) in the core ($R < 4b \approx 1$ nm) of an edge dislocation. The solid arrows point to the carbon atom, whereas the dashed arrows show the position and orientation of the dislocation line.

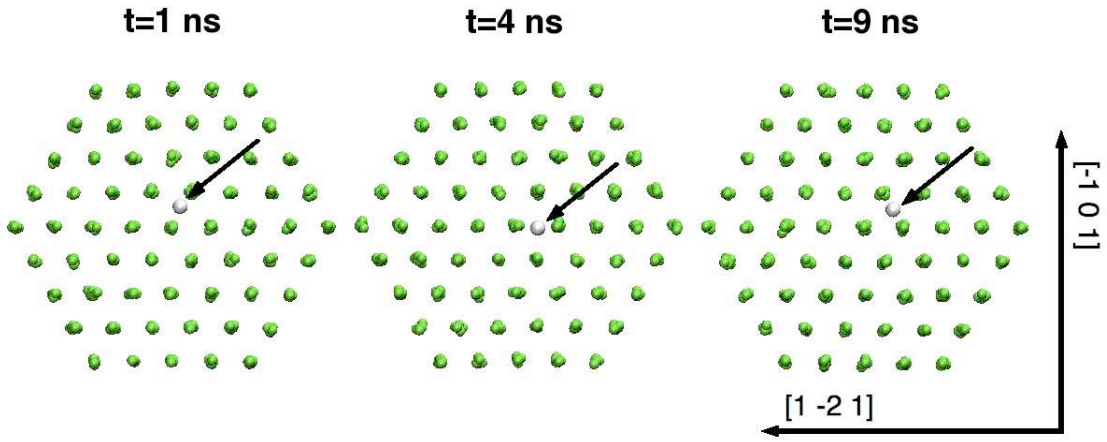

Figure 4.10: Snapshots of molecular dynamics simulations at $T = 600$ K for a carbon atom (white ball) in the core ($R < 4b \approx 1$ nm) of a screw dislocation. The solid arrows point to the carbon atom. The dislocation line (in the center) is perpendicular to the plane of the page.

ilar to the typical octahedral-to-octahedral transitions in non-strained bcc iron. For the transitions shown in Fig. 4.14, in turn, the tetrahedral site is rather a shallow energy minimum in the middle of the path. There are two equivalent saddle points in this path, where the carbon atom lies near the face of a tetrahedron, which corresponds to the center of a distorted triangular prism. The carbon atom can enter/leave the superbasin by overcoming the barriers shown in Figs. 4.11 and 4.15. In these plots, **A** and **B** are the energy minima connected to the two extremities of the superbasin. One can see that the picture is quite similar to what is seen in Fig. 4.14, except that the two peaks are no longer equivalent (the highest peak yields a barrier of 0.55 eV to escape the superbasin).

Clouet *et al* have reported that at short carbon-dislocation separations ($R \approx 3b$) our interatomic potential predicts that the force on the dislocation due to the carbon atom is so strong that makes the line defect leave its initial position and move towards the solute [Clouet 2008]. Tapasa *et al*, in turn, have found in their simulations, performed with the Fe-C potential developed by Johnson *et al* [Johnson 1964], that carbon jumps in the core of an edge dislocation are accompanied by dislocation jumps [Tapasa 2007]. Thus it is worthwhile to check also the behavior of the dislocation line in our simulations as the carbon atom performs jumps from/to the sites in the superbasin and out of it. It should be stressed that when the carbon atom jumps along the pipe, it does not move parallel to the dislocation line. Its trajectory rather makes an angle of about

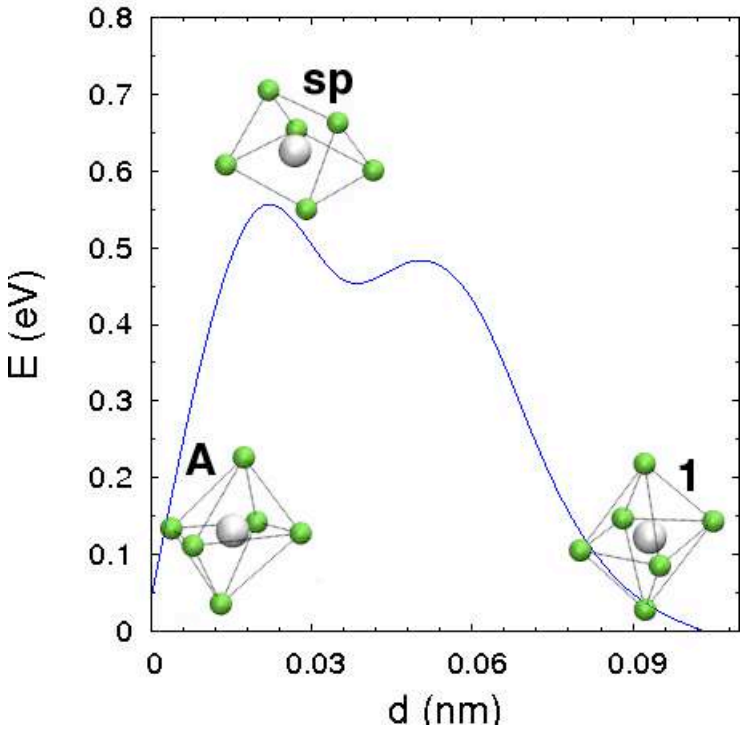

Figure 4.11: Minimum energy path connecting a state outside the superbasin with the state 1 in a superbasin in the core ($R < 4b \approx 1$ nm) of an edge dislocation, depicted in Fig. 4.4. The carbon atom is represented by a big white ball and the iron atoms by small green balls. The geometries are oriented so as to make visualization easier.

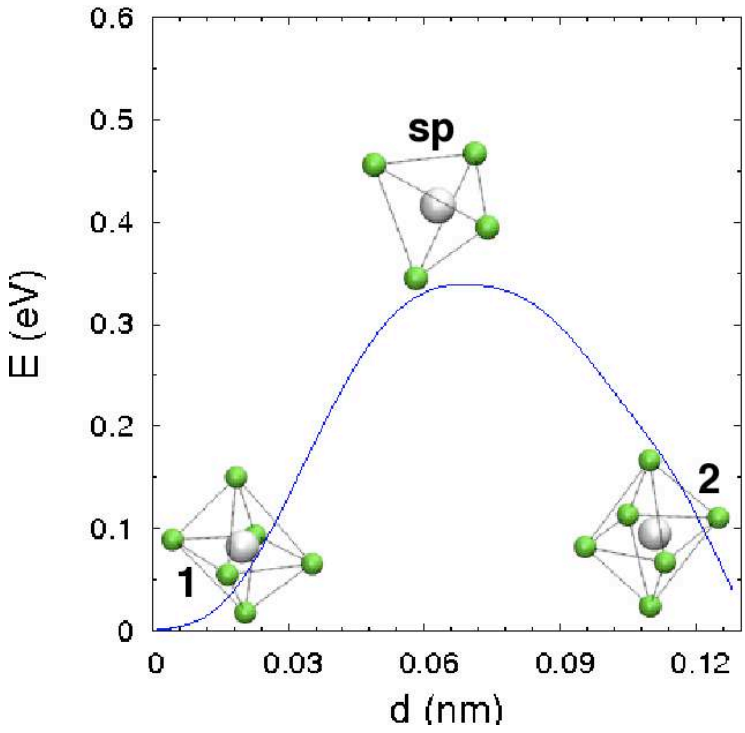

Figure 4.12: Minimum energy path connecting the state 1 to the state 2 in a superbasin in the core ($R < 4b \approx 1$ nm) of an edge dislocation, depicted in Fig. 4.4. The carbon atom is represented by a big white ball and the iron atoms by small green balls. The geometries are oriented so as to make visualization easier.

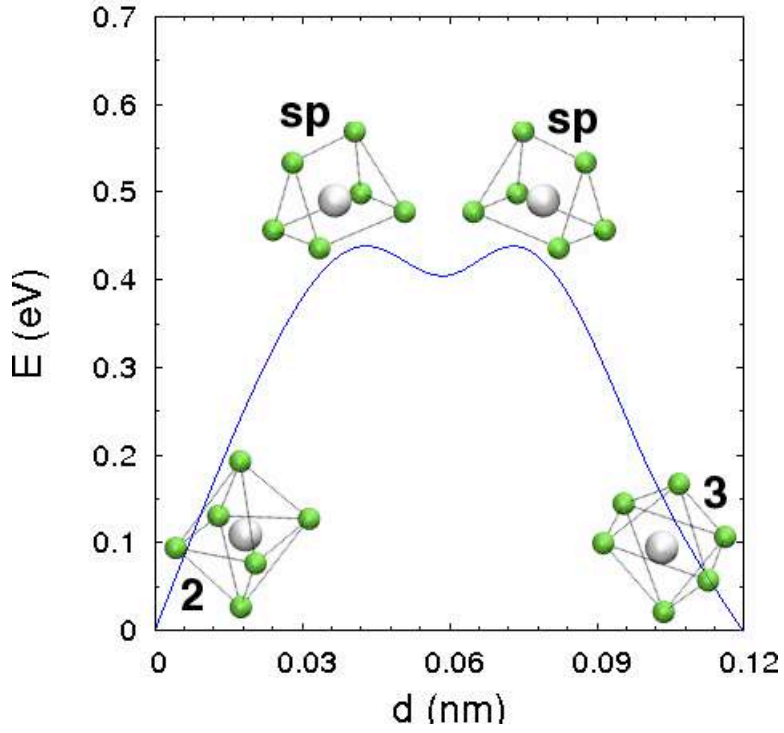

Figure 4.13: Minimum energy path connecting the state 2 to the state 3 in a superbasin in the core ($R < 4b \approx 1$ nm) of an edge dislocation, depicted in Fig. 4.4. The carbon atom is represented by a big white ball and the iron atoms by small green balls. The geometries are oriented so as to make visualization easier.

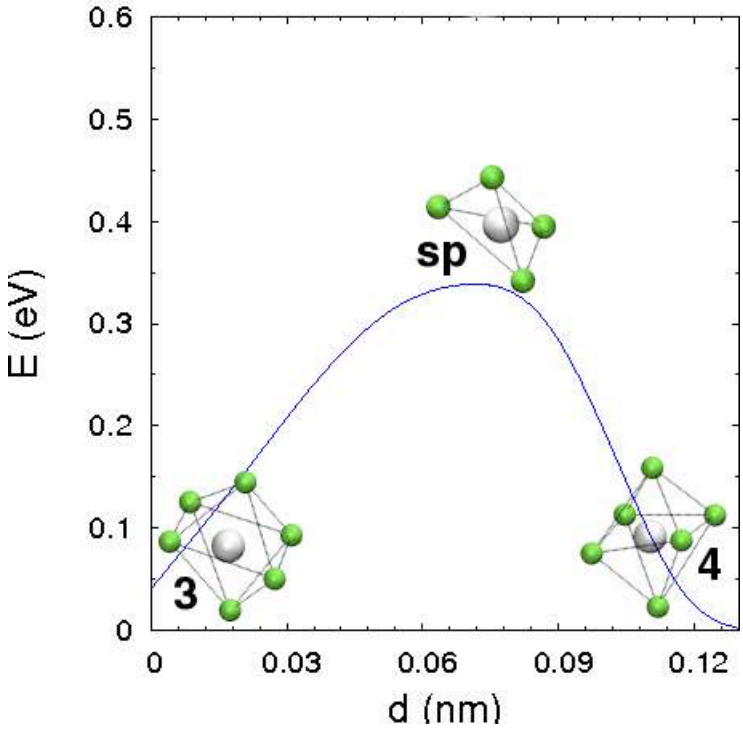

Figure 4.14: Minimum energy path connecting the state 3 to the state 4 in a superbasin in the core ($R < 4b \approx 1$ nm) of an edge dislocation, depicted in Fig. 4.4. The carbon atom is represented by a big white ball and the iron atoms by small green balls. The geometries are oriented so as to make visualization easier.

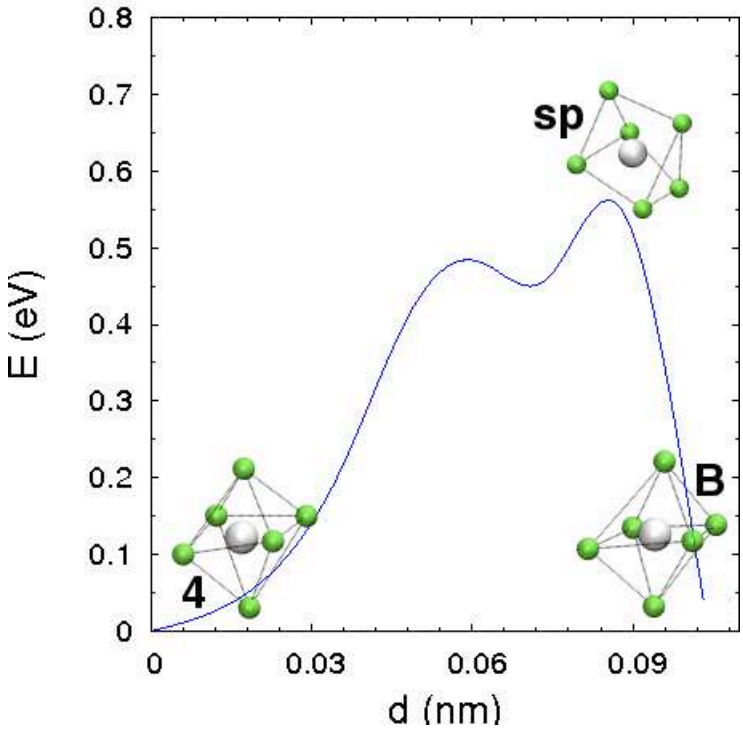

Figure 4.15: Minimum energy path connecting the state 4 in a superbasin in the core ($R < 4b \approx 1$ nm) of an edge dislocation, depicted in Fig. 4.4, with a state outside the superbasin. The carbon atom is represented by a big white ball and the iron atoms by small green balls. The geometries are oriented so as to make visualization easier.

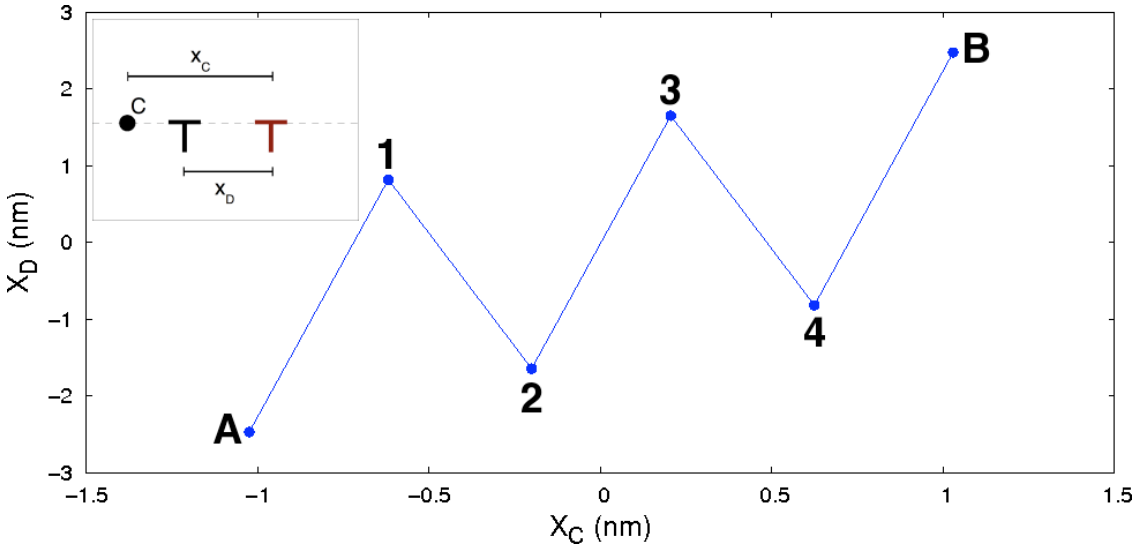

Figure 4.16: Dislocation line position (X_D) as a function of carbon position (X_C) in the region defined as the core ($R < 4b \approx 1$ nm) of an edge dislocation. The reference is the initial position of the dislocation line (in red in the inset).

70° with the Burgers vector direction, as one can see in Fig. 4.4. In other words, as the carbon atom jumps along the dislocation pipe, it also moves along the glide plane.The position of the dislocation line (X_D) as a function of carbon position in the glide plane of the edge dislocation (X_C) can be seen in Fig. 4.16. The reference is the initial position of the dislocation line. One can see that, as the carbon atom jumps in the glide plane, the dislocation line itself is displaced from its initial position and follows the interstitial atom. However, as the dislocation moves, its strain field is also expected to move. In this case, the fixed boundaries of the cylindrical simulation box used in molecular statics and molecular dynamics simulations, which represent the strain field of an edge dislocation in its initial position, imposes a resistance to dislocation motion. Such a resistance is reflected in the higher energy barriers shown in Figs. 4.11 and 4.15, which corresponds to the dislocation line moving more than b away from its initial position.

4.4.2 Carbon in the core of a screw dislocation

A few superbasins were identified in the core of a screw dislocation. One of them is shown in Fig. 4.4. The positions that a carbon atom can occupy are in the vertices of a triangle. Other superbasins identified near the line of the screw dislocation present the same configuration. Figs. 4.17 to 4.19 represent the minimum energy paths with the geometries corresponding to the energy minima and the saddle points for the fast transitions within the superbasin as well as

the lowest energy transition to move the system out of it (site **A** in Fig. 4.4). One can see that the jump distances within the superbasin ($\approx$ 0.12 nm) are much shorter than the jump distance from state 1 to the state **A** ($\approx$ 0.17 nm). Regarding the geometry, the carbon atom is nearly the center of a distorted octahedron in states 1 and 2, and also in state **A**. These states are energetically equivalent, i.e., they have the same carbon-dislocation binding energy ($E^b = 0.41$ eV). Distances to the closest iron atoms lie in the 0.184–0.198 nm range. The geometry of state 3, in turn, is not the same as the other states, as one can see in Fig. 4.19. This state is about 50 meV higher in energy than states 1 and 2. At the saddle point between the state **A** and the state 1, the carbon atom occupies nearly the center of a distorted tetrahedron. Therefore, such a transition resembles the typical octahedral-to-octahedral transition in bcc iron. On the other hand, at the saddle points within the superbasin, the carbon atom is found nearly the center of a distorted triangular prism. The consequence of the geometrical differences, particularly evident for the saddle points, is that the energy barriers for jumps inside the superbasin (0.20–0.24 eV) are much lower than the lowest energy barrier to jump out of it (0.81 eV, which is close to the value for carbon diffusion in non-strained bcc iron). Consequently, particularly at low temperatures, the probability to escape the superbasin is very low.

4.5 Overview

This chapter presented atomistic simulations of carbon behavior in the core of an edge and a screw dislocation in α-Fe. The energy barriers in the core region (defined *ad hoc* as a cylinder of radius $4b$ surrounding the dislocation line) of both dislocation types have been obtained by the CI-NEB method as implemented in LAMMPS. AKMC simulations fed with these energy barriers were performed for a wide temperature range (300–900 K). Actual pipe diffusion was observed only at $T \geq 400$ K (edge) and $T \geq 750$ K (screw). Below these temperatures, the carbon atom was seen to jump back and forth within a short circuit made of states separated by low energy barriers. The same behavior was confirmed by MD simulations carried out with LAMMPS. Additional AKMC simulations, which generated long carbon trajectories (up to 10,000,000 steps), allowed us to calculate, from the slope of the mean squared displacement at large t, the effective diffusion coefficients for carbon migration in the core of an edge and a screw dislocation. These diffusion coefficients are about two orders of magnitude larger than the diffusion coefficient for carbon migration in the bulk. Finally, the

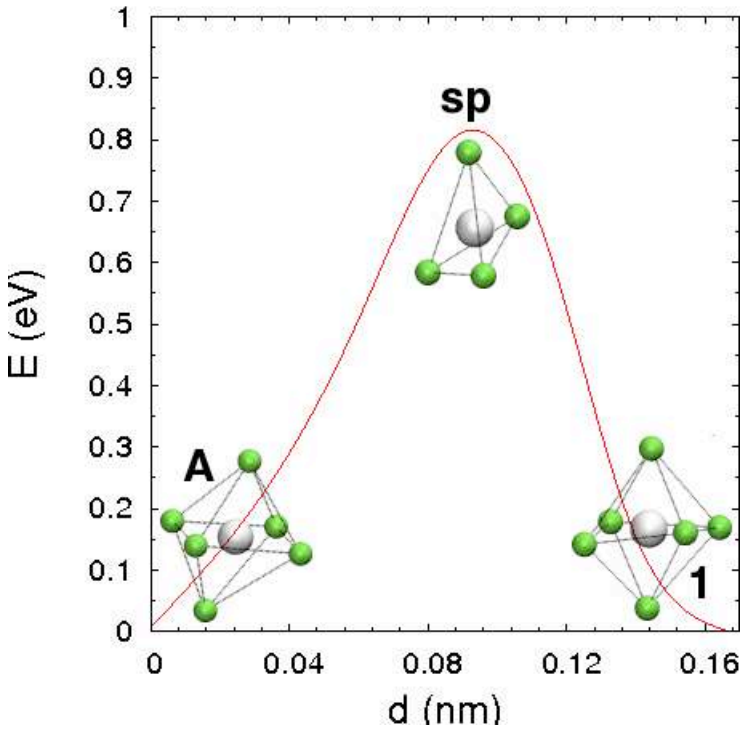

Figure 4.17: Minimum energy path connecting a state outside the superbasin with the state 1 in a superbasin in the core ($R < 4b \approx 1$ nm) of a screw dislocation, depicted in Fig. 4.4. The carbon atom is represented by a big white ball and the iron atoms by small green balls. The geometries are oriented so as to make visualization easier.

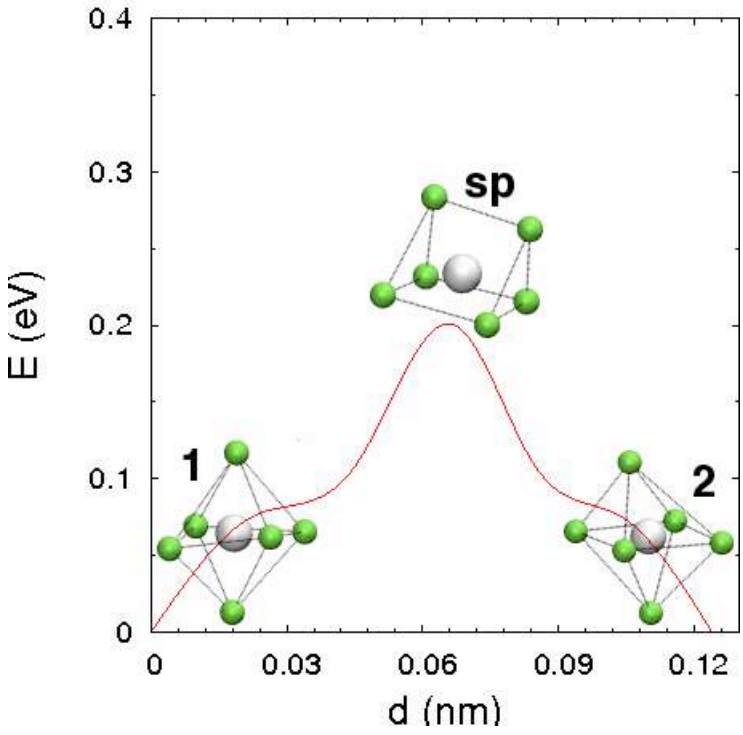

Figure 4.18: Minimum energy path connecting the state 1 to the state 2 in a superbasin in the core ($R < 4b \approx 1$ nm) of a screw dislocation, depicted in Fig. 4.4. The carbon atom is represented by a big white ball and the iron atoms by small green balls. The geometries are oriented so as to make visualization easier.

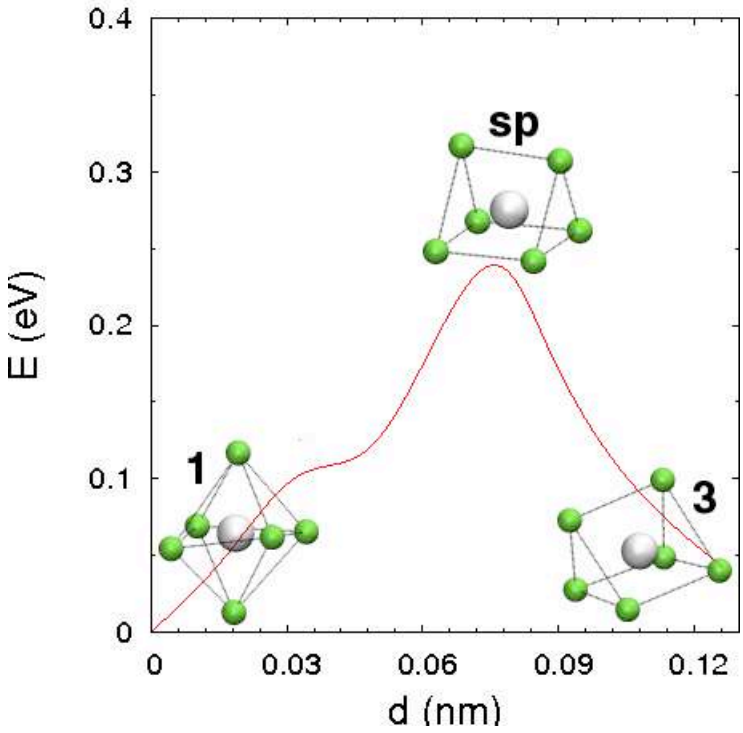

Figure 4.19: Minimum energy path connecting the state 1 to the state 3 in a superbasin in the core ($R < 4b \approx 1$ nm) of a screw dislocation, depicted in Fig. 4.4. The carbon atom is represented by a big white ball and the iron atoms by small green balls. The geometries are oriented so as to make visualization easier.

effective energy barrier in the dislocation cores was calculated: 0.670 (edge) and 0.738 (screw), about 20% and 5% lower than the energy barrier in the bulk (0.816 eV), respectively.

4.6 Ongoing work

Considering the results of the AKMC simulations presented in this chapter, Algorithm 1.1 does not seem to be appropriate for the simulation of pipe diffusion in bcc iron at low temperatures. The low barrier problem, which consists of two or more states separated by energy barriers much lower than the energy barriers to escape to other states, is a long standing problem in AKMC simulations. To circumvent it, it is necessary to modify the AKMC algorithm such that the fast transitions in a superbasin, which do not contribute to diffusion, are handled separate from the slow transitions, as proposed by Ref. [Puchala 2009]. The implementation of these modifications into the AKMC algorithm is left as future work.

Chapter 5

Carbon distribution in the stress field of a dislocation

Abstract

The vicinity of a dislocation can be divided into binding and anti-binding zones, where the probability to find a carbon atom is higher or lower than in the matrix, respectively. These zones overlap in regions where the shear stress predominates (i.e., all around a screw dislocation and near the glide plane of an edge dislocation). Statistical physics was used with the carbon-dislocation binding energies obtained by atomistic simulations to calculate the concentration of carbon atoms around an edge or a screw dislocation. The saturation concentration in the dislocation core was estimated and taken as an upper limit in the carbon distributions. A good agreement between theoretical predictions and the available experimental atom probe data is also demonstrated.

5.1 Introduction

In Chapter 2, we presented the simulations of the kinetics of carbon diffusion to an edge or a screw dislocation under the condition of very low carbon concentration, which implies that all arriving carbon atoms are captured within the dislocation core. We have also seen that at least the earliest stages of Cottrell atmosphere formation should be driven only by the bias on carbon diffusion induced by the presence of the line defect. However, as carbon concentration increases, the dislocation core is not able to accommodate all segregating interstitials and the atmosphere grows up outwards from the dislocation core by occupying sites in the surrounding matrix. Moreover, the relaxation of the dislocation strain field due to the growing interstitial cloud is likely to change the way the line defect affects carbon diffusion. In other words, simulating the dynamics of many carbon atoms in a Cottrell atmosphere is obviously a task much more complex than following the trajectories of isolated carbon atoms that interact only with the strain field of a fresh dislocation. For the time being, we focused on obtaining a static distribution of carbon atoms around an edge or a screw dislocation, which is interesting in its own right and can be achieved with the knowledge of the carbon-dislocation binding energies already calculated from molecular statics simulations.

In the next section of this chapter, some experimental results on carbon segregation to dislocations in iron [Wilde 2000, Miller 2003, Miller 2006], obtained by atom probe, are summarized. Apart from the experimental demonstration of the existence of Cottrell atmospheres, atom probe also provides information on the composition, solute concentration, and shape of the atmospheres. The subsequent section presents the statistical physics approach that we have used to obtain the equilibrium distribution of carbon atoms around an edge and a screw dislocation. A static model of a Cottrell atmosphere in equilibrium generated by such an approach can be seen in the third section. Finally, in the last section, theoretical results are compared to the experimental atom probe data.

5.2 Atomic scale experimental characterization of solute segregation to dislocations

The segregation of solute atoms to dislocations is among the most difficult microstructural features to be characterized in experiments, owing to the small extent of Cottrell atmospheres and the low dislocation densities. Despite these

difficulties, three-dimensional atom probe (3DAP) techniques have allowed to successfully image Cottrell atmospheres, even if not routinely. Chang demonstrated carbon segregation to dislocations in low carbon lath martensites by superimposing field ion micrographs and gated carbon images taken in the imaging atom probe [Chang 1985]. Indeed, Chang's doctoral thesis, defended in 1985 at Oxford University, provides, to our knowledge, the first direct observation of a carbon Cottrell atmosphere in iron, about 35 years after the pioneering Cottrell and Bilby's work. However, due to the limitations of the experimental apparatus, Chang's work was not fully quantitative: not all carbon atoms were detected and carbon concentration with respect to iron could not be properly recorded.

Wilde and co-authors later extended Chang's work and mapped a 3D distribution of carbon atoms around a dislocation with energy-compensated optical position sensitive atom probe (ECOPoSAP) in conjunction with field ion microscopy (FIM) [Wilde 2000]. Such a mapping for a Fe-0.85at%C (low carbon) martensite specimen aged at room temperature for over 24 hours can be seen in Fig. 5.1 and also compared to a dislocation free region of same size (width of 10 ± 1.5 nm). Solute enhancement in the vicinity of the line defect is clearly demonstrated. The carbon atoms form a disperse cloud that extends about 7 nm outwards from the dislocation core. A maximum carbon concentration of approximately 8 at% was observed, with about 21 carbon atoms per atomic plane along the dislocation line. This corresponds to 105 carbon atoms per nanometer of dislocation. The shape of the solute enhanced region depicted in Fig. 5.2, which shows three lobes separated by 120°, has led authors of Ref. [Wilde 2000] to conclude that it was likely to be a screw dislocation, which is also the dislocation type most commonly found in lath martensites [Sandvik 1983]. However, as Wilde and co-workers recognized, it is not a trivial task to characterize the dislocation type in FIM and, as it has been pointed out by Miller [Miller 2006], except in a few special cases where the closure failure of the Burgers circuit is visible in the atom maps (for instance, in Ref. [Blavette 1999]), it is not normally possible to distinguish neither the dislocation type nor the precise location of the dislocation line from the atom probe data. Moreover, even in these special cases, the applied electric field imposes a mechanical stress on the specimen that may alter the precise relationship of the dislocation to the atmosphere.

Refs. [Miller 2003, Miller 2006], in turn, presented a three-dimensional atom probe (3DAP) tomography characterization of a mechanically-alloyed, oxide-dispersion-strengthened (MA/ODS) ferritic alloy. The composition of the specimen can be seen in Table 5.1. Enhanced zones around dislocations were defined

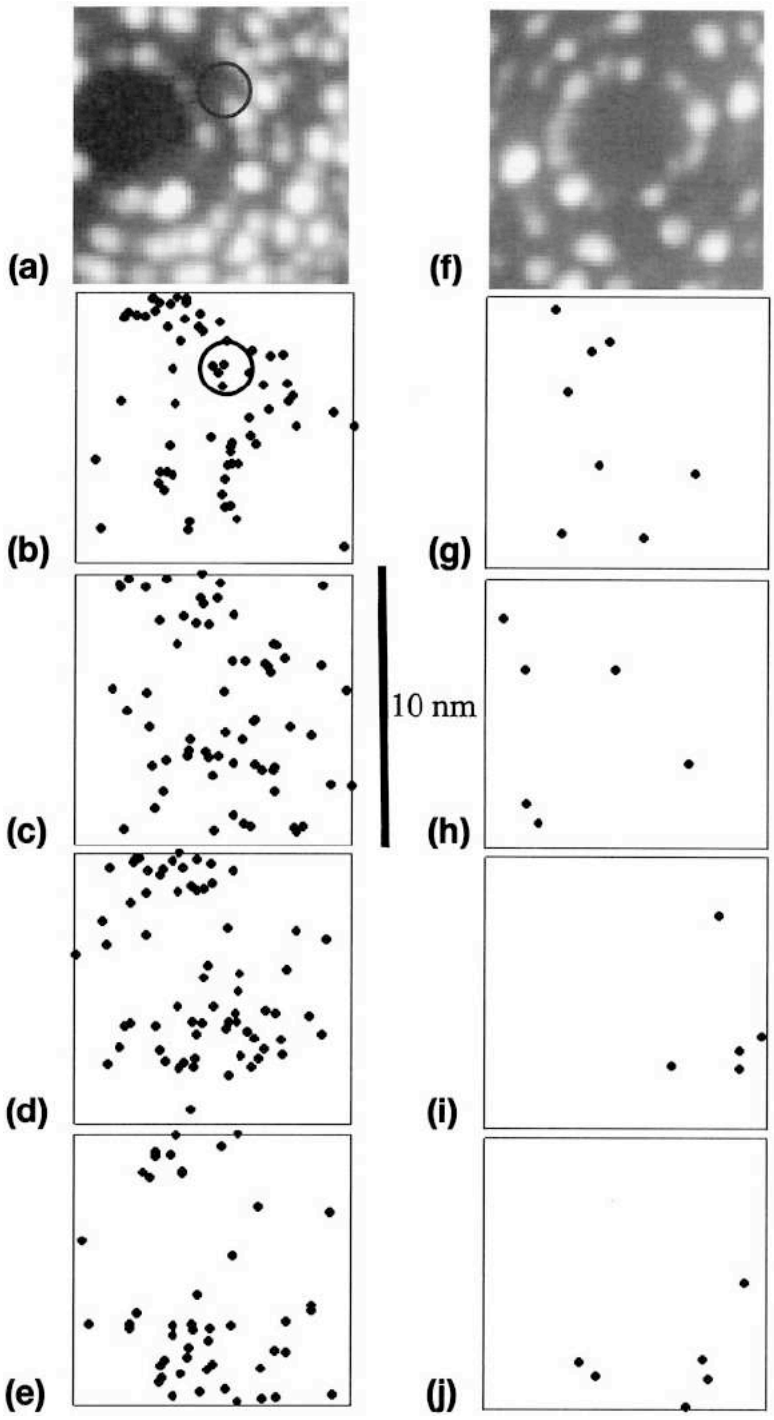

Figure 5.1: Results of ECOPoSAP analysis carried out directly over a dislocation (a-e) and over a dislocation free region (f-j) in a Fe-0.85at%C martensite specimen. Field ion micrographs of the areas of analysis, (a) and (f), were taken at 12 kV in Ne at $T = 50$ K. The analyzed volumes are divided into four successive sections of width 10 ± 1.5 nm, (b-e) and (g-j) respectively, each containing exactly five atomic planes. The initial position of the dislocation is shown by the dark circles in (a) and (b). Figure taken from Ref. [Wilde 2000].

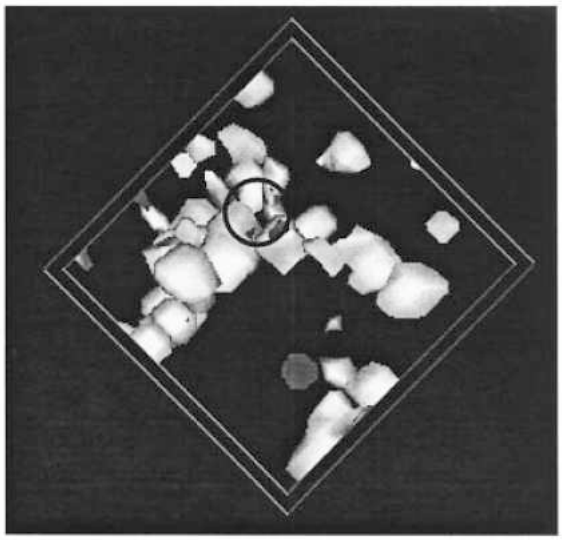

Figure 5.2: Top view plot (4at%C isosurfaces) of a Cottrell atmosphere obtained by ECOPoSAP. The dislocation position is marked by a circle. The width of the analyzed region is 10 ± 1.5 nm and the depth is ≈ 4 nm. Figure adapted from Ref. [Wilde 2000].

according to the envelope method described in details in Ref. [Marquis 2010]. Shortly, this method is implemented by identifying the solute atoms in the feature of interest (e.g., a precipitate particle or the vicinity of a dislocation) and then superimposing a fine 3D grid over the data. In order to identify such atoms, a distance criterion is employed: two atoms separated by a distance d below a certain value d_{max} (typically ranging from 0.4 nm to 0.6 nm) are considered to be part of an enriched zone; otherwise, they are considered as atoms in solution in the host matrix. A grid size of 0.1–0.2 nm is usually chosen. The extent of the feature is defined by the grid cells that contain solute atoms separated by $d \leq d_{max}$ and also by the grid cells that, even eventually empty, are encompassed by the enriched ones. From Table 5.1, it is straightforward to verify that the concentration of all alloying elements increased in the vicinity of the line defect, although for some of them (for instance, nitrogen) the enhancement is almost negligible. Carbon concentration has been seen to be enhanced by a factor of 7.7.

5.3 Modeling approach

5.3.1 Statistical physics

The problem of finding the average distribution of solute atoms in a Cottrell atmosphere under the condition of thermodynamic equilibrium has been ad-

Element	Matrix at.%	Dislocation at.%	Enrichment
Cr	12.3	15.9±0.16	1.3
W	0.71	1.21±0.05	1.7
Ti	0.08	0.44±0.03	5.5
Y	0.01	0.16±0.02	16.0
O	0.11	0.53±0.03	4.8
C	0.18	1.38±0.05	7.7
B	0.05	0.44±0.03	8.8
N	0.15	0.17±0.02	1.1

Table 5.1: Solute concentration in the matrix of a MA/ODS alloy obtained by atom probe tomography. The balance is iron. Taken from Ref. [Miller 2003].

dressed since such atmospheres were firstly proposed as an explanation of the SSA phenomenon [Cottrell 1949]. For this purpose, Cottrell and Bilby employed the Maxwell-Boltzmann formula around an edge dislocation:

$$\frac{n_i}{n_0} = \exp\left(\frac{E_i^b}{kT}\right) \tag{5.1}$$

In Eq. (5.1), n_i is the number of solute atoms occupying sites with solute-dislocation binding energy E_i^b and n_0 is the background (matrix) solute concentration. Cottrell and Bilby verified that this distribution holds for dilute carbon concentrations in the far-field, where E_i^b is small. However, it fails near the dislocation core ($R < 1$ nm), where E_i^b assumes the largest values. In this region and at room temperature, Maxwell-Botzmann statistics yields impossibly large values (in the order of 10^{11}) of the ratio n_i/n_0. For example, if N_i is the number of sites with energy E_i^b and n_i is the number of occupied sites, it is obvious that n_i must be smaller than N_i, whatever the energy level E_i^b.

In an attempt to provide a more reasonable distribution, taking into account this saturation effect, Louat proposed the following equation [Louat 1956]:

$$\frac{n_i}{n_0} = \frac{N_i - n_i}{N_0 - n_0} \exp\left(\frac{E_i^b - E_0^b}{kT}\right) \tag{5.2}$$

where N_0 and n_0 are the total number of sites and number of occupied sites, respectively, of a reference state of energy E_0^b. Louat's derivation was based on the following assumptions:

i. the region near a dislocation may be divided into a number of discrete sub-regions characterized by a unique solute-dislocation binding energy;

ii. each sub-region can be occupied by only one solute atom at a time;

iii. the interaction between solute atoms in the atmosphere may be neglected.

An important remark made by Beshers is that these assumptions are the same as the ones on which Fermi-Dirac statistics are based, that is, the problem here also boils down to how to distribute indistinguishable particles with negligible mutual interaction in discrete states with a maximum occupancy of one particle per state [Beshers 1958].

Eq. (5.2) can be readily rearranged as follows:

$$\frac{n_i}{N_i - n_i} = \frac{n_0}{N_0 - n_0} \exp\left(\frac{E_i^b - E_0^b}{kT}\right) \tag{5.3}$$

There is a large degeneracy in energy, with the total number of sites with a given energy being as great as the number of these sites per dislocation unit length multiplied by the total dislocation length. It is thus more convenient if we express Eq. (5.3) in terms of the fractional occupancies $\overline{n}_i = n_i/N_i$ and $\overline{n}_0 = n_0/N_0$:

$$\frac{\overline{n}_i}{1 - \overline{n}_i} = \frac{\overline{n}_0}{1 - \overline{n}_0} \exp\left(\frac{E_i^b - E_0^b}{kT}\right) \tag{5.4}$$

If we take E_0^b as the carbon-dislocation binding energy for a carbon atom very far away from the dislocation, $E_0^b \to 0$ because the interaction between both defects is negligible. Then, rearranging the terms of Eq. (5.4) finally yields:

$$\overline{n}_i = \frac{\frac{\overline{n}_0}{1 - \overline{n}_0} \exp\left(\frac{E_i^b}{kT}\right)}{1 + \frac{\overline{n}_0}{1 - \overline{n}_0} \exp\left(\frac{E_i^b}{kT}\right)} \tag{5.5}$$

In this case, $\overline{n}_0$ should be seen as the fractional occupancy of an octahedral site in non-strained α-Fe and $\overline{n}_i$ is the fractional occupancy of a site corresponding to an energy minimum in the neighborhood of a dislocation where the carbon atom interacts with the line defect with a binding energy E_i^b. Taking into account that $0 < \overline{n}_i < 1$, $\overline{n}_i$ is also the probability to find a carbon atom at this site at a given temperature.

5.3.2 Saturation concentration

Even if Louat's formulation (i.e., Fermi-Dirac statistics) for solute distribution in a Cottrell atmosphere yields better results than Maxwell-Boltzmann statistics, it still fails in the vicinity of the dislocation core. As pointed out by Beshers

[Beshers 1958], in the first shell around a dislocation ($R < b$), where the largest carbon-dislocation binding energies are found, Fermi-Dirac statistics gives an occupancy probability $\overline{n}_i$ larger than 99% at room temperature. This implies three or four times more carbon atoms than iron atoms in that region, an interesting feature that was never observed experimentally. It is straightforward to deduce that the reason behind this result is that the third assumption on which Louat based the derivation of Eq. (5.2) is not valid when the atmosphere becomes too dense. Indeed, at a certain concentration level, carbon atoms do interact with each other when dissolved in the iron matrix, as one can see, for instance, in Ref. [Sinclair 2010], where ordering of carbon in supersaturated α-iron has been simulated by molecular dynamics. Depending on their relative positions in the iron matrix, two neighboring carbon atoms can attract or repel each other with binding energies of up to 1.50 eV or -1.67 eV, respectively, according to *ab initio* calculations [Becquart 2007].

In the following lines, we present a scheme to estimate the saturation concentration in a given volume (a cylinder of radius b around the dislocation line) that employs an iterative algorithm (Algorithm 5.1) and molecular statics simulations with the interatomic Fe-C potential used throughout this work. It is based on an assumption similar to Cochardt's one [Cochardt 1955]: the saturation concentration is achieved when an additional carbon atom is no longer able to reduce the energy of the Fe-C system. To perform the simulations, a list of minimum energy positions that a carbon atom can occupy inside a cylindrical volume of radius b containing an edge or a screw dislocation was built. The largest carbon-dislocation binding energies are found in this volume, as shown in Chapter 4. At every iteration of the algorithm, one of these positions not yet occupied by a carbon atom is chosen at random and a carbon atom is inserted in the corresponding position in the simulation box employed in molecular statics simulations. Then, conjugate gradient is carried out with LAMMPS to obtain the total energy of the new configuration. Once knowing the total energy, the variation of the energy of the Fe-C system when m carbon atoms are found in the volume of interest is defined as follows:

$$\Delta E_{mC} = mE_C + E_{dislo} - E_{mC+dislo} \tag{5.6}$$

In Eq. (5.6), $E_C = -10.059$ eV, as already seen in Chapter 2, is the energy added by an isolated carbon atom occupying a minimum energy position in α-iron (i.e., an octahedral site) according to the EAM potential, E_{dislo} is the total energy of a simulation box such as the ones depicted in Fig. 2.4, and $E_{mC+dislo}$ is the total energy of the same simulation box with m carbon atoms. If $\Delta E_{mC} > \Delta E_{(m-1)C}$

then the configuration is accepted and the site that refers to the last added carbon atom is considered occupied. Otherwise, the configuration is rejected and the number of rejected configurations is incremented by one. The simulation stops if a user-defined consecutive number of configurations is rejected (i.e., we assume that saturation concentration has been achieved). In Algorithm 5.1, reverse moves (occupied → unoccupied) are not allowed, that is, a carbon atom can only be added to an empty site, but not removed from it in subsequent moves.

Algorithm 5.1 Algorithm used to estimate the saturation concentration in the first shell ($R < b \approx 0.25$ nm) surrounding a dislocation. For the time being, reverse moves (occupied → unoccupied) are not allowed.

```
Parameter: maximum number of simulations N_sim;
Parameter: maximum number of consecutive rejected configurations N_rej;
Load the list of interstitial sites;
i = 1;
while i ≤ N_sim do
  Create an empty history file;
  Create an empty list of blocked sites;
  m = 0;
  ΔE_mC = 0;
  j = 0;
  while j ≤ N_rej do
    Select a non-blocked site at random in the list of interstitial sites and
    Add a carbon atom to the corresponding position in the molecular statics
    simulation box;
    Run LAMMPS to obtain the total energies of the new configuration;
    m = m + 1;
    Compute ΔE_mC (Eq. 5.6);
    if ΔE_mC > ΔE_(m−1)C then
      Accept the new configuration;
      Add the current site to the list of blocked sites;
      Save m, the current site index, and Δ_mC into the history file;
      j = 0;
    else
      Reject the new configuration;
      m = m − 1;
      j = j + 1;
    end if
  end while
  i = i + 1;
end while
```

As illustrated in Fig. 5.3, the carbon concentrations around dislocations presented in the next section are calculated by Eq. (5.5), with the additional con-

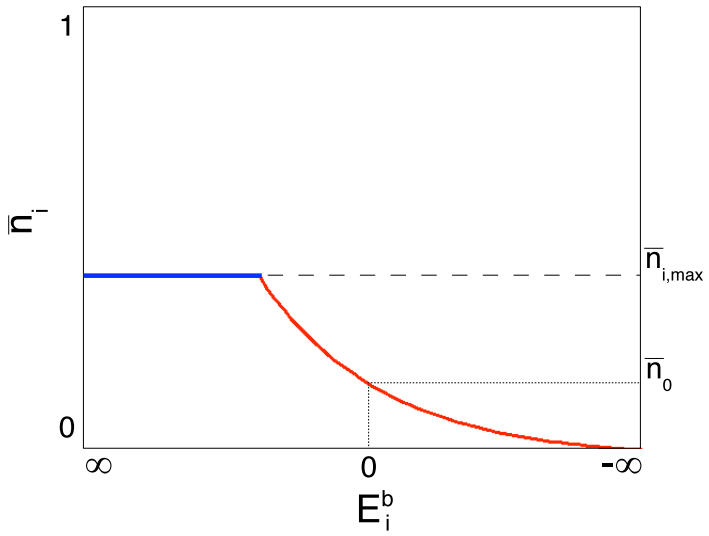

Figure 5.3: Graphical description of the approach used in this chapter to model carbon distribution in a Cottrell atmosphere: the occupancy $\overline{n}_i$ is calculated by Eq. (5.5) as a function of the carbon-dislocation binding energy E_i^b. If $\overline{n}_i > \overline{n}_{i,max}$, calculated by the Algorithm 5.1, we take $\overline{n}_i = \overline{n}_{i,max}$.

dition that $\overline{n}_i$ is smaller than the maximum occupancy $n_{i,max}$ obtained by Algorithm 5.1:

$$\overline{n}_i = \min\left(n_{i,max}, \overline{n}_{i,\text{Eq. (5.5)}}\right) \tag{5.7}$$

5.4 Modeling carbon distribution in the neighborhood of dislocations

5.4.1 Extent and shape of a Cottrell atmosphere

Given the low solubility of carbon in α-iron, a carbon Cottrell atmosphere, except very near the dislocation core, still is expected to be very dilute. Indeed, experimental findings suggest that much of the atmosphere is distributed up to a few nanometers away from the dislocation core [Wilde 2000, Miller 2003, Miller 2006]. A question that can arise is: how far from the dislocation line a carbon atom still can be considered bound to it? One answer to this question, based on the binding energies between both defects, has been proposed by Ref. [Cochardt 1955]: a Cottrell atmosphere should extend up to the limit in which the carbon-dislocation binding energy E^b is larger than the thermal energy kT. Beyond it, the disloca-

tion influence on the carbon atom is no longer relevant, since thermal fluctuations are strong enough to take the interstitial away. On the other hand, if $E^b < -kT$, we have the contrary: the available thermal energy is not sufficient to take the carbon atom closer to the line defect. Therefore, sites with $E^b > kT$ are "binding sites" (carbon is more likely to occupy one of these sites than a site in the non-strained iron matrix) and sites with $E^b < -kT$ are "anti-binding sites" (one should not expect to find a carbon atom there).

Fig. 5.4 presents the extent and shape of the regions containing the binding and anti-binding sites for a carbon atom near an edge or a screw dislocation. The binding energies E^b for a carbon atom occupying energy minima positions in the neighborhood of the line defects are the ones calculated from the molecular statics simulations presented in Chapters 2 and 4. Obviously, as one can see, the extent of the binding and anti-binding zones decreases as temperature increases.

Most of the binding sites around an edge dislocation can be found above the glide plane, in the crystal half under tension; anti-binding sites, in turn, are distributed preferentially under the glide plane, in the half under compression. However, we can discern an overlap zone near the glide plane. The atmosphere width, at $T = 300$ K, is of approximately 15 nm, with a height of approximately 6 nm. At $T = 600$ K, both the width and the height of the Cottrell atmosphere decrease by a factor of 0.5.

For a screw dislocation, binding and anti-binding sites are radially distributed around the dislocation core, rotated by 60° with respect to each other. At $T = 300$ K, the atmosphere radius is of approximately 4 nm, and half this value at $T = 600$ K. Overlap between binding and anti-binding zones can also be seen here and this feature can be easily explained. Outside the core of a screw dislocation, the stress field is predominantly shear, and near the glide plane of an edge dislocation, where the same overlap is observed, the most important component of the stress field is σ_{xy}. Differently from volumes where normal stress predominates (e.g., above and below the core of an edge dislocation), where the size of the locus that may be occupied by the carbon atom determines the binding energy with the dislocation, in volumes where the predominant stress is shear we may find interstitial positions with positive and negative binding energies mixed, since the binding energies in this case depend on the orientation of the tetragonal distortion imposed by the interstitial atom.

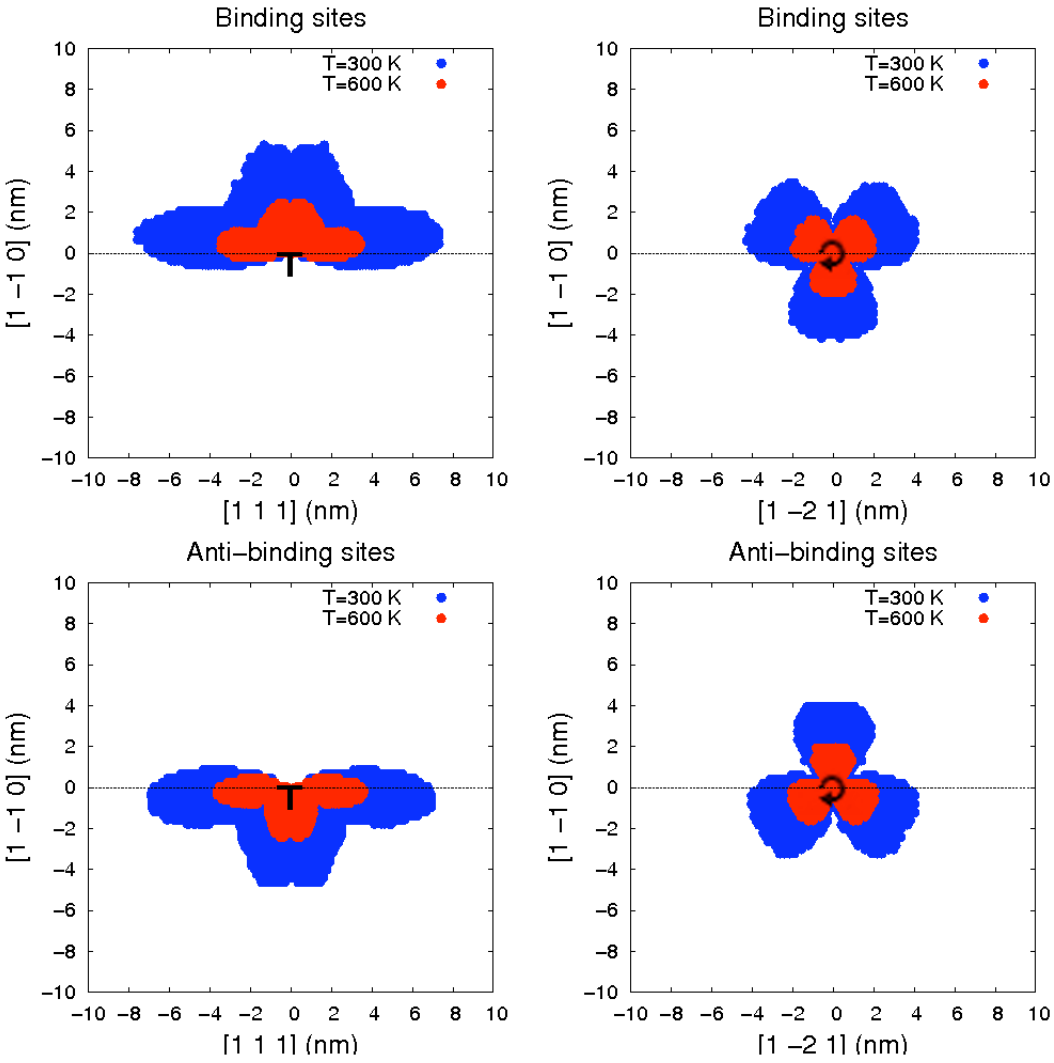

Figure 5.4: Extent and shape of the binding and anti-binding zones around an edge (left) and a screw (right) dislocation defined according to the criterion of Ref. [Cochardt 1955] at $T = 300$ K and $T = 600$ K. The dotted line represents the glide plane.

5.4.2 Carbon concentration in a Cottrell atmosphere

Before calculating carbon distributions with Eq. (5.5), the code outlined in Algorithm 5.1 was used to estimate the saturation concentration within the first shell ($R < b \approx 0.25$ nm) around an edge or a screw dislocation. A total of 100 simulations were performed for each dislocation type. In every simulation, the stop condition was fulfilled after 25 consecutive rejected configurations. On average, the saturation concentration occurs when the occupancy probability is equal to 17% (edge) and 16% (screw). These values correspond, in our simulation boxes, to 31 ± 4at%C (edge) and 21 ± 3at%C (screw). They still are much larger than the maximum carbon concentration in the vicinity of a screw dislocation experimentally found (8 ± 2at%C [Wilde 2000]), but they are much more reasonable than what is given by Fermi-Dirac statistics alone.

Taking into account the saturation concentration calculated previously as the maximum occupancy (i.e., the maximum value of $\overline{n}_i$ was 0.17 near an edge dislocation and 0.16 near a screw dislocation), the carbon distributions were generated by Eq. (5.5) from the carbon-dislocation binding energies obtained by molecular statics simulations presented in Chapters 2 and 4. Fig. 5.5 shows the equilibrium carbon concentration in the stress field of an edge (left) or a screw (right) dislocation at $T = 300$ K and $T = 600$ K. The background occupancy $\overline{n}_0$ corresponded in this case to a carbon concentration in the matrix of 0.18at%C, such as in Refs. [Miller 2003, Miller 2006]. A larger value of $\overline{n}_0$, corresponding to a solute concentration in the iron matrix of 0.85at%C [Wilde 2000], was used to generate the carbon distributions shown in Fig. 5.6. As expected, the larger the carbon content initially in solid solution, the more dense the Cottrell atmosphere decorating a dislocation will be (according to Eq. (5.5)). In any case, it is evident by visual inspection that, apart from the core, the Cottrell atmosphere around a screw dislocation is much more dilute than the atmosphere in the zone under tension above the core of an edge dislocation. On the other hand, right below the core of an edge dislocation, where the compressive stress is maximum, the probability to find a carbon atom is for all practical ends equal to zero.

In addition, the carbon positions in a Cottrell atmosphere at a given temperature can be randomly generated taking into account the occupancy probabilities calculated above, being used, for example, as the initial coordinates for atomistic simulations. To provide an example, Fig. 5.7 shows the carbon atoms forming a Cottrell atmosphere surrounding a screw dislocation at $T = 300$ K, considering a background concentration of 0.18%C.

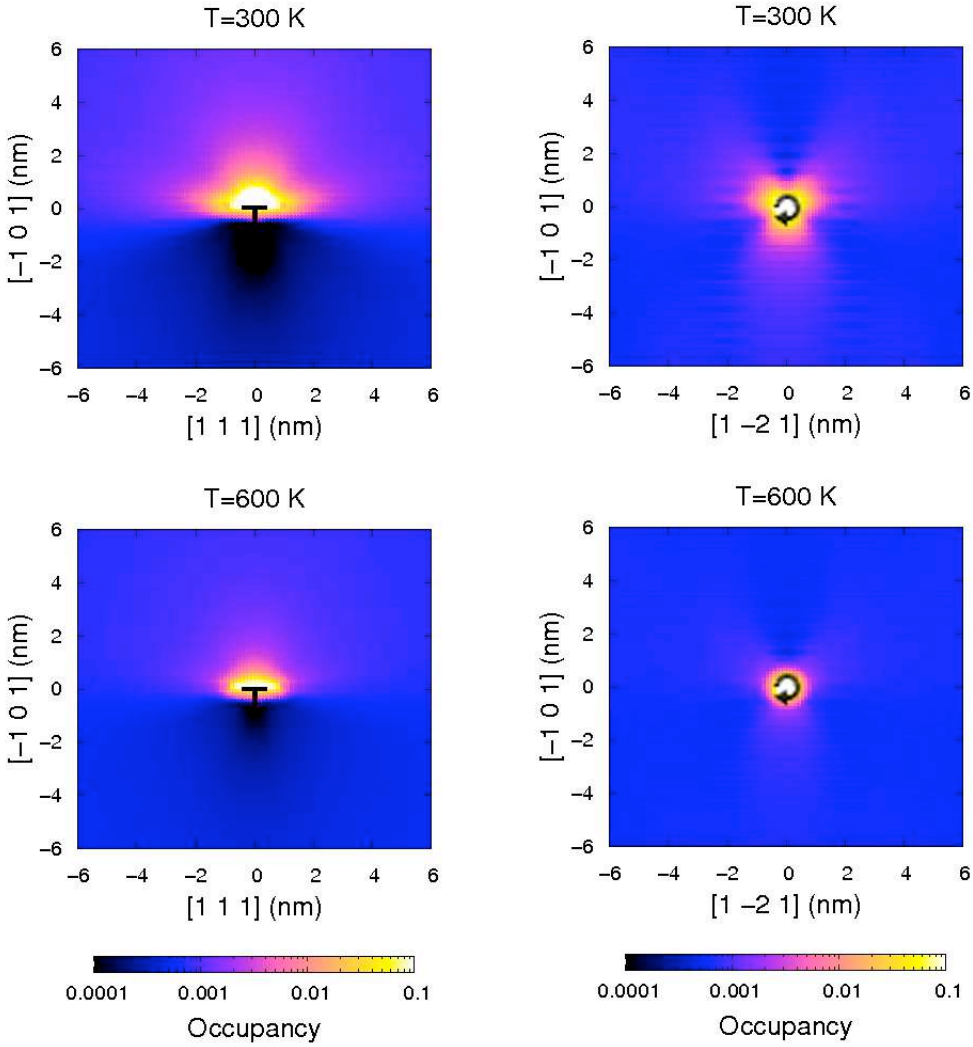

Figure 5.5: Mapping of the fractional occupancy of interstitial sites around an edge (left) and a screw (right) dislocation at $T = 300$ K and $T = 600$ K for Fe-0.18at%C, such as in Ref. [Miller 2003, Miller 2006].

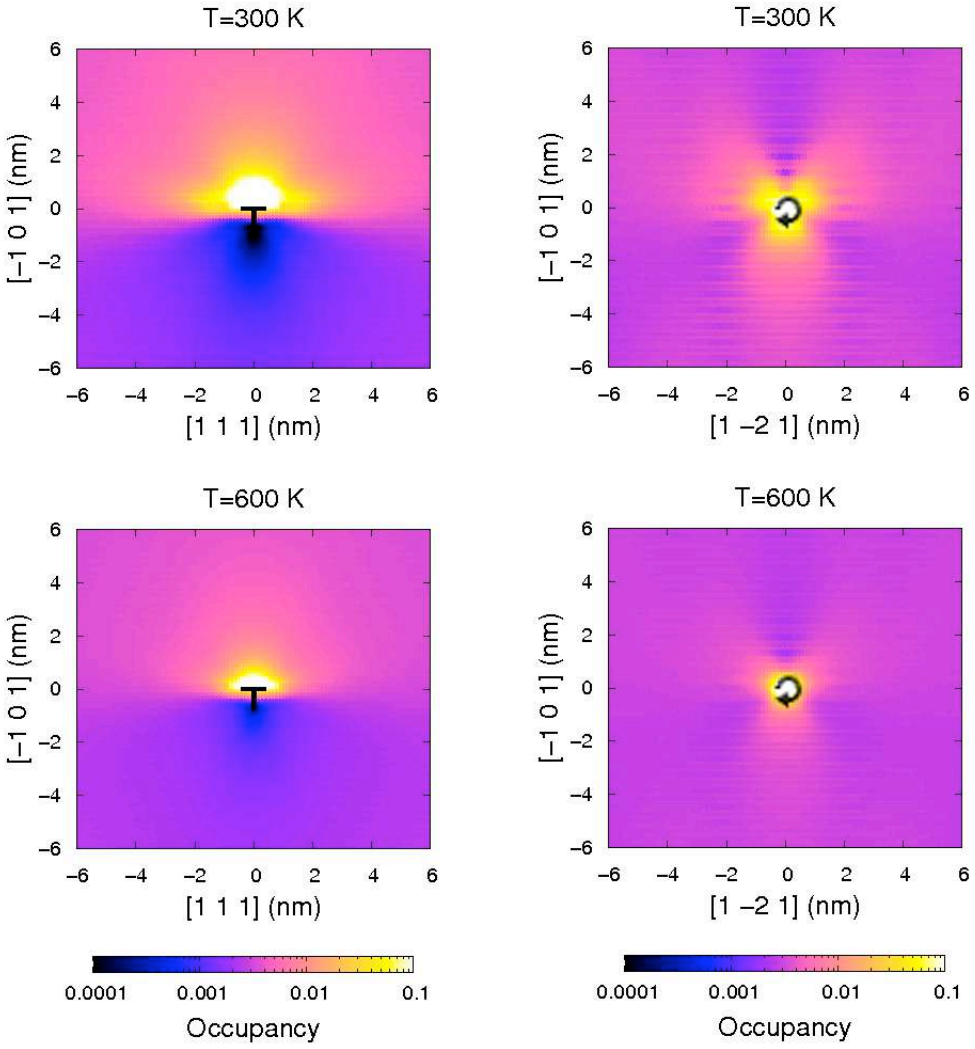

Figure 5.6: Mapping of the fractional occupancy of interstitial sites around an edge (left) and a screw (right) dislocation at $T = 300$ K and $T = 600$ K for Fe-0.85at%C, such as in Ref. [Wilde 2000].

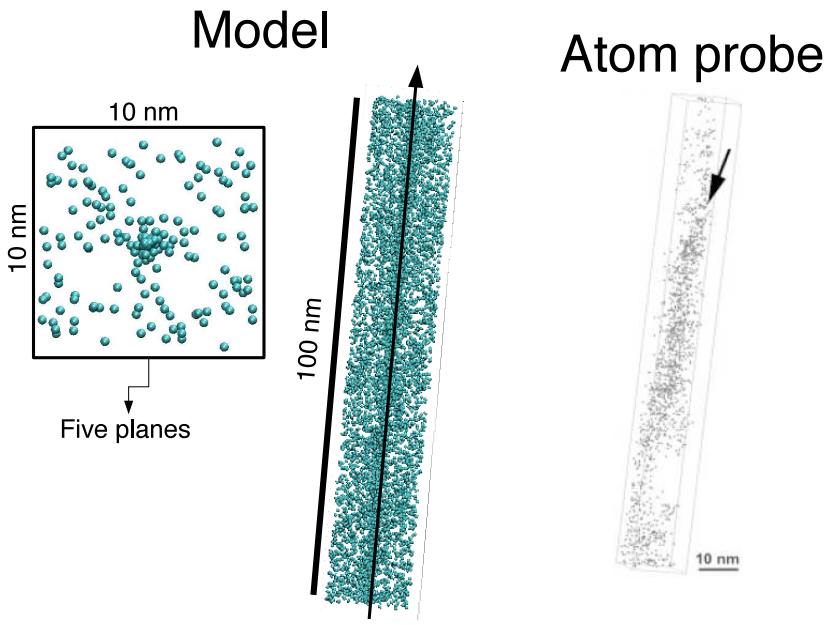

Figure 5.7: (Left) Representation of a carbon Cottrell atmosphere decorating a screw dislocation in α-iron at $T = 300$ K. The iron atoms are not shown for clarity. (Right) Carbon atom map showing solute enhancement along a dislocation in a MA/ODS alloy. Figure adapted from Ref. [Miller 2003].

5.5 Comparison to experimental data

Comparing our theoretical predictions to the experimental data available in the literature is not as trivial as it seems to be *a priori*. In the theoretical corner, we have a statistical distribution and the extent of the atmospheres is usually defined according to a quantitative criterion based on the carbon-dislocation binding energies, as shown in Fig. 5.4. On the other hand, one should expect that carbon concentration is very low in the outer shells of the atmospheres imaged by atom probe techniques. Consequently, in the far-field, where the carbon atoms are weakly bound to the dislocation, the frontier where the atmosphere ends and the matrix starts cannot be precisely defined. The authors of Ref. [Wilde 2000] have used a predominantly visual criterion to estimate the extent of the solute enhanced region around the line defect. Although we have to admit that it is difficult to think of a different way of doing that, such an approach means that the extent of the atmospheres is somewhat human-biased. In this work, the volume of interest for the purpose of comparison to experimental data was delimited in directions perpendicular to the dislocation line by a rectangle just wide enough to encompass a Cottrell atmosphere defined according to the Cochardt's criterion at $T = 300$ K. In the next paragraphs, we compare our theoretical carbon

Method	References	Dislocation	Extent (nm)	$N_{C/l}$ (nm^{-1})
Atom probe	[Wilde 2000]	Screw	10×10	105
Molecular statics	This work	Edge	15×6	240
	This work	Screw	8×8	125

Table 5.2: Extent and number of carbon atoms per unit length of dislocation, in nm^{-1}, in the zone corresponding to a Cottrell atmosphere in Fe-0.85at%C (low carbon martensite).

distributions with the atom probe data provided by Wilde *et al* [Wilde 2000] and Miller *et al* [Miller 2003, Miller 2006].

We start by looking at Table 5.2, where the number of carbon atoms per unit length of dislocation ($N_{C/l}$) is presented. In this work, $N_{C/l}$ is given by:

$$N_{C/l} = \frac{1}{L} \sum_{i}^{\eta} \overline{n}_i N_i \tag{5.8}$$

where η is the number of energy levels represented in the volume of interest, N_i is the number of sites with carbon-dislocation binding energy E_i^b, and L is the dislocation length, in nm. For the calculation of $\overline{n}_i$ with Eq. (5.5), $\overline{n}_0$ corresponding to a matrix concentration of 0.85at%C was assumed (see Fig. 5.6, at $T = 300$ K). In the experimental work reported by Ref. [Wilde 2000], during the specimen aging (before atom probe data was collected), about 105 carbon atoms per nanometer segregated to form an atmosphere around the dislocation. This value is close to what we have theoretically predicted around a screw dislocation (≈ 125 C/nm), and less than half the number of carbon atoms that are expected to segregate to the stress field of an edge dislocation (≈ 240 C/nm). Thus, it seems that the theoretical results of this work also support the conclusion of Ref. [Wilde 2000], that is, the dislocation depicted in Figs. 5.1 and 5.2 is screw. It should be mentioned that the dislocation line in Ref. [Wilde 2000] is oriented along the [110] rather than the [111] direction. In any case, the agreement between theoretical predictions and the experimental data is remarkable here.

The results presented in Table 5.3, in turn, refer to a more recent experimental work carried out by Miller and co-workers with atom probe tomography [Miller 2003, Miller 2006]. Solute enhancement around dislocations is measured in terms of the enrichment (or partitioning) factor, which is the ratio of the carbon concentration in the atmosphere to the carbon concentration in the matrix. The theoretical enrichment factor ϵ_{fac} from the distributions obtained by Eq. (5.5)

Method	References	Dislocation	Extent (nm)	ϵ_{fac}
Atom probe	[Miller 2003, Miller 2006]	Unknown	10×10	7.7
Molecular statics	This work	Edge	15×6	6.7
	This work	Screw	8×8	5.1
Elasticity+DFT	[Hanlumyuang 2010]	Edge	20×20	5.3
	[Hanlumyuang 2010]	Screw	12×12	4.4

Table 5.3: Extent and solute enrichment in the zone corresponding to a Cottrell atmosphere in Fe-0.18at%C.

was defined as follows:

$$\epsilon_{fac} = \frac{\langle \overline{n}_i \rangle}{\overline{n}_0} \tag{5.9}$$

where $\langle \overline{n}_i \rangle$ is the mean occupancy in the volume of interest. The same amount of background carbon content in the specimen analyzed in Ref. [Miller 2003] (0.18at%C, which yields the carbon distributions represented in Fig. 5.5) was considered in the theoretical calculations of $\overline{n}_i$. The results of Ref. [Hanlumyuang 2010], which employed a combination of DFT (used to calculate the components of the P_{ij} tensor) and anisotropic elasticity to perform carbon distribution in the stress field of dislocations, are also presented. As it can be seen, the theoretical predictions shown in Table 5.3 underestimated the solute enrichment compared to the experimental data. This probably comes mostly from the fact that the theoretical models have not taken into account the effects of the other alloying elements (see Table 5.1) on carbon segregation. For instance, titanium concentration in the dislocation vicinity increased by a factor of 5.5 and titanium is known to form carbides in steel. Moreover, Ref. [Hanlumyuang 2010], due to the limitations of the elasticity approach, have not included in the calculations the core region, defined as a cylinder of diameter $6b$ around the dislocation line. Despite the difference in the compositions of the real alloy and the model systems (only carbon and iron), the agreement can also be considered satisfactory, even from a quantitative point of view, in this case.

5.6 Overview

An equation proposed by Louat has been used to obtain the carbon distribution in the stress field of an edge and a screw dislocation in α-iron. As pointed out by Beshers, Louat's formulation corresponds to the well-known Fermi-Dirac statistics. This approach predicts a high carbon concentration right in the dislocation

core because solute-solute interactions are not taken into account. Saturation concentration has been obtained with a simple iterative algorithm coupled to molecular statics simulations. Results of this program provided a maximum fractional occupancy of 0.15 and 0.19 carbon atom per interstitial site in the first shell ($R < b$) surrounding the line of an edge and a screw dislocation, respectively. These maximum occupancies have been adopted as the upper limit for carbon distributions with Louat's formulation. Theoretical predictions have been demonstrated to be in good agreement with two sets of experimental atom probe data available in the literature.

5.7 Ongoing work

Carbon distributions around dislocations done according to Eq. (5.5) may be a useful supporting tool for the simulation of dislocation dynamics at the atomic scale, provided that the condition of saturation concentration is taken into account. For instance, different carbon concentrations can be generated (see Fig. 5.7) and then the force necessary to unpin the dislocation can be calculated with molecular dynamics simulations by applying an external shear stress.

Conclusions and perspectives

Summary and conclusions

In spite of the fact that strain aging has been theoretically and experimentally investigated for decades since Cottrell and Bilby first proposed their seminal theory, there still is much work to be done in order to achieve the complete understanding of the underlying atomistic mechanisms behind this phenomenon. In this thesis, static strain aging in bcc iron at the atomic scale has been theoretically investigated by bringing together different computational methods. The main results presented throughout the manuscript are summarized in the next paragraphs.

Chapter 2 reported an investigation on the effect of the long range stress fields of an edge and a screw dislocation on carbon diffusion in α-iron. First, the positions corresponding to the energy minima (octahedral sites) and the saddle points (tetrahedral sites) in the low-to-moderate strained iron lattice outside the dislocation core (defined in this work for both dislocation types as a cylindrical volume of radius $4b \approx 1$ nm surrounding the dislocation line) were mapped within a radius of 6 nm from the dislocation line. The carbon-dislocation binding energies were obtained from molecular statics simulations performed by LAMMPS with a Fe-C EAM interatomic potential. In the part of the crystal under tension above the glide plane of an edge dislocation, the binding energies are positive (attractive interaction between the defects), whereas below the glide plane, the crystal is under compression and the binding energies are negative (the defects repel each other). Near the glide plane, the edge dislocation creates an important shear stress, and the type of interaction with a carbon atom (attractive or repulsive) depends on the tetragonal distortion that the point defect induces locally. The screw dislocation, in turn, creates a predominantly shear stress field in the surroundings; zones of positive and negative carbon-dislocation binding energies present a three-fold symmetry around the screw dislocation. The stress field created by both dislo-

cation types induces a location dependent bias on carbon diffusion, which results in a drift in carbon trajectories. Such a bias should play the major role in the early stages of Cottrell atmosphere formation, driving the first arriving solutes towards the core. From the knowledge of the migration energies, it was possible to calculate the transition rates in the neighborhood of the line defects. With these rates, AKMC simulations were performed for temperatures ranging from 300 K to 600 K. Both dislocation types were seen to attract the carbon atoms diffusing nearby, even if this effect is subtle. The fraction of carbon trajectories that terminated in the dislocation core in stress-assisted AKMC simulations (34% for an edge and 32% for a screw dislocation) was larger than in simple (unbiased) random walks (27%). The kinetics of carbon segregation to dislocations obtained by AKMC was fitted to Hartley's model and was demonstrated to obey the $t^{\frac{2}{3}}$ law proposed by Cottrell and observed since then in macroscopic experiments.

In Chapter 3, we obtained energy barriers for carbon migration in the neighborhood of an edge or a screw dislocation with anisotropic elasticity theory and compared to the energy barriers given by molecular statics simulations. It is remarkable that the agreement between the methods is much better for the octahedral sites than for the tetrahedral sites. Regarding the energy barriers, the methods are in reasonable agreement (absolute errors of less than 5 meV on average) if the carbon-dislocation separation is larger than 1.5 nm (screw) and 2–4 nm (edge). However, even small absolute errors in the migration energies may lead to significant temperature-dependent errors in quantities that depend on the Boltzmann factor. For instance, an absolute error of only 5 meV in the energy barriers yields a relative error of about 20% in these quantities at $T = 300$ K. AKMC simulations were carried out at $T = 300$ K with the energy barriers provided by both methods. The kinetics of carbon segregation to dislocations simulated by AKMC with energy barriers calculated by molecular statics has been seen to proceed faster than its counterpart using energy barriers calculated by anisotropic elasticity theory, owing to the largest absolute errors found near the dislocation core. Such a discrepancy indicates that the atomistic treatment still is required in the dislocation vicinity, particularly at low temperatures. On the other hand, anisotropic elasticity theory provides a very fast way to calculate energy barriers in the far-field, where the agreement with atomistic simulations is almost perfect. As such, anisotropic elasticity theory may be a useful tool to be incorporated into a future model to investigate the dynamics of Cottrell atmosphere formation.

In Chapter 4, we used AKMC to study the behavior of a single carbon atom right in the core of an edge or a screw dislocation. From the analysis of the trajec-

tories generated by the simulations, we show that the carbon atom spends most of the time performing back and forth jumps between certain states separated by low energy barriers (0.33 eV and 0.42 eV in the core of an edge dislocation; 0.20 eV in the core of a screw dislocation) rather than traveling fast inside the dislocation channel. This behavior was also observed to predominate in MD simulations at $T = 600$ K (edge and screw) and $T = 800$ K (edge only). Indeed, with our current AKMC implementation, this low barrier problem does not allow us to observe pipe diffusion at temperatures lower than 400 K (edge) and 750 K (screw). The diffusion coefficient for carbon diffusion along the dislocation line was estimated from AKMC-generated trajectories to be about two orders of magnitude larger than the bulk diffusion coefficient, for both dislocation types. Furthermore, the effective activation energies for pipe diffusion were 0.670 eV (edge) and 0.738 eV (screw), about 20% and 5% lower than the energy barrier for bulk diffusion according to the EAM potential (0.816 eV), respectively; the preexponential factor for pipe diffusion was seen to be about two orders of magnitude larger than for bulk diffusion.

Statistical physics using the carbon-dislocation binding energies calculated by molecular statics in Chapter 2 was employed in Chapter 5 to obtain carbon distributions in the stress field of an edge or a screw dislocation. Carbon concentration in the surroundings of the line defects as a function of carbon concentration in the iron matrix was calculated by an equation proposed by Louat, which corresponds to Fermi-Dirac statistics. Taking into account that this equation predicts a non-realistic high carbon concentration near the dislocation core (three or four carbon atoms per iron atom), a simple MC-like algorithm was developed to estimate the maximum carbon content within a radius of b from the dislocation line (where the largest carbon-dislocation binding energies are found). MC predicts a maximum carbon content in the considered volume of 33 ± 2at%C (edge) and 23 ± 2at%C (screw). The saturation concentration calculated by MC was taken as a upper limit in the subsequent applications of Louat's fromulation. The theoretical carbon distributions were compared to experimental atom probe data, revealing a good agreement between our work and experiments. This provided an evidence that our atomistic model is able to describe the carbon-dislocation interactions in a realistic fashion.

Future work

One can see the results presented in Chapters 2 and 3 as the current stage of our efforts to build a model based on AKMC to simulate the dynamics of Cottrell atmosphere formation in α-iron. The very first step, carried out in the course of this PhD work, was to investigate the behavior of a single carbon atom diffusing around a dislocation and eventually being dragged by its stress field towards the core. This is obviously the simplest case, where only two entities (the point and the line defect) interact with each other, and even so it is not free of complications. As SSA proceeds, other carbon atoms arrive to the stress field of the dislocation. One should expect that, with the increasing concentration of solutes, two or more carbon atoms may be found close enough to each other, so that they interact with each other and not only with the dislocation. Such solute-solute interactions have to be taken into account, because they are likely to change the energy barriers for carbon migration (and, consequently, the transition rates). Last but not least, because of the strain in the lattice due to the dislocation, the simulation boxes used thus far lack periodic boundary conditions in directions perpendicular to the dislocation line. Consequently, in the AKMC simulations reported in Chapters 2 and 3, only a fraction of the carbon trajectories reached the dislocation core, while the remaining moved out of the simulation box. To overcome this limitation, periodic boundary conditions have to applied somehow in all directions, which is not a trivial implementation.

For the next step of this project, a model to study the dynamics of Cottrell atmosphere formation is envisaged as follows:

i. The energy minima and saddle points in the far-field are calculated by anisotropic elasticity theory (these calculations are very fast);

ii. Within a certain carbon-dislocation separation, molecular statics simulations is employed to obtain the energy barriers;

iii. Whenever two or more carbon atoms are expected to interact with each other, a more sophisticated method (e.g., NEB) should be used to calculate on-the-fly the energy barriers for carbon migration.

Alternatively, for situation (iii) above, the innovative approach recently proposed by N. Castin, where most of the energy barriers are obtained by an artificial neural network algorithm [Castin 2011], may be useful.

The study of carbon behavior in the core of an edge or a screw dislocation, presented in Chapter 4, still is in a preliminary stage. For the moment, the AKMC

algorithm that we have been using is not able to properly handle the low barrier problem that we faced in the dislocation core, which prevents AKMC simulations of pipe diffusion at low temperatures. To overcome this limitation, the algorithm has to be modified in order to treat the fast and slow transitions separately. In other words, the rates of slow transitions should be calculated taking somehow into account the rates of the fast transitions. An interesting possibility which is easier to be done with MD is to insert two or more carbon atoms in the dislocation core, in order to verify how the mutual interaction between solutes affect pipe diffusion, if it does.

A third branch of research that may be followed regards the effect of a Cottrell atmosphere on dislocation glide. Tapasa and co-workers reported the results of MD simulations on the glide of an edge dislocation with a single carbon atom in its core [Tapasa 2007]. The natural next step is to perform the same investigation on a more realistic system, where many carbon atoms will be decorating a dislocation. A Cottrell atmosphere at different instants of the strain aging process, for a given initial carbon concentration in the iron matrix, can be generated according to the scheme presented in Chapter 5. Then, the force required to unpin the dislocation and make it move free from its Cottrell atmosphere can be calculated, at different temperatures and strain rates, from molecular dynamics simulations. In these MD simulations, an external shear stress is applied to the simulation box in order to make the dislocation move along its glide plane. Given the size of the systems and the number of simulations to be carried out, one should expect that, in contrast with AKMC simulations, a large amount of CPU time will be required to accomplish this work.

Although there is much to be done concerning the Fe-C system, extending the investigations to other solutes than carbon (e.g., nitrogen, phosphorus, manganese, copper, etc) is certainly desirable from a technological point of view. For the sake of example, phosphorus is known to have an important effect on the thermal and neutron embrittlement of reactor pressure vessel steels. Obviously, considering other alloying elements depends first on the availability of interatomic potentials. A number of EAM potentials for binary Fe-X systems (where X=Cu, Cr, Ni, P, Mg) has been developed in recent years.

Apart from dislocations, grain boundaries constitute another class of intrinsic extended defects commonly found in real materials. Grain boundary segregation of impurities also plays an important role in the mechanical properties of metals, since it results in loss of grain boundary cohesion and facilitates brittle fracture. This is another aging aspect that can be addressed in a near future by atomistic

kinetic Monte Carlo in a fashion similar to what we have done so far for carbon segregation to dislocations.

Appendix A

The Fe-C interatomic potential

Abstract

Here we present the iron-carbon potential that we have used in the atomistic simulations. It is based on the embedded atom method (EAM) and was constructed so as to fit to the data obtained from *ab initio* calculations for a carbon atom in dilute solid solution in bcc iron, occupying either an octahedral or a tetrahedral site. The original potential has been seen to predict a saddle point slightly off the tetrahedral position. This problem was fixed by adding a Gaussian function to the Fe-C pairwise function, which does not change the position corresponding to the local energy minimum (the octahedral site).

A.1 Introduction

Ideally, the total energy of a system of atoms should be obtained by solving the main equation of quantum mechanics, i.e., the time-independent (stationary) Schrödinger equation $\hat{H}\psi = E\psi$ (here, $\hat{H}$ is the Hamiltonian operator and ψ is the wave function). In practice, this is not doable even for isolated atoms as light as helium. Some approximations to the exact solution of $\hat{H}\psi = E\psi$ have been developed along the decades, and nowadays the most widely used is density functional theory (DFT) proposed by Walter Kohm in the 1960s [Kohm 1965]. In Kohm's formulation, the total energy of an atomic system is a functional of the electron density function. The development of approximations to the exact solution of the Schrödinger equation in general and DFT in particular made possible to simulate the ground state properties of a number of molecular and solid state systems. Despite such an important advance in the theoretical side, an issue still remains concerning the size of the model systems. Simulations of some complex systems in a realistic fashion (e.g., proteins or, in our case, the environment surrounding line defects in a crystal) requires that some thousands of atoms are included in the model, the computational cost of which is prohibitive even with the most efficient quantum-mechanical approximations. This is normally achieved by analytical interatomic potentials that mimic somehow the chemistry of a realistic atomic system without taking into consideration explicitly the underlying electronic structure.

For solid state systems, the embedded atom method (EAM) proposed by Daw and Baskes [Daw 1983] became very popular in recent years. In their method, a semi-empirical interatomic potential is obtained by fitting some parameters in order to reproduce a certain set of key properties of the material of interest (e.g., elastic constants, binding energies, heat of formation, lattice parameter, etc) given by *ab initio* calculations or experiments. The total potential energy of a system within EAM is given by the following equation:

$$E^{tot} = \frac{1}{2}\sum_{i,j}\phi_{ij}(r_{ij}) + \sum_{i}F_i\left[\sum_{i\neq j}\rho_j(r_{ij})\right] \tag{A.1}$$

In this equation, $\phi_{ij}(r_{ij})$ is a short range pair potential function that obviously depends on the types of the atoms i and j and describes the attractive/repulsive electrostatic interactions between them. $F_i[\overline{\rho}(r_{ij})]$ is the embedding functional, which represents the interaction of the i-th atom with the surrounding electron density. An important corollary proved by Stott and Zaremba and useful in

the derivation of the embedding functional $F_i[\overline{\rho}(r_{ij})]$ states that the energy of an impurity is a functional of the unperturbed electron density at the position occupied by the impurity in the host lattice [Stott 1980]. In Daw and Baskes' words, EAM is thus called because the i-th atom is considered as an impurity embedded in the host lattice consisting of all other atoms, so that the energy of the i-th atom is a functional of the constant electron density of all other atoms before its introduction in the host at that specific location.

Taking into consideration that the system investigated in this thesis is a relatively large one (some hundreds of thousands atoms) where an interstitial atom (carbon) is found in solution in a metallic matrix (α-iron), an EAM potential ends up being the most appropriate approach to account for the atomic interactions. In the next sections, we provide a brief description of the iron-carbon EAM potential that has been used throughout this work.

A.2 The original Fe-C potential

The original version of the iron-carbon EAM potential used in this work has been developed by Becquart and co-workers and is presented in details in Ref. [Becquart 2007]. It has been fitted to *ab initio* calculations performed with the Vienna Ab initio Simulation Package (VASP) [Kresse 1993], for a carbon atom in dilute solid solution occupying either an octahedral or a tetrahedral site in a cubic simulation box with 128 iron atoms arranged on a bcc lattice. In the DFT calculations, the $3d^6 4s^2$ valence configuration was used for the Fe atom; for the C atom, $2s^2 2p^2$. A non-exhaustive description of the Fe-C potential functions follows in the next paragraphs.

Following Refs. [Ackland 1997, Mendelev 2003], the Fe-C interaction was described by a linear combination of truncated polynomials of degree 3 in the interval $1 \leq r \leq 3.502$ Å:

$$\phi_{Fe-C}(r) = \sum_{i=1}^{N} a_i H(b_i - r)(b_i - r)^3 \tag{A.2}$$

where H is the Heavyside function and the parameters a_i and b_i can be seen in Table A.1.

The carbon electron density in the interval $0 \leq r \leq 4.808$ Å was postulated to be:

$$\rho_C(r) = \sum_{i=1}^{N} c_i H(d_i - r)(d_i - r)^3 \tag{A.3}$$

N	a_i (a.u./Å^3)	b_i (Å)
1	25.8403449446387	1.57392207030071
2	5.29633693622809	2.50697533078414
3	4.03000262768764	2.55706258348374
4	-7.23257363478654	2.74993431502404
5	-7.91809159848018	3.11129997684853
6	0.283612435794859	3.50162017458081
7	12.1869023019844	1.64805018491946
8	9.19127905165634	3.08003832563079

Table A.1: Parameters of the iron-carbon cross potential. a.u. means density arbitrary units. Values taken from Ref. [Becquart 2007].

N	c_i (a.u./Å^3)	d_i (Å)
1	-16.205911	0.5
2	-0.245035	4.54378

Table A.2: Parameters of the carbon electron density potential. a.u. means density arbitrary units. Values taken from Ref. [Becquart 2007].

where the parameters c_i and d_i are shown in Table A.2.

Finally, the embedding function is represented as follows:

$$F_C(\overline{\rho}) = F_1\sqrt{\rho} + F_2\rho^2 \tag{A.4}$$

In this equation, $F_1 = -2.78333808071882$ eV·a.u.$^{-1/2}$ and $F_2 = 1.45647907575885 \times 10{-}3$ eV·a.u.$^{-2}$, where a.u. is a density arbitrary unit.

The parameters in Eqs. (A.2), (A.3), and (A.4) were fitted with the aid of the software ASSIMPOT [1]. In the frame of ASSIMPOT, the target functions are discretized on a mesh or projected on a finite number of other functions. The fit procedure consists of finding out the values of the coefficients that yield the minimal deviation of the EAM model with respect to the reference data. The algorithm of Broyden, Fletcher, Goldfarb, and Shanno (BFGS) has been used to carry out numerical optimization [Press 2007].

The Fe-Fe interactions, in turn, are described by the interatomic potential developed by Ackland and Mendelev [Mendelev 2003, Ackland 2004]. This potential provides a good description (compared to both *ab initio* calculations and experiments) of many bulk properties and – which is more important, considering the needs of our work – of the geometry of the dislocation cores. It is currently admitted to be the state-of-the-art potential for α-iron. To the interested reader,

[1] Described in: "Documentation du code ASSIMPOT: bases théoriques et utilisation, note interne EDF, HI-23/05/003/A".

the analytical form of the potential Fe-Fe functions are presented in Table 5 in Ref. [Ackland 2004].

As the potential aimed at the simulation of dilute solid solutions of carbon in bcc iron, no C-C interaction part was derived. Moreover, EAM does not seem to be the best choice to describe carbon-carbon interactions, because it does not allow for directional covalent bonding.

Despite the fact that this Fe-C potential was fitted to the data corresponding to only two simple configurations (i.e., an isolated carbon atom sitting on an octahedral or a tetrahedral site), its application to other configurations (e.g., two carbon atoms in neighboring positions) have been seen to compare well with *ab initio* calculations or experiments, as one can see in Table 5 in Ref. [Becquart 2007]. This potential has been successfully used in a number of works recently published [Clouet 2008, Garruchet 2008, Hanlumyuang 2010, Sinclair 2010]. For the time being, it is, to our knowledge, the Fe-C potential that better describes the minimum energy path for carbon migration in bcc iron and this is the reason for having chosen it. However, in the course of this PhD work, a bad description of the energy potential landscape in the vicinity of the tetrahedral site has been found. This problem and the solution that we have applied are discussed in the next section.

A.3 The saddle point problem

In Ref. [Becquart 2007], the tetrahedral site is said to correspond to the the saddle point for carbon migration in bulk α-Fe according to the EAM potential. The migration energy, which is the difference of the total energies of the carbon atom sitting on the tetrahedral and the octahedral sites, is 0.85 eV. However, some simulations performed in the frame of this PhD work for testing purposes reached a different conclusion. These simulations are described in the following. First, a cubic simulation box with 16,000 iron atoms ($20 \times 20 \times 20$ unit cells) was built to be used with LAMMPS. Then, a number of planes perpendicular to the migration path followed by a carbon atom from a [100] O-site to a [001] O-site, passing through a [010] T-site, was defined. This corresponds to an octahedral-to-octahedral path along the [010] direction. For every plane, a rectangle of area 0.1×0.1 nm^2 with the octahedral-to-octahedral line passing through its center was divided into an uniform grid (grid spacing of 0.005 nm). Molecular statics simulations were performed, where a carbon atom was inserted in a position corresponding to a grid point. The carbon atom was kept fixed at its position

while the iron atoms were allowed to fully relax.

Fig. A.1 shows the energy contour maps for each plane. Each point in the maps represents the total energy of the system with a carbon atom at that position minus the total energy of the carbon atom in the octahedral site. We can see in this sequence of maps that the minimum energy path is unique – the minimum of each plane is found right in its center – up to very close to the tetrahedral site, where the minimum energy path is split into four degenerate saddle points, yielding an energy barrier of 0.81 eV. Therefore, the actual energy barrier for carbon migration predicted by the original EAM potential is 0.04 eV lower than the energy barrier reported in Ref. [Becquart 2007]. The positions of the saddle points were $(T_x \pm 0.15, T_z \pm 0.15)$, where T_x is the x coordinate of the T-site (along the [100] direction) and T_z is its z coordinate (along the [001] direction). From theses simulations, the conclusion that one can reach is that the T-site, according to the Fe-C potential, is a local maximum on the plane, not a minimum, as it must be if it was the saddle point.

The solution for this problem was not trivial. Indeed, it was only attained by trial and error. We first identified that when the system is at one of the four energy minima on the plane that contains the tetrahedral site, represented in Fig. A.1 (E), the carbon atom has not four iron atoms at a distance of 0.257 nm as second nearest neighbors. It has two second nearest neighbors at a distance of 0.236 nm and two, now third, nearest neighbors at a distance of 0.271 nm. Our attempts consisted of adding Gaussian functions to the Fe-C pairwise interaction function $\phi(r)$ near $r = 0.257$ nm in order to lower the second derivative at this point. After many trials, a set of three Gaussian functions $g_i(r) = a_i \exp[(-(r-r_i)^2/60\sigma]$ were added and brought the saddle point back to the tetrahedral site. The parameters of the Gaussian functions are $a_1 = -0.01$, $a_2 = a_3 = 0.01$, $r_1 = 0.2539$ nm, $r_2 = 0.2365$ nm, $r_3 = 0.2713$ nm, and $\sigma = 0.0002$. In Figs. A.2 and A.3, one can see the energy mapping on the plane perpendicular to the [010] direction that contains the tetrahedral site (in the center), obtained by molecular statics simulations in the same way as the results shown in Fig. A.1 with the original and the modified Fe-C EAM potential, respectively. It can be clearly seen that the modification introduced in the Fe-C potential brings the saddle point back to the tetrahedral site. This modification is obviously very localized. Consequently, it does not change neither the geometry nor the total energy of the local energy minimum, which remains corresponding to the carbon atom in the octahedral site. In addition, the configurations in Table 5 in Ref. [Becquart 2007] were simulated with the modified Fe-C potential, and all the results matched.

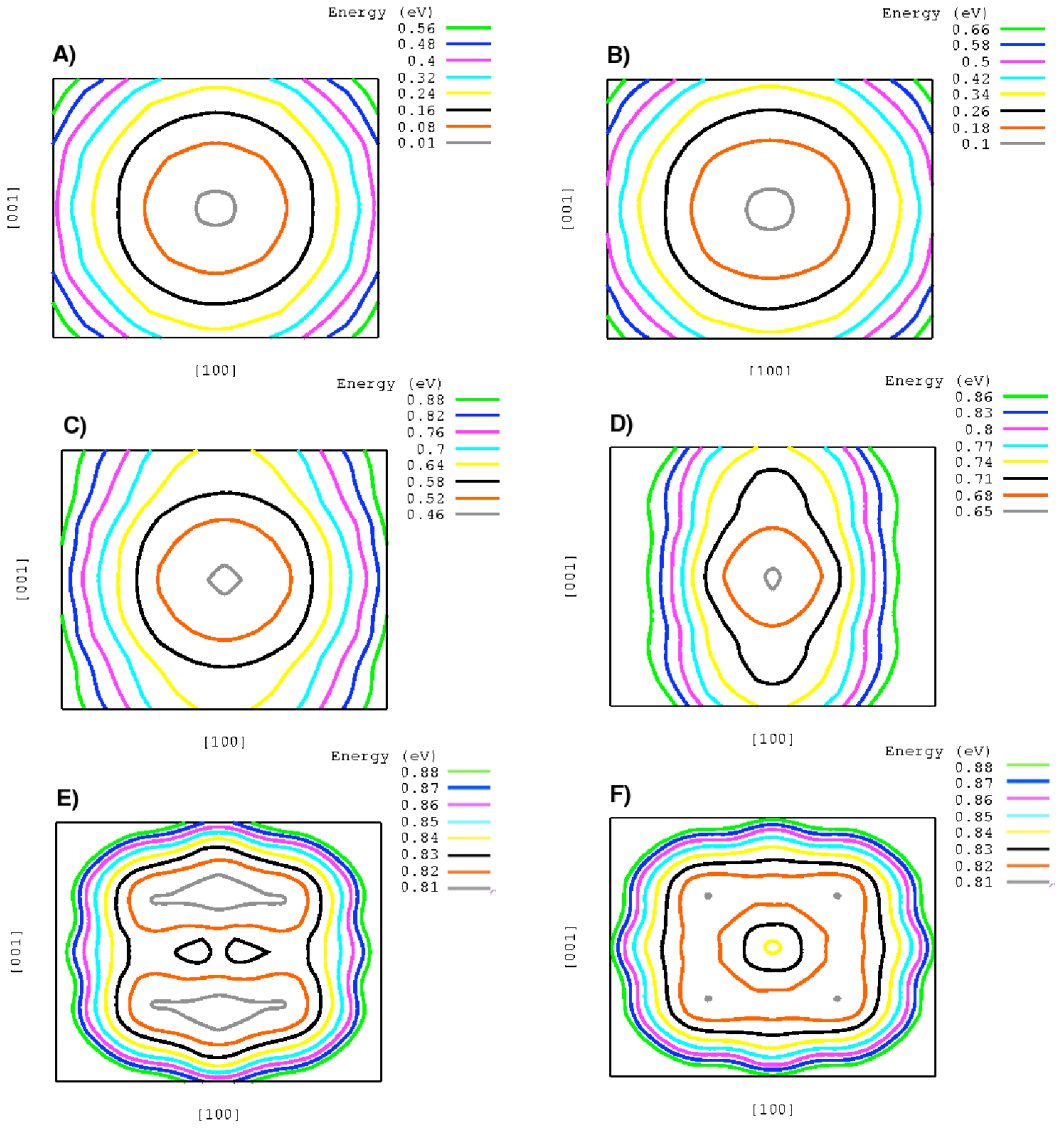

Figure A.1: Energy mapping on several planes perpendicular to a [010] carbon migration path: (A) origin (plane containing the O-site), (B) origin + 0.02 nm, (C) origin + 0.05 nm, (D) origin + 0.06 nm, (E) origin + 0.07 nm, (F) origin + 0.07138 nm (plane containing the T-site).

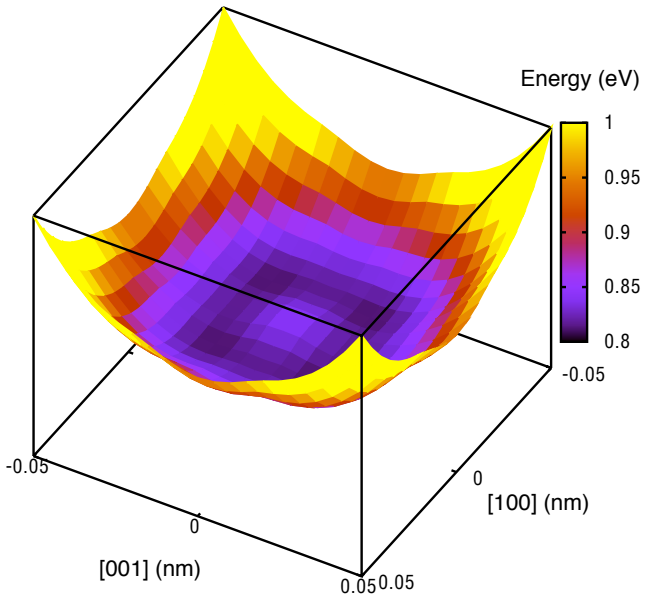

Figure A.2: Energy mapping on the plane perpendicular to the [010] direction that contains the tetrahedral site (in the center) obtained by the original Fe-C EAM potential. The energy reference is the total energy of the simulation box with the carbon atom occupying the octahedral site.

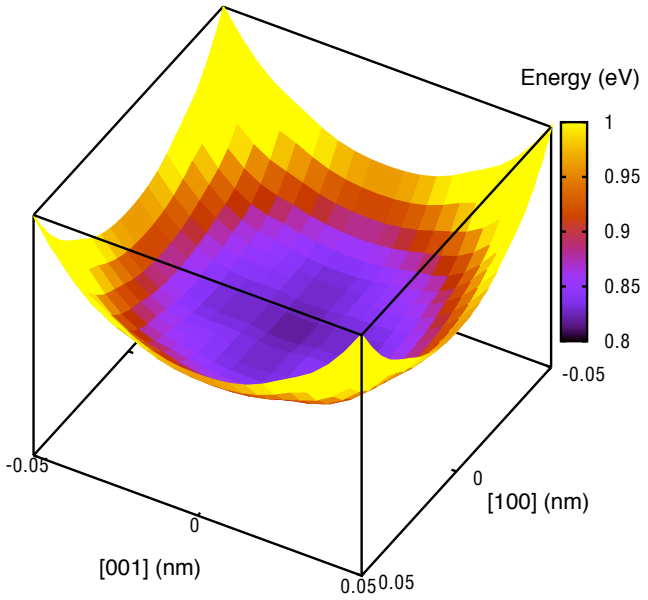

Figure A.3: Energy mapping on the plane perpendicular to the [010] direction that contains the tetrahedral site (in the center) obtained by the modified Fe-C EAM potential. The energy reference is the total energy of the simulation box with the carbon atom occupying the octahedral site.

Appendix B

Résumé: "Simulation à l'échelle atomique du vieillissement statique dans le fer α"

B.1 Présentation de la problématique et l'approche

La plupart des aciers utilisés dans les centrales nucléaires subissent des traitements thermomécaniques de mise en forme (hypertrempes, laminages, traitements thermiques de revenu, de recristallisation...) qui leur confèrent les propriétés requises. Mais les matériaux peuvent se retrouver alors dans des états d'équilibre thermodynamique instables ou métastables. Sous l'effet de la température de fonctionnement, ils vont avoir tendance à évoluer pour retrouver plus ou moins vite leur état d'équilibre thermodynamique. Ce retour à l'équilibre (vieillissement) se traduit par une évolution microstructurale et par une évolution des propriétés des matériaux: le plus souvent durcissement et fragilisation (perte de ductilité et/ou décalage de la température de transition fragile-ductile). Parmi les principaux mécanismes de vieillissement susceptibles d'apparaître sur les composants des centrales nucléaires, les plus importants sont la précipitation et la ségrégation des atomes interstitiels (carbone ou azote) sur les dislocations qui entraînent selon la température un vieillissement statique ou dynamique. Ces deux mécanismes sont liés à la diffusion et la mobilité des interstitiels ainsi que des dislocations. Si les bases de la diffusion sont relativement bien connues dans une matrice libre de contrainte, il en est tout autrement quand les

espèces diffusantes subissent un champ de contraintes de nature hétérogène lié à la présence des dislocations ou d'autres défauts. De plus, les processus physiques d'ancrage-désancrage des dislocations sont assez mal connus. Dans les deux cas, la modélisation de ces mécanismes à l'échelle atomique permet de mieux comprendre et/ou de prédire le comportement des aciers lors du vieillissement.

Au cours de ce projet, nous avons donc développé une approche couplant deux techniques complémentaires de simulation à l'échelle atomique: la statique moléculaire (SM) et le Monte Carlo cinétique (MCC). La méthode de MCC qui traite des sauts de différentes espèces atomiques sur un réseau rigide nécessite en effet de connaître les probabilités de saut et les temps de résidence qui ont été, dans ce travail, obtenues par des simulations de SM. Le modèle de cohésion choisi pour cette tache est un potentiel interatomique développé dans le cadre du projet PERFECT. Dans un premier temps, nous avons analysé et modifié le potentiel inter-atomique Fe-C, puis nous avons déterminé les énergies de point-selle par SM afin de créer un catalogue d'interactions carbone-dislocation (coin et vis) pour un très grand nombre de configurations. Ces interactions ont alors été utilisées dans le MCC pour étudier la diffusion d'un atome de carbone vers les dislocations coins et vis dans le fer cubique centré et essayer de prédire la cinétique de formation des atmosphères de Cottrell.

Les deux dislocations ont été créées par le déplacement des atomes de fer selon la théorie de l'élasticité anisotrope des défauts linéaires [Eshelby 1953, Stroh 1962, Stroh 1958]. Un tel déplacement correspond au champ de Volterra élastique créé par la dislocation. Dans les deux cas, le vecteur de Burgers est $\vec{b} = a0/2[111]$ et le plan de glissement est un plan $\{\overline{1}01\}$ qui divise les boîtes de simulation en deux moitiés. Ce sont en effet les dislocations les plus couramment observées dans le fer cubique centré. Pour la dislocation coin, la ligne de dislocation est orientée selon la direction $[1\overline{2}1]$, tandis que la ligne de dislocation de la dislocation vis est orientée selon la direction [111]. En raison du fait que la dislocation détruit la périodicité du cristal dans les directions perpendiculaires à la ligne de dislocation, des conditions aux limites périodiques ont été appliquées seulement le long de cette direction. Les boîtes de simulation, representées dans la Fig. B.1, sont des cylindres de rayon 15 nm. Les anneaux extérieurs se composent d'atomes de fer fixés durant les simulations, afin d'éviter des relaxations indésirables dues aux effets des surfaces libres.

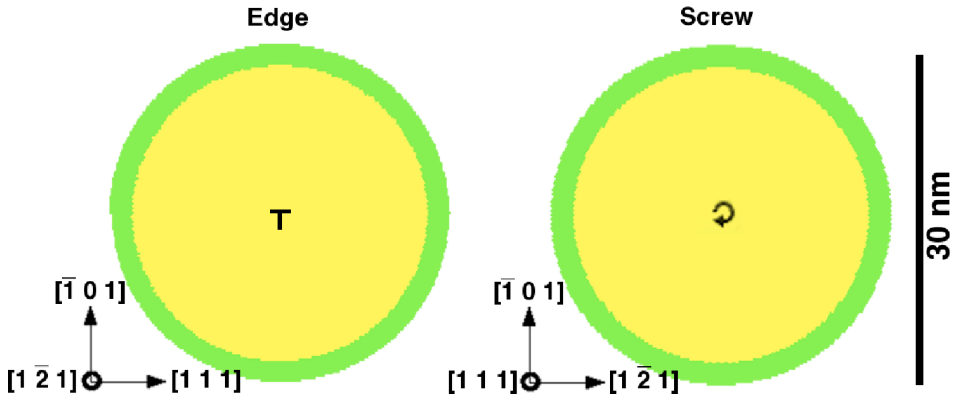

Figure B.1: Vue du haut des boîtes de simulation cylindriques contenant une dislocation coin et une dislocation vis (au centre), respectivement. Les atomes de fer dans les anneaux extérieurs verts (2 nm d'épaisseur) sont maintenus fixes afin de représenter le champ de déplacement correct créé par les dislocations.

B.2 Effet du champ de contraintes des dislocations sur la diffusion du carbone

Les simulations de SM ont été réalisées avec le code LAMMPS [Plimpton 1995] et un potentiel EAM développé récemment [Becquart 2007], afin d'obtenir les configurations atomiques, les énergies de liaison carbone-dislocation et les énergies de migration de l'atome de carbone dans le voisinage des défauts linéaires. En utilisant les informations recueillies par SM, des simulations MCC ont été réalisées pour des températures dans la gamme 300-600 K, afin d'étudier le comportement de l'atome de carbone dans le champ de contraintes des dislocations avant qu'il ne soit piégé par le coeur de la dislocation. Ces travaux peuvent être donc considérés comme une toute première étape vers la simulation complète à l'échelle atomique du stade initial du vieillissement statique, à savoir la formation d'une atmosphère de Cottrell autour d'une dislocation dans le fer.

L'atome de carbone est beaucoup plus petit que l'atome de fer. Pour cette raison, on le trouve donc en solution solide dans une matrice de fer dans des positions interstitielles. Il existe deux types des sites interstitiels dans le réseau du fer cubique centré: dans le site octaédrique (O), l'atome de carbone est au centre de l'octaèdre formé par six atomes de fer qui occupent les sommets. Les plus proches premièrs voisins (deux atomes) et les seconds voisins (quatre atomes) sont situés à une distance de 0.179 nm et 0.198 nm, respectivement, de l'atome de carbone, selon le potentiel EAM. Dans le site tétraédrique (T), l'atome de carbone est entouré de quatre atomes de fer situés à une distance de 0.179 nm de celui-ci.

L'interprétation des résultats expérimentaux [Porter 1981], corroborés plus tard par des calculs *ab initio* [Jiang 2003, Domain 2004] indique que le mécanisme de diffusion du carbone interstitiel dans le fer cubique centré s'effectue par des sauts de site octaédrique en site octaédrique en passant par un site tétraédrique. Lorsque il se trouve dans un site octaédrique, l'atome de carbone est au centre de l'un des faces d'une cellule cubique centré. Il peut alors sauter sur un des quatre sites octaédriques voisins coplanaires situés sur les bords du cube. L'hypothèse de base du travail présenté ici est que le mécanisme de diffusion simple se produit le plus souvent là où la matrice de fer est modérément distordue par la présence d'une dislocation.

Les énergies de liaison carbone-dislocation ont été obtenues par SM. Elles sont présentées dans les Figs. B.2 et B.3. Dans notre convention, lorsque $E^b > 0$, l'interaction entre les défauts est attractive; sinon, si $E^b < 0$, elle est repulsive. Les barrières d'énergie ont été également obtenues par des simulations de SM. Les Figs. B.4 et B.5 répresentent les barrières d'énergie pour les six types de transitions qui un atome de carbone peut subir autour d'une dislocation coin et d'une dislocation vis, respectivement. Ces barrières ont été utilisées par le programme de MCC afin de simuler les trajectoires du carbone dans le champ de contrainte des dislocations.

Le champ de contraintes d'une dislocation modifie les probabilités des transition autour du défaut linéaire. Le biais que cela ajoute à une marche aléatoire est quantifié par le vecteur de déplacement moyen, défini comme suit:

$$\langle \vec{d} \rangle = \sum_{j=1}^{N} P_{i \to j} \vec{\delta}_{i \to j} \tag{B.1}$$

Les Figs. B.6 et B.7 représentent la projection des vecteurs de déplacement moyen pour $T = 300$ K et $T = 600$ K sur les plans perpendiculaires aux lignes de dislocations pour les dislocations coin et vis, respectivement. On constate que le biais de la diffusion du carbone est beaucoup plus important autour d'une dislocation coin qu'autour d'une dislocation vis.

La cinétique de diffusion du carbone simulée par le MCC avec les barrières obtenues par des simulations de SM est mise en évidence dans les Figs. B.8 et B.9 qui représentent l'évolution de la fraction d'atomes de carbone piégées par les deux types de dislocations. On constate tout d'abord que pour la dislocation coin, un premier effet notable est que la cinétique est accélérée par rapport à la marche aléatoire simple. Un tel effet est évidemment dépendant de la température, mais il est encore présent à la température la plus élevée (600 K) considérée dans

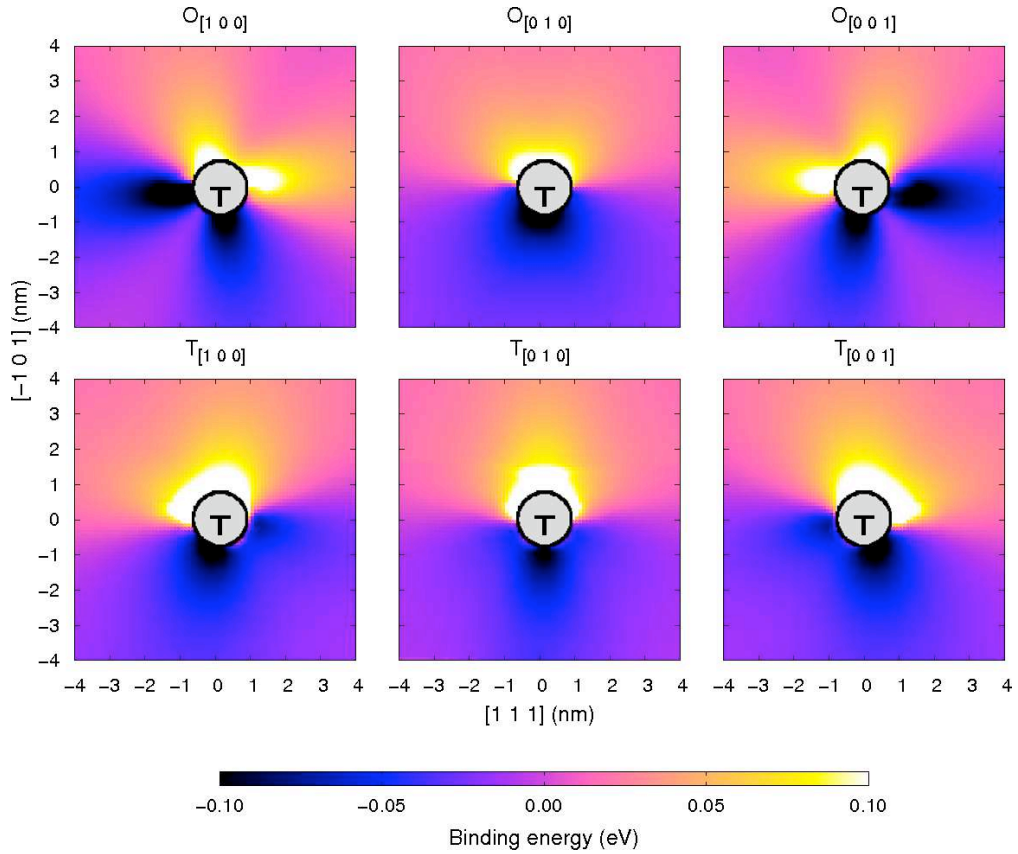

Figure B.2: Cartographie des énergies de liaison carbone-dislocation obtenues par des simulations atomistiques pour les différentes positions possibles de l'atome de carbone autour d'une dislocation coin (au centre) alignée parallèlement à la direction $[1\bar{2}1]$ (perpendiculaire à la page). Le cercle gris au centre (dont le diamètre équivaut à 8b) se rapporte à la région définie comme étant le coeur de la dislocation.

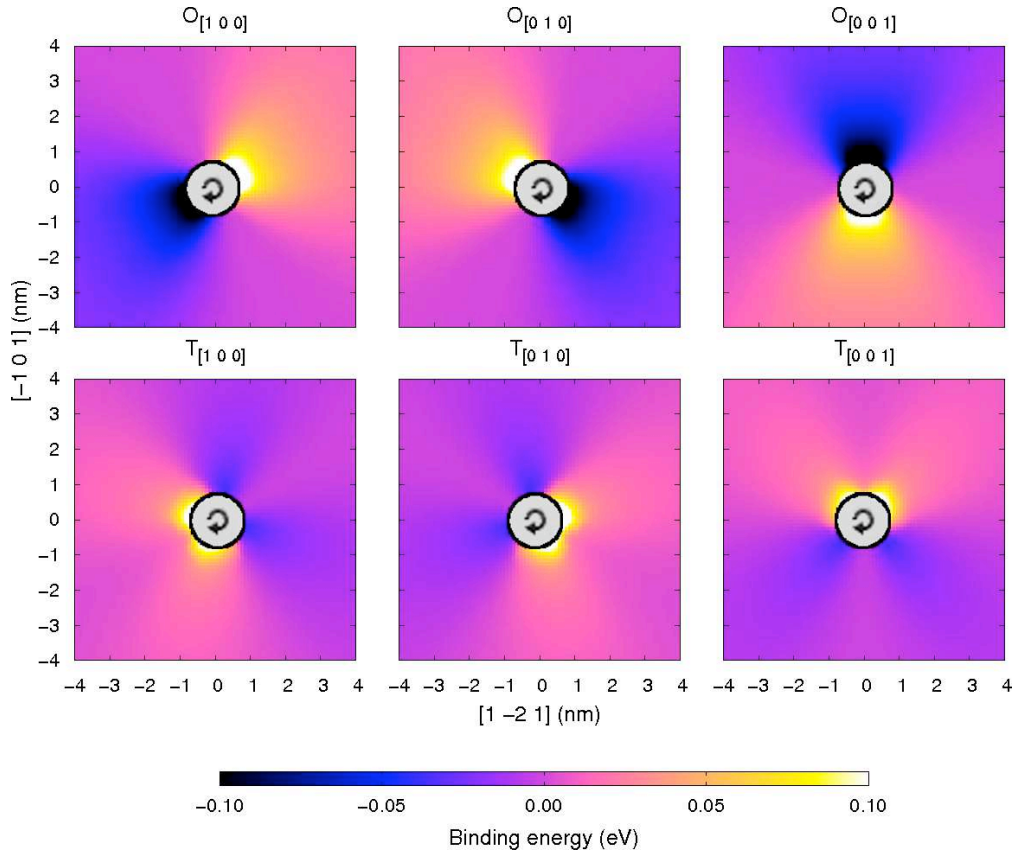

Figure B.3: Cartographie des énergies de liaison carbone-dislocation obtenues par des simulations atomistiques pour les différentes positions possibles de l'atome de carbone autour d'une dislocation vis (au centre) qui est alignée parallèlement à la direction [111] (perpendiculaire à la page). Le cercle gris au centre (diamètre équivaut à 8b) se rapporte à la région définie comme étant le coeur de la dislocation.

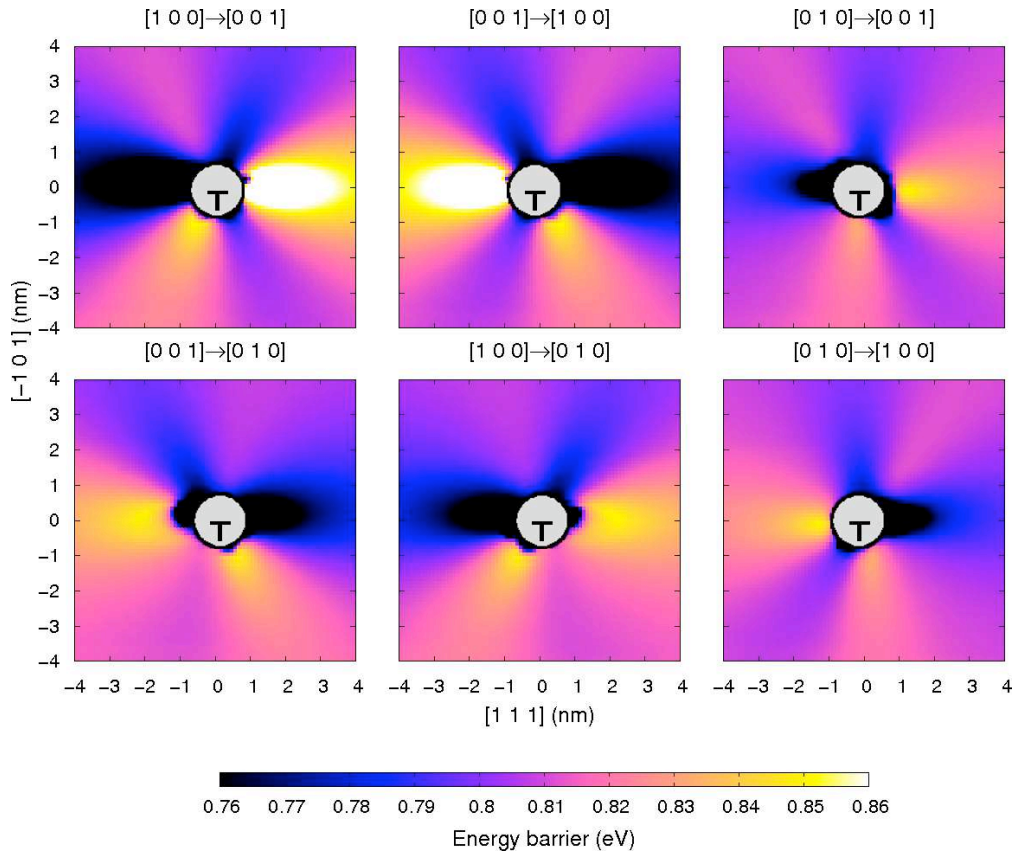

Figure B.4: Cartographie des barrières d'énergie obtenues par des simulations atomistiques pour la diffusion de l'atome de carbone autour d'une dislocation coin (au centre) alignée parallèlement à la direction $[1\bar{2}1]$ (perpendiculaire à la page). Le cercle gris au centre (dont le diamètre équivaut à 8b) se rapporte à la région définie comme étant le coeur de la dislocation.

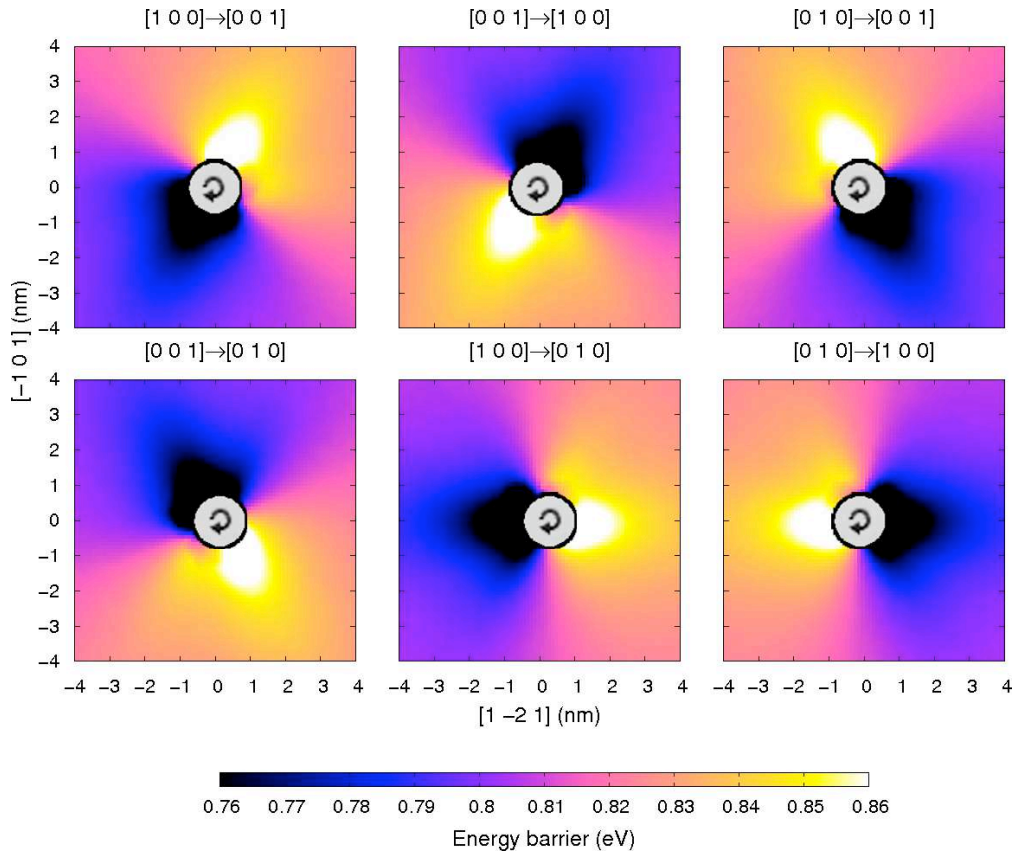

Figure B.5: Cartographie des barrières d'énergie obtenues par des simulations atomistiques pour la diffusion de l'atome de carbone autour d'une dislocation vis (au centre) qui est alignée parallèlement à la direction [111] (perpendiculaire à la page). Le cercle gris au centre (diamètre équivaut à 8b) se rapporte à la région définie comme étant le coeur de la dislocation.

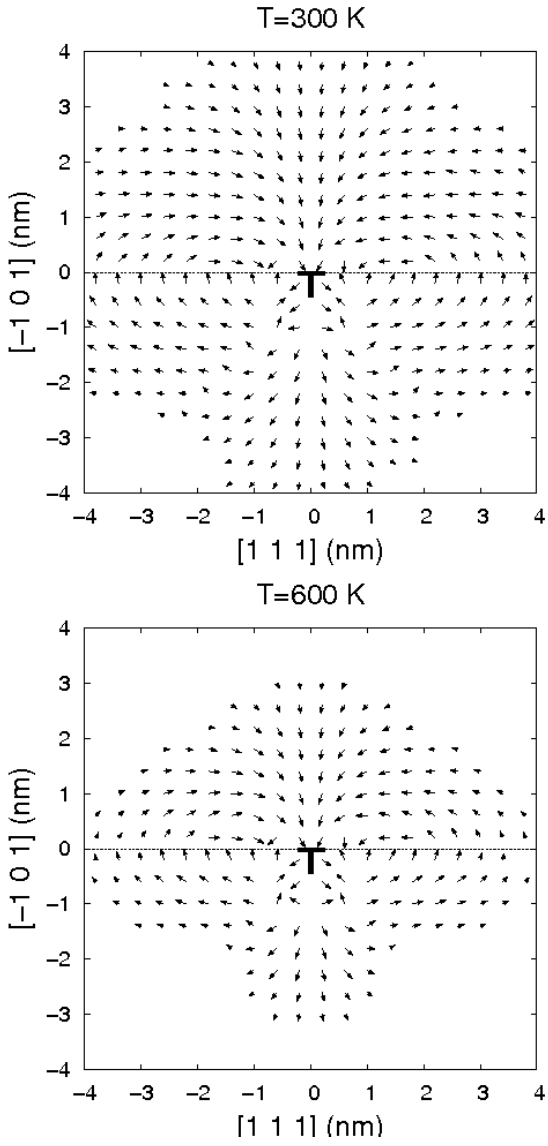

Figure B.6: Vecteur de déplacement moyen dans le voisinage d'une dislocation coin pour $T = 300$ K et $T = 600$ K.

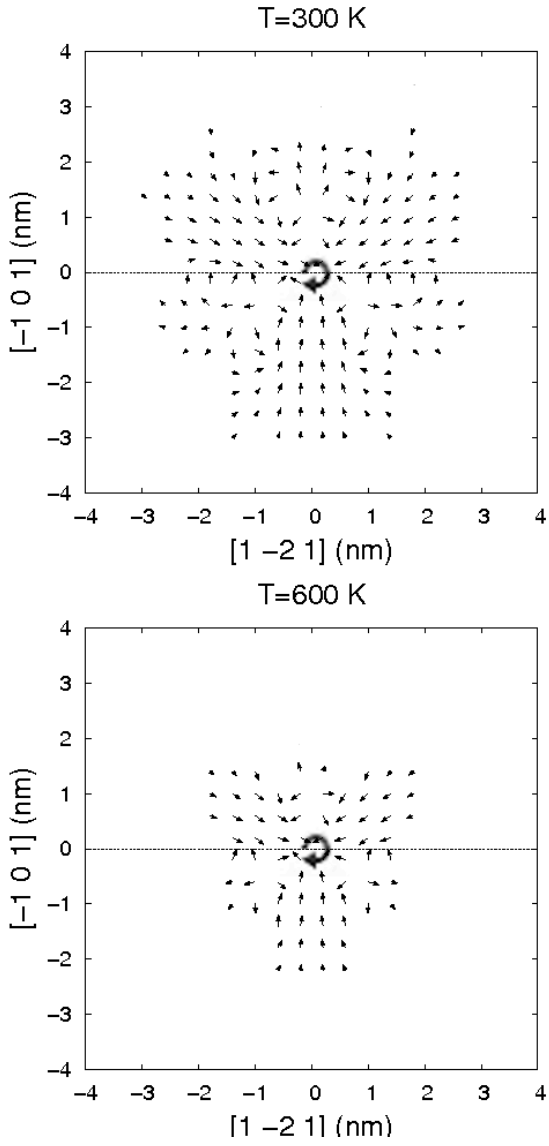

Figure B.7: Vecteur de déplacement moyen dans le voisinage d'une dislocation vis pour $T = 300$ K et $T = 600$ K.

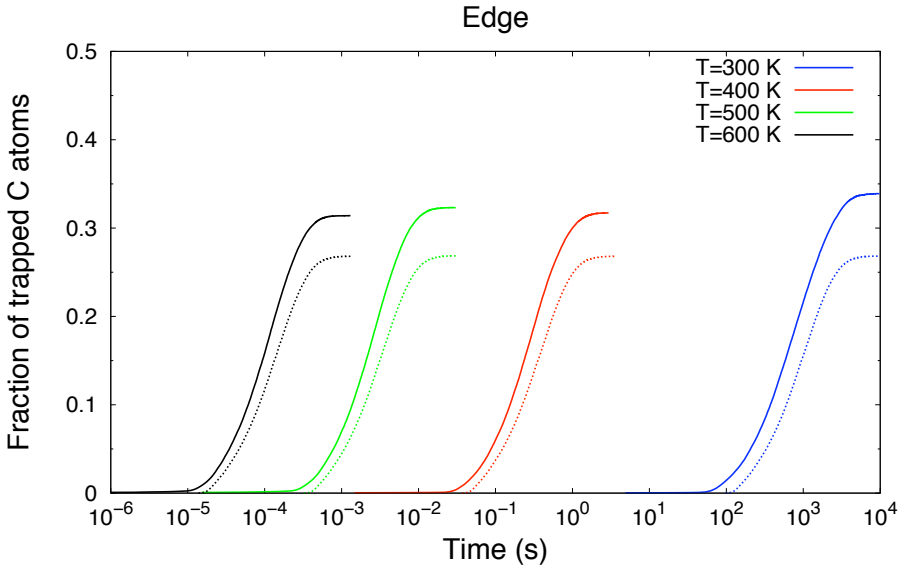

Figure B.8: Fraction des trajectoires d'atomes de carbone qui aboutissent dans le coeur d'une dislocation coin lors de simulations MCC pour des températures allant de 300 K à 600 K. Les lignes en pointillé représentent les résultats des marches aléatoires simples.

cette étude. A cette température, l'atome de carbone diffuse la plupart du temps (environ 80% du nombre total de sauts, à $T = 300$ K) au-dessus du plan de glissement, où la contrainte de traction normale due à la dislocation coin abaisse les énergies d'activation, ce qui accélère la diffusion. Pour la dislocation vis, l'effet est inverse: il y a un retard dans le début de la cinétique de diffusion par rapport à la marche aléatoire simple, clairement observé à $T = 300$ K. Un tel retard disparaît presque à $T = 600$ K. Par conséquent, la diffusion d'un atome de carbone dans le voisinage d'une dislocation vis, au moins à basse température, est ralentie en raison de l'interaction de l'impureté avec le champ de contraintes de la dislocation. Comparé à des simulations de marche aléatoire simple, pour lesquelles 27% des trajectoires des atomes de carbone aboutissent à un cylindre de rayon $4b$ par hasard, la fraction des trajectoires de carbone se terminant soit dans le coeur d'une dislocation coin ou vis plutôt que de quitter la boîte de simulation varie entre 32-34% et entre 30-32%, respectivement. En d'autres termes, les dislocations coin et vis ont la capacité d'attirer les atomes de carbone qui diffusent à proximité, même si un tel effet, pour les deux types de dislocation, semble être trop faible à première vue. Comme illustré dans la Fig. B.6, l'atome de carbone perçoit différemment l'influence d'une dislocation coin au-dessus et en dessous du plan de glissement, même relativement loin de la ligne de dislocation.

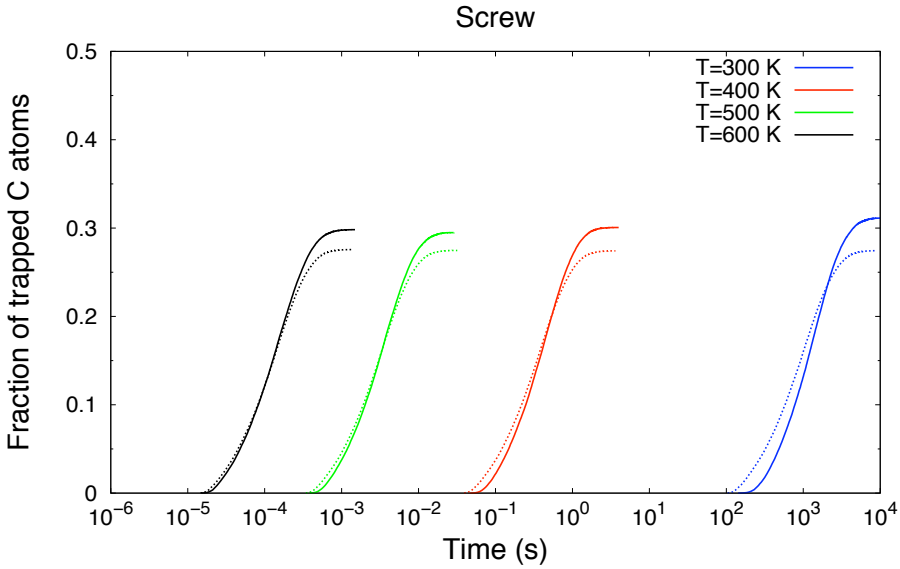

Figure B.9: Fraction des trajectoires d'atomes de carbone qui aboutissent dans le coeur d'une dislocation coin lors de simulations MCC pour des températures allant de 300 K à 600 K. Les lignes en pointillé représentent les résultats des marches aléatoires simples.

B.3 Comparaison entre les simulations atomistiques et la théorie de l'élasticité anisotrope

Il a été récemment montré que les résultats des calculs d'élasticité présentent un bon accord quantitatif entre les énergies de liaison carbone-dislocation obtenus par simulations atomistiques et la théorie de l'élasticité anisotrope [Clouet 2008], à condition que la séparation entre les deux défauts soit supérieure à 2 nm (dislocation coin) et 0,2 nm (dislocation vis). Plus récemment, Hanlumyuang et autres ont modélisé la distribution du carbone et sa concentration autour des dislocations dans le fer cubique centré à T=300 K et T=400 K avec une combinaison de calculs DFT et d'élasticité anisotrope, concluant que les effets de la chimie et du magnétisme au-delà de ceux déjà reflétés dans les constantes élastiques peuvent être négligés en toute sécurité [Hanlumyuang 2010].

Dans notre travail, les barrières d'énergie pour la migration du carbone dans le coeur de la dislocation obtenues par nos simulations atomistiques ont été comparées aux prédictions de la théorie de l'élasticité anisotrope. L'accord est meilleur pour les sites octaédrique (qui sont des minima d'énergie) par rapport aux sites tétraédriques (qui sont des points-selle). Les différences absolues dans les barrières d'énergie obtenues par les deux méthodes sont généralement inférieures à 5 meV lorsque l'atome de carbone est situé à des distances supérieures à 1,5

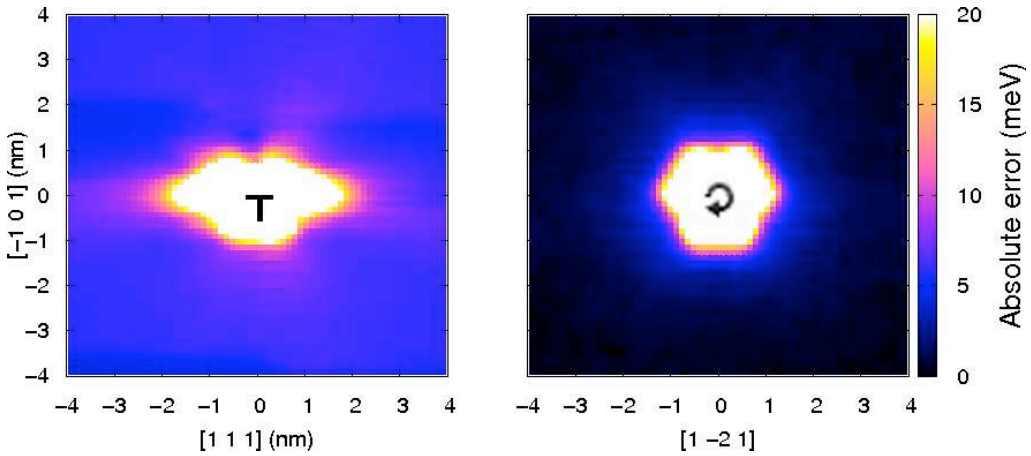

Figure B.10: Cartographie des différences absolues (erreurs) entre les barrières d'énergie obtenues par des simulations atomistiques et les calculs d'élasticité anisotrope en fonction de la position de l'atome de carbone autour d'une dislocation coin ou vis (au centre).

nm de la ligne de la dislocation vis et 2 nm (jusqu'à 4 nm, dans le plan de glissement) de la ligne de la dislocation coin (Figs. 7). Des simulations MCC réalisées à T=300 K et une analyse supplémentaire des énergies d'activation obtenues par chacune des méthodes montrent qu'elles sont globalement en bon accord qualitatif, en dépit de certaines differences importantes à proximité du coeur des dislocations.

Les résultats présentés ici nous permettent d'envisager un protocole afin d'utiliser le MCC pour effectuer des simulations réalistes à l'échelle atomique de la ségrégation du carbone aux dislocations et la formation des nuages de Cottrell tout en gardant des temps de calcul raisonnables. Ceci peut être réalisé par le cloisonnement des simulations AKMC en deux parties comme suit:

1. Afin d'accélérer les simulations MCC, on utilisera un catalogue statique de barrière dans les situations où les transitions que le système peut subir sont prévisibles. Ce catalogue sera construit de la manière suivante:

   a) les énergies de migration de l'atome de carbone situé loin de la dislocation, donc lorsque le champ de déformation nest pas trop important peuvent être obtenues à partir de calculs d'élasticité. Ces calculs sont très rapides: environ un million d'énergies de liaison carbon-dislocation peuvent être obtenus en moins d'une minute sur un ordinateur mono-processeur.

   b) à un certain moment, selon la séparation carbone-dislocation (et en fonction d'un seuil défini par l'utilisateur), les simulations atomistiques devront être employées plutôt que la théorie de l'élasticité anisotrope pour aug-

menter la précision du calcul. Le calcul de quelques milliers de barrière dure habituellement un ou deux mois sur un cluster de taille moyenne avec les processeurs actuels.

2. On complémentera ce catalogue d'une approche à la volée pour obtenir les énergies de point-selle lorsque deux ou plusieurs atomes de carbone seront censés interagir (près de la dislocation, au sein du nuage, par exemple). Dans ce cas, une méthode telle que la technique d'activation-relaxation (ART) [Barkema 1996] peut être utilisée pour construire la connectivité entre les états voisins et ensuite la technique de Nudge Elastic Band (NEB) peut être utilisée pour obtenir les énergies de point-selle. Un exemple de simulation MCC sur-le-volée (concernant la diffusion de vacance dans le silicium) est présenté par F. El-Mellouhi et co-travailleurs [El-Mellouhi 2008].

B.4 Diffusion du carbone à l'intérieur du coeur des dislocations

La région désordonnée du coeur des dislocations a longtemps été supposée être un canal par lequel la diffusion a lieu de manière quasi-unidimensionnelle et très rapidement. Ce type de diffusion dans le coeur joue un rôle aussi important que la diffusion en volume pour le problème du vieillissement des matériaux. Par exemple, le voisinage d'une dislocation est un environnement idéal pour la nucléation des précipités en raison de la diffusion en volume. Aux dernières étapes du processus de vieillissement, le coeur lui-même pourrait agir comme une voie rapide à travers laquelle les impuretés voyagent et se retrouvent à faire grossir des particules de précipités le long de la ligne de dislocation. Récemment, les résultats expérimentaux de Legros et co-auteurs [Legros 2008] a fourni une preuve directe d'une diffusivité elevée dans le coeur d'un matériau cristallin (dans leur cas, l'aluminium).

Nous avons réalisé des simulations atomistiques pour obtenir les barrières d'énergie dans le coeur d'une dislocation coin et d'une dislocation vis. Pour ce faire, au lieu de supposer que le point-selle correspondait au site tétraédrique, nous avons effectué des calculs de NEB. Nous avons constaté que le maximum d'énergie de liaison entre un atome de carbone et une dislocation est de 0,65 eV (pour la dislocation coin) et 0,41 eV (pour la dislocation vis). Nos calculs indiquent que les valeurs des barrières d'énergie, dans le coeur, présentent une grande variation (voir Fig. B.11). La barrière peut être aussi faible que 0,14 eV

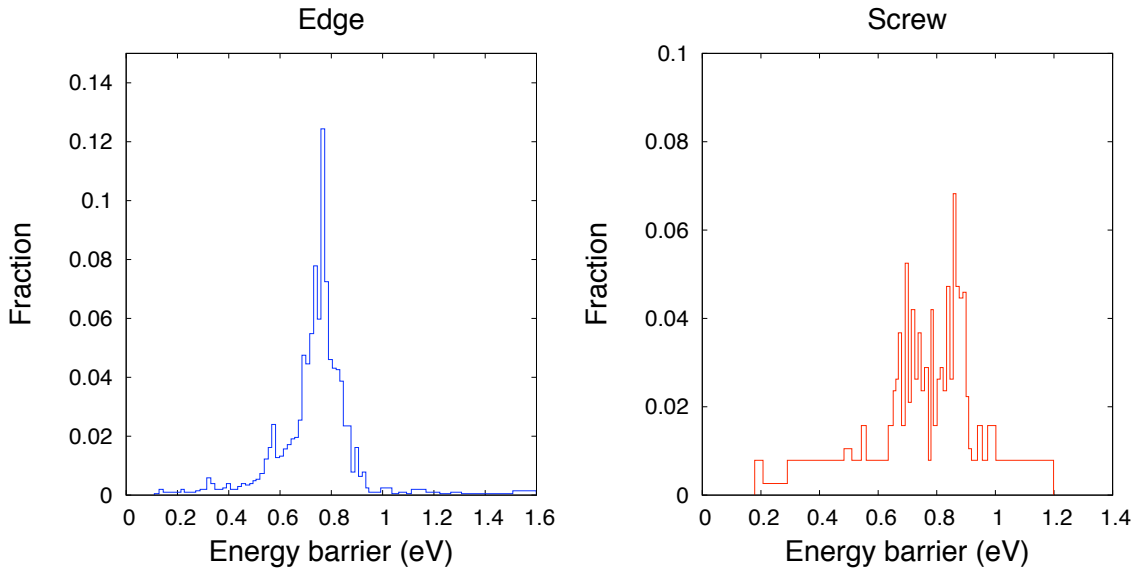

Figure B.11: Distribution des barrières d'énergie dans la région définie comme le coeur ($R < 4b \approx 1$ nm) d'une dislocation coin et d'une dislocation vis.

dans le coeur d'une dislocation coin et 0,19 eV dans le coeur d'une dislocation vis.

Les simulations MCC effectuées en utilisant ces barrières montrent que la diffusion dans le coeur des dislocations est un processus complexe, où la plupart du temps l'atome de carbone se promène dans un sous-ensemble d'états séparés par des barrières de basse énergie, et saute éventuellement des barrières d'énergie plus élevées afin de diffuser le long de la ligne de dislocation. Ce comportement a été confirmé par des simulations de dynamique moléculaire. Ce problème de faibles barrières est bien connu dans la literature [Voter 2002, Puchala 2009] et nous a empêché de simuler la diffusion de l'atome de carbone pour des températures inférieures à 400 K et 750 K dans le coeur d'une dislocation coin et d'une dislocation vis, respectivement. Au-dessus de ces températures, le MCC nous a permis d'obtenir des trajectoires longues de l'atome de carbone dans le coeur des dislocations. À partir de ces trajectoires, nous avons obtenu le coefficient de diffusion D_{coeur} du carbone dans le coeur et, à partir de la pente de $\ln(D_{coeur})$, le facteur pré-exponentiel D_0 et l'énergie d'activation efficace E^m_{eff} pour la diffusion dans le coeur (voir Tab. B.1). Nos résultats indiquent que la diffusion dans le coeur des dislocations est d'environ deux ordres de grandeur plus grand que la diffusion dans la matrice.

	D_0 (m^2/s)	E^m_{eff} (eV)
Matrice	1.3×10^{-7}	0.816
Coin	9.9×10^{-6}	0.670
Vis	1.0×10^{-5}	0.738

Table B.1: Le facteur pré-exponentiel et l'énergie d'activation efficace pour la diffusion dans la matrice et dans la région définie comme le coeur ($R < 4b \approx 1$ nm) d'une dislocation coin où vis.

B.5 La répartition des atomes de carbone dans le champ de contraintes des dislocations

Ce travail de thèse nous a permis également de revisiter certains travaux théoriques classiques sur la distribution des atomes de carbone dans le champ de contraintes des dislocations dans le fer cubique centré. Nous avons ainsi utilisé les énergies de liaison carbone-dislocation obtenues par des simulations atomistiques pour déterminer par la méthode statistique proposée par Louat [Louat 1956] la concentration d'atomes de carbone autour des dislocations coin et vis en utilisant l'Eq. (B.2). Dans cette equation, $\overline{n}_i$ est l'occupation d'un site d'énergie de liaison carbone-dislocation E^b_i et $\overline{n}_0$ est l'occupation moyenne de la matrice de fer α, où l'atome de carbone n'interagit pas avec avec la dislocation. Il convient de mentionner quùne méthode du type Monte Carlo a été utilisée pour déterminer la concentration de saturation dans le coeur des dislocations, qui a été prise comme la valeur maximale de $\overline{n}_i$ (0.17 autour d'une dislocation coin et 0.16 autour d'une dislocation vis).

$$\overline{n}_i = \frac{\dfrac{\overline{n}_0}{1-\overline{n}_0}\exp\left(\dfrac{E^b_i}{kT}\right)}{1+\dfrac{\overline{n}_0}{1-\overline{n}_0}\exp\left(\dfrac{E^b_i}{kT}\right)} \tag{B.2}$$

La proximité d'une dislocation peut être divisée en zones "attractives", où $E^b > kT$ (respectivement "répulsives", où $E^b < -kT$), où la probabilité de trouver un atome de carbone est supérieure (respectivement inférieure) à la concentration moyenne de la matrice (voir Fig. B.12). Ces zones se fondent dans les régions où prédomine la contrainte de cisaillement (c'est-à-dire tout autour de la dislocation vis, et à proximité du plan de glissement de la dislocation coin), puisque deux sites voisins peuvent présenter une alternance d'énergies de liaison positives et négatives vers la ligne de dislocation.

En utilisant l'Eq. (B.2) et en tenant compte de la concentration de saturation,

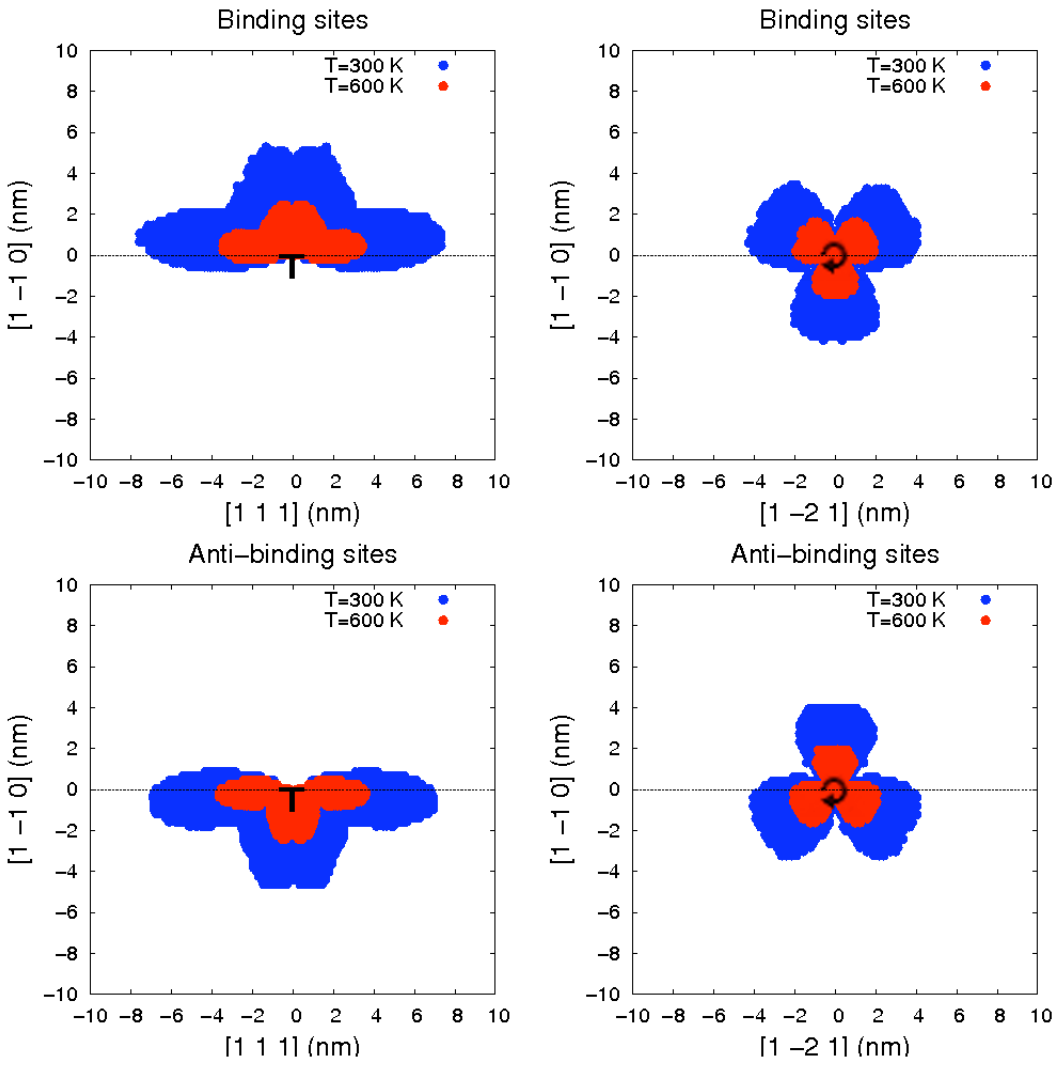

Figure B.12: L'extension et la forme des zones attractives et répulsives autour d'une dislocation coin (à gauche) et d'une dislocation vis (à droite) définis selon le critère de la Réf. [Cochardt 1955] avec $T = 300K$ et $T = 600$ K. La ligne pointillée représente le plan de glissement des dislocations.

Méthode	Références	Dislocation	Extension (nm)	$N_{C/l}$ (nm^{-1})
Sonde atomique	[Wilde 2000]	Vis	10×10	105
Statique moléculaire	Ce travail	Coin	15×6	240
	Ce travail	Vis	8×8	125

Table B.2: Extension et nombre d'atomes de carbone par unité de longueur de dislocation, en nm^{-1}, dans la zone correspondant à une atmosphère de Cottrell (Fe-0.85at% C).

il a été possible de générer des distributions des atomes de carbone dans une atmosphère de Cottrell autour d'une dislocation coin et d'une dislocation vis, comme indiqué dans la Fig. B.13. Nous avons comparé ces résultats théoriques aux résultats des expériences de sonde atomique, par example, le travail de Wilde et co-auteurs [Wilde 2000]. Pendant le vieillissement statique du spécimen ces auteurs constatent qu'environ 105 atomes de carbone par nanomètre ont diffusé vers la dislocation pour former une atmosphère de Cottrell. Cette valeur est proche de ce que nous avons prévu théoriquement autour d'une dislocation vis (125 C/nm), et moins de la moitié du nombre d'atomes de carbone qui sont attendus dans le champ de contraintes d'une dislocation coin (240 C/nm) (voir Tab. B.2).

Une des perspectives de ce travail est la détermination de la force d'ancrage de ces atmosphères. Pour cela, on pourrait générer par notre méthode des concentrations de carbone différentes, chacune représentant une étape de formation de l'atmosphère de Cottrell au cours du vieillissement statique (de la première arrivée des interstitiels jusqu'à l'achèvement de l'atmosphère), et déterminer ensuite la force nécessaire pour décrocher la dislocation par dynamique moléculaire en appliquant une contrainte extérieure de cisaillement.

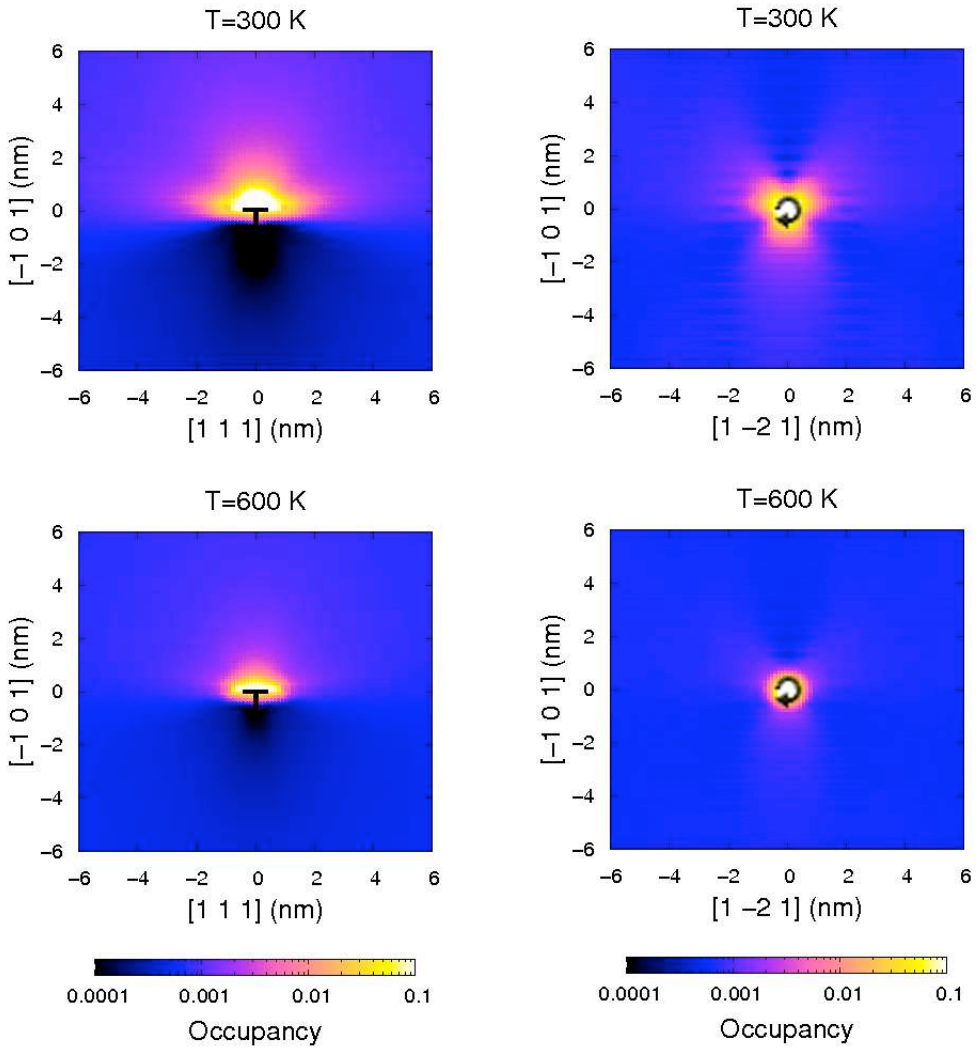

Figure B.13: Cartographie de l'occupation fractionnelle des sites interstitiels autour d'une dislocation coin (à gauche) et d'une dislocation vis (à droite) avec $T = 300$ K et $T = 600$ K pour Fe-0.18at%C, comme dans les Réfs. [Miller 2003, Miller 2006].

Bibliography

[Ackland 1997] G. J. Ackland, D. J. Bacon, A. F. Calder and T. Harry. Philos. Mag. A, vol. 75, page 713, 1997.

[Ackland 2004] G. J. Ackland, M. I. Mendelev, D. J. Srolovitz, S. Han and A. V. Barashev. J. Phys.: Cond. Mat., vol. 16, page S2629, 2004.

[Bacon 1980] D. J. Bacon, D. M. Barnett and R. O. Scattergood. Prog. Mater. Sci., vol. 23, pages 51–262, 1980.

[Barkema 1996] G. T. Barkema and N. Mousseau. Phys. Rev. Lett., vol. 77, page 4358, 1996.

[Barlett 2009] V. Ruiz Barlett, J. J. Bigeón, M. Hoyuelos and H. O. Mártin. J. Comp. Phys., vol. 228, page 5740, 2009.

[Bass 1962] J. Bass and D. Lazarus. J. Phys. Chem. Solids, vol. 23, page 1820, 1962.

[Becquart 2007] C. S. Becquart, J. M. Raulot, G. Benecteux, C. Domain, M. Perez, S. Garruchet and H. Nguyen. Comp. Mater. Sci., vol. 40, pages 119–129, 2007.

[Becquart 2009] C. S. Becquart and C. Domain. Phys. Status Solidi B, vol. 247, page 9, 2009.

[Becquart 2010] C. S. Becquart and C. Domain. Met. Mat. Trans. A, vol. 42A, page 852, 2010.

[Beshers 1958] D. N. Beshers. Acta Metall, vol. 6, page 521, 1958.

[Blavette 1999] D. Blavette, E. Cadel, A. Fraczkiewicz and A. Menand. Science, no. 5448, page 2317, 1999.

[Bortz 1975] A. B. Bortz, M. H. Kalos and J. L. Lebowitz. J. Comp. Phys, vol. 17, page 10, 1975.

[Bosman 1960] A. J. Bosman, P. E. Brommer, L. C. H. Eijkelenboom, C. J. Schinkel and G. W. Rathenau. Physica, vol. 26, page 533, 1960.

[Bullough 1959] R. Bullough and R. C. Newman. Proc. R. Soc., vol. A249, page 427, 1959.

[Buono 1998] V. T. L. Buono, M. S. Andrade and B. M. Gonzalez. Metall. Trans. A, vol. 29A, page 1415, 1998.

[Cadel 1999] E. Cadel, D. Lemarchand, A.-S. Gay, A. Fraczkiewicz and D. Blavette. Scripta Mater., vol. 41, page 421, 1999.

[Cancès 2009] E. Cancès, M.-C. Marinica, F. Legoll, K. Minoukadeh and F. Willaime. J. Chem. Phys., vol. 130, page 114711, 2009.

[Castin 2011] N. Castin. PhD thesis, Université Libre de Bruxelles, 2011.

[Chang 1985] L. Chang. PhD thesis, Oxford University, 1985.

[Chen 2008] Q. Chen, X.-Y. Liu and S. Biner. Acta Materialia, vol. 56, pages 2937–2947, 2008.

[Clouet 2006] E. Clouet. Acta Materialia, vol. 54, page 3543, 2006.

[Clouet 2008] E. Clouet, S. Garruchet, H. Nguyen, M. Perez and C. S. Becquart. Acta Materialia, vol. 56, pages 3450–3460, 2008.

[Clouet 2009] E. Clouet, L. Ventelon and F. Willaime. Phys. Rev. Lett., vol. 102, page 055502, 2009.

[Cochardt 1955] A. W. Cochardt, G. Shoek and H. Wiedersich. Acta Metall., vol. 3, page 533, 1955.

[Codling 2008] E. A. Codling, M. J. Plank and S. Benhamou. J. R. Soc. Interface, vol. 5, page 813, 2008.

[Cottrell 1949] A. H. Cottrell and B. A. Bilby. Proc. Phys. Soc. A, vol. 62, page 49, 1949.

[Daw 1983] M. S. Daw and M. I. Baskes. Phys. Rev. Lett., vol. 50, page 1285, 1983.

[De 2000] A. K. De, K. De Blauwe, S. Vandeputte and B. C. De Cooman. J. All. Com., vol. 310, page 405, 2000.

[De 2001] A. K. De, S. Vandeputte and B. C. De Cooman. JMEPEG, vol. 10, page 567, 2001.

[Domain 2004] C. Domain, C. S. Becquart and J. Foct. Phys. Rev. B, vol. 69, page 144112, 2004.

[Douthwaite 1973] R. M. Douthwaite and J. T. Evans. Scripta Metallurgica, vol. 7, page 1019, 1973.

[El-Mellouhi 2008] F. El-Mellouhi, N. Mousseau and L. J. Lewis. Phys. Rev. B, vol. 78, page 153202, 2008.

[Elsen 1993] P. Elsen and H. P. Hougardy. Steel Res., vol. 64, page 431, 1993.

[Eshelby 1953] J. D. Eshelby, W. T. Read and W. Shockley. Acta Metall., vol. 1, page 251, 1953.

[Eshelby 1955] J. D. Eshelby. Acta Metall., vol. 3, page 487, 1955.

[Eyring 1935] H. Eyring. J. Chem. Phys., vol. 3, page 107, 1935.

[Fichthorn 1991] K. A. Fichthorn and W. H. Weinberg. J. Chem. Phys., vol. 95, page 1090, 1991.

[Frenkel 2002] Daan Frenkel and Berend Smit. Understanding molecular simulation – from algorithms to applications. Academic Press, 2002.

[Garruchet 2008] S. Garruchet and M. Perez. Comp. Mat. Sci., vol. 43, no. 2, pages 286–292, 2008.

[Graff 2004] S. Graff, S. Forest, J.-L. Strudel, C. Prioul, P. Pilvin and J.-L. Bchade. Mat. Sci. and Eng. A, vol. 387, page 181, 2004.

[Ham 1959] F. S. Ham. J. App. Phys., vol. 30, page 915, 1959.

[Hanlumyuang 2010] Y. Hanlumyuang, P. A. Gordon, T. Neeraj and D. C. Chrzan. Acta Materialia, vol. 58, pages 5481–5490, 2010.

[Harper 1951] S. Harper. Phys. Rev., vol. 83, page 709, 1951.

[Hartley 1966] S. Hartley. Acta Metall., vol. 14, page 1237, 1966.

[Henderson 1972] B. Henderson. Defects in crystalline solids, page 170. Edward Arnold, 1972.

[Henkelman 2000a] G. Henkelman, G. Jóhannesson and H. Jónsson. Progress on theoretical chemistry and physics, chapitre 10. Kluwer Academic Publishers, 2000.

[Henkelman 2000b] G. Henkelman, B. P. Uberuaga and Hannes Jonsson. J. Chem. Phys., vol. 113, page 9901, 2000.

[Hin 2008] C. Hin, Y. Bréchet, P. Maugis and F. Soisson. Acta Materialia, vol. 56, pages 5535–5543, 2008.

[Hoover 1985] W. G. Hoover. Phys. Rev. A, vol. 31, page 1695, 1985.

[Huang 1989] J. Huang, M. Meyer and V. Pontikis. Phys. Rev. Lett., vol. 63, page 628, 1989.

[Jiang 2003] D. E. Jiang and E. A. Carter. Phys. Rev. B, vol. 67, page 214103, 2003.

[Johnson 1964] R. A. Johnson, G. J. Dienes and A. C. Damask. Acta Metall., vol. 12, page 1215, 1964.

[K. Kamber 1961] W. Wert K. Kamber D. Keefer. Acta Metall, vol. 9, page 403, 1961.

[Kalk 1995] A. Kalk, A. Nortmann and Ch. Schwink. Philos. Mag. A, vol. 72, page 1239, 1995.

[Kelly 2007] T. F. Kelly and M. K. Miller. Rev. Sci. Instr., vol. 78, page 031101, 2007.

[Kohm 1965] W. Kohm and L. J. Sham. Phys. Rev., vol. 140, page A1133, 1965.

[Krempaszky 2006] C. Krempaszky, U. Liedl and E. A. Werner. Comp. Mater. Sci., vol. 38, pages 90–97, 2006.

[Kresse 1993] G. Kresse and J. Hafner. Phys. Rev. B, vol. 47, page 558, 1993.

[Lavaire 2001] N. Lavaire, J. Merlin and V. Sardoy. Scripta Mater., vol. 44, page 554, 2001.

[Lavaire 2004] N. Lavaire, V. Massardier and J. Merlin. Scripta Mater., vol. 50, page 131, 2004.

[Legros 2008] M. Legros, G. Dehm, E. Arzt and T. J. Balk. Science, vol. 319, page 1646, 2008.

[Leslie 1961] W. C. Leslie. Acta Metall, vol. 9, page 1004, 1961.

[Ling 1993] C. P. Ling and P. G. McCormick. Acta Metall. Mater., vol. 41, page 3127, 1993.

[Louat 1956] N. Louat. Proc. Phys. Soc. B, vol. 69, no. 459, 1956.

[Love 1964] G. R. Love. Acta Metall., vol. 12, page 731, 1964.

[Macnab 1972] R. M. Macnab and D. E. Koshland. Proc. Natl. Acad. Sci. U.S.A., vol. 69, page 2509, 1972.

[Marcelin 1915] R. Marcelin. Ann. Physique, vol. 3, page 120, 1915.

[Marquis 2010] E. A. Marquis and J. M. Hyde. Mat. Sci. Eng. R, vol. 69, 2010.

[Mendelev 2003] M. I. Mendelev, S. Han, D. J. Srolovitz, G. J. Ackland, D. Y. Sun and M. Asta. Philos. Mag., vol. 83, page 3977, 2003.

[Mesarovic 1995] S. D. Mesarovic. J. Mech. Phys. Solids., vol. 43, page 671, 1995.

[Metropolis 1953] N. Metropolis, A. W. Rosenbluth, M. N. Rosenbluth, A. H. Teller and E. Teller. J. Chem. Phys., vol. 21, 1953.

[Miller 2003] M. K. Miller, E. A. Kenik, K. F. Russell, L. Heatherly, D. T. Hoelzer and P. J. Maziasz. Mat. Sci. and Eng. A, vol. 353, page 140, 2003.

[Miller 2006] M. K. Miller. Microsc. Res. Tech., vol. 69, page 359, 2006.

[Muba 1962] T. Muba and J. O. Brittain. Acta Metall, vol. 10, page 974, 1962.

[Nosé 1984] S. Nosé. J. Chem. Phys., vol. 81, page 511, 1984.

[Osetsky 2003] Y. N. Osetsky and D. J. Bacon. Modelling Simul. Mater. Sci. Eng., vol. 11, page 427, 2003.

[Picu 2004] R. C. Picu and D. Zhang. Acta Materialia, vol. 52, page 161, 2004.

[Plimpton 1995] S. J. Plimpton. J. Comp. Phys., vol. 117, pages 1–19, 1995.

[Porter 1981] D. A. Porter and K. E. Easterling. Phase transformations in metals and alloys. London: Chapman and Hall, 2nd édition, 1981.

[Press 2007] W. H. Press, S. A. Teukolsky, W. T. Vetterling and B. P. Flannery. Numerical recipes: The art of scientific programming. http://www.nrbook.com, 2007.

[Puchala 2009] B. T. Puchala. PhD thesis, The University of Michigan, 2009.

[Purja 2009] G. P. Purja and Y. Mishin. Acta Materialia, vol. 57, page 5531, 2009.

[Ramasubramaniam 2008] A. Ramasubramaniam, M. Itakura, M. Ortiz and E. A. Carter. J. Mater. Res., vol. 23, page 2757, 2008.

[Rudnick 2004] J. Rudnick and G. Gaspari. Elements of the random walk, chapitre 5. Cambridge University Press, 2004.

[Saad 2003] Y. Saad. Iterative methods for sparse linear systems. Society for Industrial and Applied Mathematics, 2003.

[Sandvik 1983] B. P. J. Sandvik and C. M. Wayman. Metall. Trans. A, vol. 14A, page 809, 1983.

[Sherman 2007] D. Sherman, S. Cross, S. Kim, F. Grandjean, G. J. Long and M. K. Miller. Met. Mat. Trans. A, vol. 38AA, page 1698, 2007.

[Shewchuk 1994] J. R. Shewchuk. *An Introduction to the Conjugate Gradient Method Without the Agonizing Pain*, 1994.

[Sinclair 2010] C. W. Sinclair, M. Perez, R. G. A. Veiga and A. Weck. Phys. Rev. B, vol. 81, page 224204, 2010.

[Stott 1980] M. J. Stott and E. Zaremba. Phys. Rev. B, vol. 22, page 1564, 1980.

[Stroh 1958] A. N. Stroh. Philos. Mag., vol. 3, page 625, 1958.

[Stroh 1962] A. N. Stroh. J. Math. Phys., vol. 41, page 77, 1962.

[Swope 1982] W. C. Swope, H. C. Andersen, P. H. Berens and K. R. Wilson. J. Chem. Phys., vol. 76, page 637, 1982.

[Tapasa 2007] K. Tapasa, Y. N. Osetsky and D. J. Bacon. Acta Materialia, vol. 55, page 93, 2007.

[Thompson 2007] K. Thompson, P. L. Flaitz, P. Ronsheim, D. J. Larson and T. F. Kelly. Science, no. 317, page 1370, 2007.

[Veiga 2010] R. G. A. Veiga, M. Perez, C. S. Becquart, C. Domain and S. Garruchet. Phys. Rev. B, vol. 82, page 054103, 2010.

[Verlet 1967] L. Verlet. Phys. Rev., vol. 159, page 98, 1967.

[Vineyard 1957] G. H. Vineyard. J. Phys. Chem. Solids, vol. 3, page 121, 1957.

[Voter 2002] A. F. Voter, F. Montalenti and T. C. Germann. Annual Review of Materials Research, vol. 32, no. 1, pages 321–346, 2002.

[Wigner 1932] E. Wigner. Z. Phys. Chem., vol. 19, page 203, 1932.

[Wilde 2000] J. Wilde, A. Cerezo and G. D. W. Smith. Scripta Mater., vol. 43, pages 39–48, 2000.

[Wuttig 1971] M. Wuttig and J. Keiser. Phys. Rev. B, vol. 3, page 815, 1971.

[Young 1966] W. M. Young and E. W. Elcock. Proc. Phys. Soc., vol. 89, no. 735, 1966.

[Zhang 2010a] F. Zhang, A. M. Walker, K. Wright and J. D. Gale. J. Mater. Chem., vol. 20, page 10445, 2010.

[Zhang 2010b] X. Zhang and G. Lu. Phys. Rev. B, vol. 82, page 012101, 2010.

FOLIO ADMINISTRATIF

THESE SOUTENUE DEVANT L'INSTITUT NATIONAL DES SCIENCES APPLIQUEES DE LYON

NOM : GOMES DE AGUIAR VEIGA DATE de SOUTENANCE : 16 Septembre 2011

Prénoms : Roberto

TITRE : Computational insights into the strain aging phenomenon in bcc iron at the atomic scale

NATURE : Doctorat Numéro d'ordre : 2011 ISAL 0084

Ecole doctorale : Matériaux de Lyon

Spécialité : Sciences des Matériaux

RESUME :

Le vieillissement statique est un concept important dans la métallurgie qui se réfère à un durcissement de la matière ayant subi une déformation plastique et est ensuite vieilli pendant une certaine période de temps. La théorie proposée dans les années 1940 par Cottrell et Bilby explique ce phénomène comme étant causé par l'épinglage des dislocations par les impuretés (par exemple, les atomes de carbone en solution solide) qui migrent au voisinage du défaut de ligne. Au cours de ce travail de thèse, le mécanisme atomistique responsabledu phénomène du vieillissement statique dans le fer alpha a été étudié par des simulations numériques. Etant donné que la diffusion à l'état solide se déroule lentement, l'utilisation de la dynamique moléculaire à basse température (lorsque l'effet du champ de contraintes sur la dislocation de diffusion du carbone est plus prononcé) a été évitée , et nous avons utilisé préférentiellement le couplage de la statique moléculaire avec le Monte-Carlo cinétique atomistique.

Trois points principaux ont été abordés dans cette thèse: (i) l'effet du champ de contraintes d'une dislocation coin ou vis sur un atome de carbone qui diffuse à proximité, (ii) la diffusion de l'atome de carbone dans le cour de la dislocation («pipe diffusion»), et (iii) la distribution d'équilibre des atomes de carbone dans une atmosphère de Cottrell. Le principal effet du champ de contrainte de la dislocation à l'extérieur du coeur est de biaiser la diffusion de l'impurité, de sorte que certains sauts (transitions) deviennent plus probables que d'autres. Cet effet va conduire aux premiers stades de la formation de l'atmosphère de Cottrell, lorsque l'interaction mutuelle entre atomes de carbone est négligeable. Au coeur de la dislocation, comme prévu, nos résultats indiquent que le carbone diffuse plus vite que dans le volume. La concentration de carbone dans le voisinage d'une dislocation coin ou vis a été modélisée par une approche de physique statistique en utilisant les énergies de liaison calculées par la statique moléculaire. Cette approche est en bon accord avec les données expérimentales.

MOTS-CLES : Strain aging, dislocation, carbon, diffusion, segregation, pipe diffusion, bcc iron, Cottrell atmosphere, molecular statics, molecular dynamics, atomistic kinetic Monte Carlo, anisotropic elasticity theory

Laboratoire (s) de recherche : Matériaux: Ingénierie et Sciences (MATEIS) UMR 5510

Directeur de thèse: Michel PEREZ, Charlotte BECQUART

Président de jury : David BACON

Composition du jury : D. Bacon, C. Sinclair (rapporteur), P. Maugis (rapporteur), M. Perez, C. Becquart. G. Monnet